ELASTOCAPILLARY INTERACTIONS BETWEEN LIQUIDS AND THIN SOLID FILMS UNDER TENSION

ELASTOCAPILLARY INTERACTIONS BETWEEN LIQUIDS AND THIN SOLID FILMS UNDER TENSION

By

RAFAEL D. SCHULMAN,
B.Sc. , M. Sc.

A Thesis
Submitted to the School of Graduate Studies
in Partial Fulfillment of the Requirements
for the Degree
Doctor of Philosophy

McMaster University

DOCTOR OF PHILOSOPHY (2018)
(Physics)

McMaster University
Hamilton, Ontario

TITLE: Elastocapillary interactions between liquids and thin solid films under tension

AUTHOR: Rafael D. Schulman,
B.Sc. (University of Western Ontario),
M.Sc. (McMaster University)

SUPERVISOR: Dr. Kari Dalnoki-Veress

NUMBER OF PAGES: x, 124

Abstract

In this thesis, experiments are described which study the elastocapillary interactions between liquids and taut solid films. The research employs contact angle measurements to elucidate how capillary forces deform compliant solid structures, but also to attain fundamental insight into the energy of interfaces involving amorphous solids.

The majority of the work focuses on how capillary deformations of compliant elastic membranes introduce modifications to descriptions of common wetting phenomena. Particular focus is given to studying partial wetting in the presence of compliant membranes in various geometries: droplet on a free-standing membrane, droplet capped by a membrane but sessile on a rigid substrate, and droplet pressed between two free-standing membranes. The mechanical tension in these membranes is found to play an equivalent role as the interfacial tensions. As such, the mechanical tension is incorporated into Young-Dupré's law (capped droplet on a rigid substrate) or Neumann's triangle (droplet on free-standing membrane), leading to departures from the classical wetting descriptions. In addition, one study is conducted investigating how viscous dewetting is affected by the liquid film being capped by an elastic film. The results of this study show that the dewetting rate and rim morphology are dictated by the elastic tension.

Another important aspect of the work is demonstrating the utility of anisotropic membrane tension for liquid patterning. A biaxial tension is shown to produce droplets and dewetting holes which are elongated along the high tension direction. The compliant membrane geometry can also be designed to produce droplets and holes with square morphology.

In the final project, the surface energy of strained glassy and elastomeric solids is studied. Glassy solids are shown to have strain-dependent surface energies, which implies that surface energy (energy per unit area) and surface stress (force per unit length) are not equivalent for this class of materials by virtue of the Shuttleworth equation. On the other hand, this study provides strong evidence that surface energy and surface stress are equivalent for elastomeric interfaces.

Preface

This is a “sandwich” thesis based on the papers published or submitted during my PhD. The first chapter will serve as an introduction for the reader, providing the concepts necessary to digest the papers that follow. In Chapter 2, I outline supplementary details of the experimental methods and data analysis protocols beyond those that already appear in the manuscripts. This chapter will be of assistance to those who seek to replicate or perform extensions of research presented herein. Chapter 3 contains the core papers of this thesis that have been published or submitted. Each paper is prefaced by a summary of the work and a description of the contributions I have made to each study. The final chapter contains a summary of the research presented within this thesis, emphasizing the overarching story told by these papers, and outlines some future directions that ought to be explored. In the Appendix, I list other papers that I have been involved in and include a brief summary of the key findings of each.

Acknowledgements

The past four years have been a life-changing journey. Reflecting on the hard work behind this thesis, I realize that I've accomplished something that my younger self would never have thought possible. At the same time, there are people who have supported and guided me, and without whom I wouldn't have come this far.

First and foremost, I extend my sincerest gratitude to my supervisor, Kari. Any success I've had in the lab can be traced back to your mentorship and experimental saviness. You have an unmatched talent for designing experiments that embody creativity and ingenuity, but at the same time, remarkable simplicity. I've never met anyone with a better intuition for physics. From personal experience, I would advise others never to enter a physics-related argument with you- their chances of winning are exceedingly low. Your guidance has taught me the most important lessons during these years, both in physics and beyond. You've succeeded in being an incredible supervisor, but also a friend, and I'm sure that no future boss will ever compare.

A big thank you goes out to all the grad students in the KDV experience that have been good friends during my PhD: Solomon, Mark, Paul, Adam, John, JC, Carmen, Clementine, and Ben. You guys have made this journey such a pleasure. I would also like to thank the Paris team, especially Tom and Elie, for doing incredible theory work and teaching me to approach a problem from several angles.

I would never have reached this point without the infinite support of my family. My sisters, brother-in-laws, and most importantly, my parents, have been an incredible source of love and encouragement. Mom and dad, your unwavering confidence in me has provided me with the courage needed to face the challenges ahead. Your support means more to me than I can ever describe. Thank you for being such amazing role models and for teaching me the importance of ambition.

Finally, I want to thank the most important person in my life, my future wife, Michelle. You've been there for me every step of the way, motivating me, believing in me, and supporting me. After a hard day, you always know just the right things to say to make me feel better. You truly brighten up every single day, and I'm so unbelievably lucky to have such a wonderful and loving person at my side. We're an amazing team. There is no one I would rather walk the road ahead with than you, and I'm so excited for the adventures that await us.

Contents

Abstract iii
Preface iv
Acknowledgements v

1 Introduction **1**
- 1.1 Surface tension 2
    - 1.1.1 Energetic cost of forming interface 2
    - 1.1.2 A force parallel to the interface 4
    - 1.1.3 Laplace pressure 6
    - 1.1.4 The gravity capillary length 7
- 1.2 Wetting 8
    - 1.2.1 Partial wetting on a rigid solid 9
    - 1.2.2 Partial wetting on a liquid 11
    - 1.2.3 Dewetting 12
- 1.3 Elasticity of solid films 16
    - 1.3.1 Hooke's law 17
    - 1.3.2 Plane stress 18
    - 1.3.3 Transverse loading of a solid film 23
    - 1.3.4 Elastic materials 27
- 1.4 Surface energy and surface stress of solid interfaces 29
- 1.5 Elastocapillarity 33
    - 1.5.1 Partial wetting on a soft solid 35
    - 1.5.2 Partial wetting on a compliant solid film 38

1.5.3 Elastocapillary interactions in dewetting 41

2 Experimental details **43**

2.1 Creating thin polymer films 43

2.1.1 Materials 43

2.1.2 Film preparation 44

2.2 Creating tension in solid films 46

2.2.1 Method 1: isotropic tension set by film thickness 46

2.2.2 Method 2: biaxial tension from tunable uniaxial strain 48

2.2.3 Method 3: biaxial or isotropic tension from tunable biaxial strain 50

2.3 Droplet deposition 52

2.4 Contact angle measurements 53

3 Papers **57**

3.1 Paper I 59

3.2 Paper II 67

3.3 Paper III 80

3.4 Paper IV 88

3.5 Paper V 99

4 Conclusions and future outlook **107**

A Papers not included in this thesis **111**

Paper AI 112

Paper AII 112

Paper AIII 112

Bibliography **113**

List of Figures

1.1 Intermolecular interactions in a liquid 3
1.2 Pulling on a liquid membrane 4
1.3 Origin of Laplace pressure 6
1.4 Partial wetting on a rigid solid 9
1.5 Partial wetting on a liquid 11
1.6 Dewetting by hole growth on a rigid solid 13
1.7 Plane stress equilibrium 18
1.8 Plane stress equilibrium on a triangular segment 20
1.9 Variation of tension in a film with respect to orientation 21
1.10 Bending vs. stretching 23
1.11 Physically crosslinked elastomers 28
1.12 Partial wetting on a soft solid 36
1.13 Partial wetting on a free-standing film 39
1.14 Neumann construction on a free-standing film 40

2.1 Free-standing sample with isotropic tension 47
2.2 Uniaxial straining set-ups 48
2.3 Biaxial straining set-up 51
2.4 Methods of droplet deposition 52
2.5 Side view contact angle measurement 54
2.6 Interferometric contact angle measurement 55

Chapter 1

Introduction

Surface tension is a fundamental physical property which characterizes the interface between two phases. In fact, surface tension lies at the heart of several everyday phenomena, such as water striders roaming on the surface of water or the spherical shape assumed by a rain drop on a car's windshield. Despite these canonical examples which serve as evidence for its influence, the magnitude of the capillary force is relatively insignificant in comparison to other forces we experience on macroscopic length scales. The same cannot be said at small length scales. Although a rigid windshield remains completely undeformed by the capillary forces of the droplet acting on its surface, at submillimetric scales, surface tension forces are often significant enough to deform solid structures. In particular, these forces play an important role in the context of micro- and nanotechnologies. For instance, microelectromechanical systems (MEMS), which are used for countless applications, contain numerous compliant solid structures, such as cantilevers, thin walls, and rods. Since MEMS devices are often processed by rinsing with a liquid, capillary forces may induce large-scale deformations of the flexible structures within, destroying the integrity of the device [1]. Similar detrimental effects can be seen in other systems of comparable scale, such as in the collapse of soft microfluidic channels or bundling of vertically aligned nanowire "carpets" [2–4]. Therefore, it is of fundamental importance to understand the influence of surface tension forces on compliant solid structures. To purpose of this thesis is to further our understanding of the interaction between capillary forces and compliant structures by studying wetting on thin solid films under tension.

This chapter lays the foundation of the thesis, providing the essential concepts and equations needed to fully understand the research performed during my PhD. This introduction will begin with a discussion on surface tension (Section 1.1), which can be equivalently described as an energetic cost and a tensile force for a fluid-fluid interface. Section 1.2 will provide a background on wetting phenomena. The focus will be on describing partial wetting on rigid solid and liquid substrates, as well as providing an overview of viscous dewetting of a thin liquid film on a rigid solid. In Section 1.3, fundamentals of elasticity will be reviewed, chiefly in the context of solid films. A digression into the surface energy of solid materials is contained in Section 1.4. There, the Shuttleworth equation is introduced, and with it, the notion that the energtic cost and tensile force for a solid interface are not necessarily equal. Finally, in Section 1.5, principles of "elastocapillarity" - the interaction between surface tension and elasticity, are discussed. This section will home in on the interaction between liquids and compliant solid structures, particularly solid films.

1.1 Surface tension

Water striders and other small insects dwell on the surface of water. In a well-mixed vinaigrette, the oil droplets, surrounded by vinegar, are spherical in shape. Plants are able to transport water from their roots to be delivered to leaves at a great height. These seemingly disconnected phenomena are all manifestations of a single physical property: surface tension. Although we typically think of surface tension as a property of liquids, it is a property of an interface between any two unique phases. However, as we will see in Section 1.4, there are some caveats that must be considered when at least one of the phases is a solid. Therefore, to simplify the discussion in this section, we will focus on fluid-fluid interfaces. In this context, surface tension can be equivalently thought of as an energetic cost of forming an interface or a tensile force at the interface.

1.1.1 Energetic cost of forming interface

In the liquid state, molecules are in a condensed phase in which they are constantly interacting with other nearby molecules. The liquid is disordered, and it is different

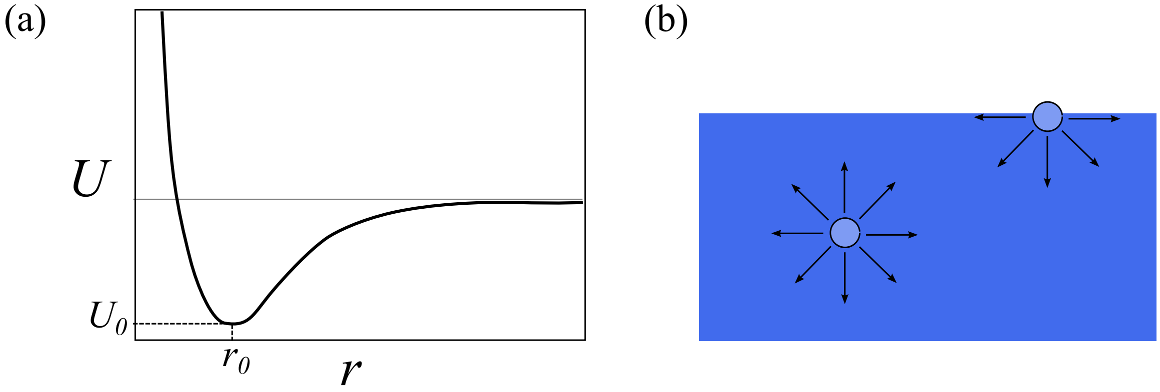

Figure 1.1: (a) A typical intermolecular potential between two liquid molecules. (b) Schematic comparing the isotropic intermolecular interactions felt by a liquid molecule in the bulk with those felt at the surface.

from a solid as the molecules are constantly changing in their relative positions and rearranging globally. Molecules in a liquid are subject to two types of intermolecular interactions, an attractive interaction and a steric repulsion. The steric repulsion, which is strong and short range, is a result of the electron clouds of the molecules overlapping and originates from the Pauli Exclusion Principle [5]. The attractive potential is longer ranged and could originate from van der Waals interactions for a non-polar liquid such as oil, or could stem from polar interactions such as hydrogen bonding for liquids like water. The total interaction potential U between molecules may be schematically depicted as in Fig. 1.1(a). The molecules in the liquid tend to be found at separations r_0 corresponding to the location of the minimum of the potential well, and, on average, the molecules are bound to one another by a potential energy of magnitude U_0. If we now consider a molecule at the surface between a liquid and air, as seen in Fig. 1.1(b), it has been stripped of roughly half its interactions that it had in the bulk, and finds itself in an energy state of order U_0 higher than in the bulk. The same principle applies for an interface between two different liquids, because the attractive interactions are typically stronger between molecules that are identical compared with other molecules, and forming an interface implies replacing the interactions with like molecules for less favourable ones [5]. As such, forming an interface is associated with an energetic cost per unit area, and is quantified by the surface tension γ_{AB} for the interface between A and B. In the special case of a liquid

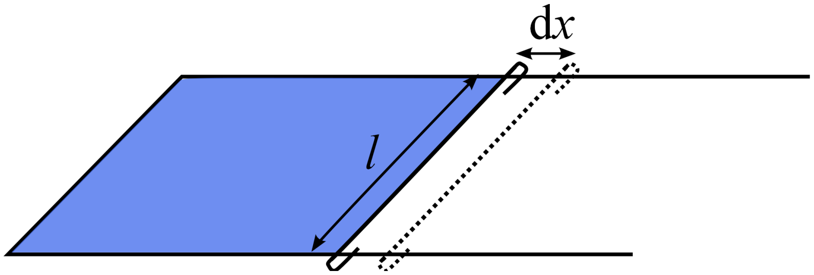

Figure 1.2: A liquid film framed on three sides by a U-shaped rigid wire and on the fourth side by a wire capable of translating. In the thought experiment, the translatable wire is displaced to the right by a distance dx.

that shares an interface simply with air, which necessarily contains the vapour of the liquid, the typical notation γ_{lv} where "l" and "v" denote liquid and vapour, is often replaced simply with γ.

Thermodynamically, the surface tension, also referred to as the surface energy, is found through a derivative of the Helmholtz free energy $\mathcal{F}$ with respect to the change in interfacial area A at constant temperature (T), volume (V), and number of particles (n) [5,6]:

$$\gamma_{\mathrm{AB}} = \left(\frac{\partial \mathcal{F}}{\partial A}\right)_{T,V,n}. \tag{1.1}$$

The fact that creating interface comes with an energetic penalty leads to the general principle that liquids are driven to minimize their interfacial area. It is for this reason, for instance, that oil droplets in vinaigrette (described earlier) are spherical.

1.1.2 A force parallel to the interface

In a thought experiment, we imagine a liquid membrane (e.g. a soap film) that is framed on three sides by a wire bent into a U-shape (as seen in Fig. 1.2), and on its fourth side, the liquid film is framed by a straight wire of length l that is able to translate in the direction indicated. If we imagine translating the straight wire to the right by a distance dx, this increases the interfacial area of the liquid film by an amount $2l\mathrm{d}x$. The factor of two arises as there are liquid-air interfaces both on the top and bottom side of the film. This increase in interfacial area implies a proportional increase in the surface free energy ($\delta\mathcal{F}_\gamma$) of the liquid

$$\delta\mathcal{F}_\gamma = 2l\mathrm{d}x\,\gamma\,. \tag{1.2}$$

Of course, this increase in free energy implies that work (δW) must have been done on the system:

$$\delta W = F\,\mathrm{d}x\,, \tag{1.3}$$

where F is the force applied to move the rod at a constant speed. If we equate Eq. 1.2 with Eq. 1.3, we find that $F = 2\gamma l$. Thus, we see that film's surface tension causes a force per unit length which is parallel to the interface in the direction that would tend to shrink the area of the interface. Once again, the factor of two arises due to the presence of two interfaces in this example. Therefore, γ can be thought of as both an energetic cost per unit area as well as a tensile force per unit length. It is due to this tensile force that small insects are able to be supported on the surface of water.

In problems involving surface tension, there is always a duality between the energy and force descriptions. Of course, the two are completely equivalent, but it is often the case that one approach is enormously simpler than the other, as will be seen for example in Section 1.2.1. In most of the work comprising this thesis (Papers I, II and V), we have found the force picture to be the simplest approach.

The molecular origin of the tensile force is not as easily described as the energetic cost of forming interface, but is a result of the interplay between the repulsive and attractive contributations to the intermolecular interactions, and how these vary in proximity to the interface where the liquid transitions from being a bulk liquid to vapour [7–9]. These considerations are most clearly elucidated using molecular dynamics simulations, where particles are subject to the Lennard-Jones potential (which has a form akin to that drawn in Fig. 1.1(a)). At the interface, these simulations clearly show the existence of a tensile force parallel to the interface which is spread over a few molecular diameters, comparable to the thickness of the region where the density changes from bulk liquid to vapour, i.e. the interfacial width [8–10].

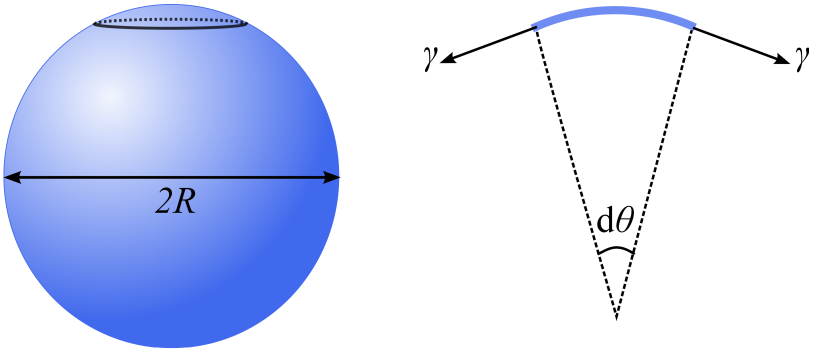

Figure 1.3: A small surface section of a liquid sphere of radius R (left) experiences surface tension forces per unit length parallel to the interface at its perimeter (right). The result of this force per unit length, when integrated around the cap's perimeter, is a net inwards force.

1.1.3 Laplace pressure

Across any curved liquid interface, there exists a pressure jump called the "Laplace pressure". To see why this pressure jump exists, we consider a liquid droplet of radius R, as seen in Fig. 1.3. We consider an infinitesimal cap of this droplet's surface, shown in profile in Fig. 1.3, defined by a cone angle $\mathrm{d}\theta$. The surface tension of the liquid surrounding this section exerts a tensile force pulling on the cap surface parallel to the interface. The net result is a force per unit length of magnitude $\gamma\mathrm{d}\theta/2$ directed radially inward. The total force (F_γ) is found by multiplying by the perimeter of the cap to be:

$$F_\gamma = \frac{\pi R\gamma}{2}\mathrm{d}\theta^2\,. \tag{1.4}$$

Under the action of surface tension alone, there would be a net inward force on the droplet's surface causing it to collapse, and hence minimize surface area. To maintain the droplet in equilibrium, there is an overpressure ΔP_L within the droplet compared to the outside pressure. This Laplace pressure can be found by dividing Eq. 1.4 by the surface area of the cap $\pi R^2\mathrm{d}\theta^2/4$:

$$\Delta P_\mathrm{L} = \frac{2\gamma}{R}\,. \tag{1.5}$$

The same result can easily be obtained from an energetic picture. This expression can be generalized for any fluid-fluid interface with two principal radii of curvature R_1, R_2 and of interfacial tension γ_{AB}:

$$\Delta P_{\mathrm{L}} = \gamma_{AB}\left(\frac{1}{R_1} + \frac{1}{R_2}\right) = 2\gamma_{AB}C\,, \tag{1.6}$$

where C is the mean curvature of the surface. Applying this principle, it is clear that soap films must always assume a surface described by a zero curvature, since the atmospheric pressure on either side of the film is the same [6, 11]. These are called minimal surfaces as they are ones that minimize surface area. In addition, static liquid volumes that are subject to no external body forces such as gravity, must sustain a constant pressure within their volume (otherwise, the liquid would flow). Therefore, all of its liquid-fluid interfaces must have a constant value of $\gamma_{AB}C$, in order to maintain a constant Laplace pressure within the entire volume.

1.1.4 The gravity capillary length

Although capillarity drives liquids to minimize interfacial area, gravity drives liquids to flatten. For instance, puddles are liquid volumes that are flattened by gravity and contain a great deal of interface. To further understand the interplay between gravity and capillarity, we compare the pressure due to each force within a droplet. Gravity creates a hydrostatic pressure difference (ΔP_{g}) between the top and bottom of a droplet of radius R of magnitude:

$$\Delta P_{\mathrm{g}} = 2\rho_{\mathrm{l}} g R\,, \tag{1.7}$$

where ρ_{l} is the density of the liquid and g is the acceleration due to gravity. Equating the Laplace pressure within the drop given by Eq. 1.5 with Eq. 1.7, and solving for the droplet radius yields what we will refer to as the gravity capillary length L_{GC} [6]:

$$L_{\mathrm{GC}} = \sqrt{\frac{\gamma}{\rho_{\mathrm{l}} g}}\,. \tag{1.8}$$

For length scales much smaller than L_{GC}, capillarity dominates and liquids are driven to minimize their interfacial energy (subject to volume constraints). For length scales much larger than L_{GC}, gravity forces liquids to flatten. The gravity capillary length of water is approximately 2 mm. This length scale is traditionally referred to as simply the "capillary length" [6], but the nomenclature we have chosen here will better distinguish it from other length scales that will be discussed. In all the work contained in this thesis, droplet sizes are sufficiently small that gravity can be safely neglected. Unless otherwise stated, all further discussion will be in the context where gravity can be neglected.

1.2 Wetting

Wetting describes how a liquid deposited on a solid (or liquid) substrate spreads out [6, 12]. It is a vast field, motivated by a multitude of industrial applications ranging from designing tires with better adhesion on wet roads, creating textiles that perform well in rainy conditions, to developing chocolate powder that dissolves readily in milk. An important parameter in this context is the spreading parameter S, which describes the difference in surface energy per unit area of a solid substrate when it is dry compared to when it is wet by a liquid film:

$$S = \gamma_{\mathrm{sv}} - \gamma_{\mathrm{sl}} - \gamma \,, \tag{1.9}$$

where γ_{sv} and γ_{sl} are the interfacial energies of the solid-vapour and solid-liquid interfaces [6, 12]. Although γ_{AB} for interfaces involving solids are sometimes referred to as interfacial tensions as well, one must use caution in thinking of these quantities as tensile forces for reasons that will become clear in Section 1.4. For a liquid substrate being wet by another immiscible liquid, the solid "s" is simply replaced by a substrate liquid "$\mathrm{l_s}$". When $S > 0$, it is energetically favourable for a liquid deposited on a surface to spread completely and form a liquid film that coats the substrate, and hence is referred to as "total wetting". On the other hand, when $S < 0$, the liquid assumes the shape of a spherical cap on a solid substrate when in its lowest free energy state. This case is referred to as "partial wetting".

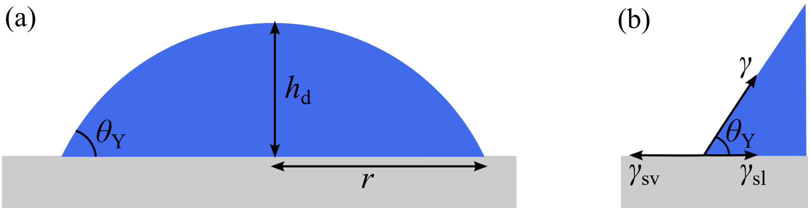

Figure 1.4: Partial wetting between a liquid droplet and a rigid solid substrate. (a) The droplet assumes the shape of a spherical cap with the indicated height h_d, contact radius r, and contact angle θ_Y. (b) The interfacial tension balance to derive the Young-Dupré equation.

1.2.1 Partial wetting on a rigid solid

When a liquid droplet is deposited on a rigid solid substrate, it assumes the shape of a spherical cap with contact angle θ_Y, as depicted in Fig. 1.4(a). The equilibrium contact angle can be determined by minimizing the interfacial energy of the solid-liquid-vapour system. For the calculation, we consider a spherical cap droplet with base radius r and height h_d [13]. The free energy of a partially wet substrate relative to its dry state is given by $\mathcal{F}$:

$$\mathcal{F} = \big(\gamma_\mathrm{sl} - \gamma_\mathrm{sv}\big) A_\mathrm{sl} + \gamma A_\mathrm{lv} \,, \tag{1.10}$$

where A_sl and A_lv are the surface areas of the solid-liquid and liquid-vapour interfaces of the droplet. $A_\mathrm{sl} = \pi r^2$ is the base area of the droplet, and $A_\mathrm{lv} = \pi r^2 + \pi h_\mathrm{d}^2$ is the surface area of the spherical segment of the cap. The volume (Ω) of the liquid cap is:

$$\Omega = \frac{1}{6}\pi h_\mathrm{d}\big(3r^2 + h_\mathrm{d}^2\big) \,, \tag{1.11}$$

and must be held constant when the free energy is minimized. We minimize Eq. 1.10 with respect to r at constant Ω to yield:

$$\left(\frac{\partial \mathcal{F}}{\partial r}\right)_\Omega = 0 = \big(\gamma_\mathrm{sl} - \gamma_\mathrm{sv}\big)(2\pi r) + \gamma\Big(2\pi r + 2\pi h_\mathrm{d}\frac{\mathrm{d}h_\mathrm{d}}{\mathrm{d}r}\Big) \,. \tag{1.12}$$

The derivative $\frac{\mathrm{d}h_\mathrm{d}}{\mathrm{d}r}$ can be evaluated by implicit differentiation of Eq. 1.11:

$$\frac{\mathrm{d}\Omega}{\mathrm{d}r} = 0 = \pi h_\mathrm{d} r + \frac{\pi}{2}\frac{\mathrm{d}h_\mathrm{d}}{\mathrm{d}r}(r^2 + h_\mathrm{d}^2) \tag{1.13}$$

$$\frac{\mathrm{d}h_\mathrm{d}}{\mathrm{d}r} = \frac{-2h_\mathrm{d} r}{r^2 + h_\mathrm{d}^2}\,. \tag{1.14}$$

Substituting Eq. 1.14 into Eq. 1.12 gives:

$$0 = \left(\gamma_\mathrm{sl} - \gamma_\mathrm{sv}\right)(2\pi r) + \gamma(2\pi r)\left(\frac{r^2 - h_\mathrm{d}^2}{r^2 + h_\mathrm{d}^2}\right). \tag{1.15}$$

Making use of the spherical cap identity $\cos\theta_\mathrm{Y} = (r^2 - h_\mathrm{d}^2)/(r^2 + h_\mathrm{d}^2)$ [13], we arrive at the Young-Dupré equation [14]:

$$\gamma\cos\theta_\mathrm{Y} = \gamma_\mathrm{sv} - \gamma_\mathrm{sl}\,. \tag{1.16}$$

Thus, we see that by measuring the contact angle of a liquid of known surface tension on a solid, we attain information regarding the energetics of the solid-liquid and solid-vapour interfaces.

Although it is feasible to derive the Young-Dupré equation from an energetic picture, it is much simpler in the force description. We imagine zooming in around the contact line, such that the liquid can be described as a wedge subtending an angle θ_Y to the substrate, as schematized in Fig. 1.4(b). As indicated, if we proceed with the notion that these interfacial tensions can be thought of as tensile forces, the three tensions of the system are tugging at the contact line. Balancing these in the horizontal direction, we immediately recover the Young-Dupré equation. In the force description, it appears as if the vertical component at the contact line remains unbalanced. In fact, the balancing vertical force $\gamma\sin\theta$ is provided by the elasticity of the substrate itself [6,9,15]. Thus, the solid is also being subjected to a vertical force $\gamma\sin\theta$, but since it is infinitely rigid here, it remains undeformed. As we will see in Section 1.5.1, if the solid substrate is soft, the deformation can become significant.

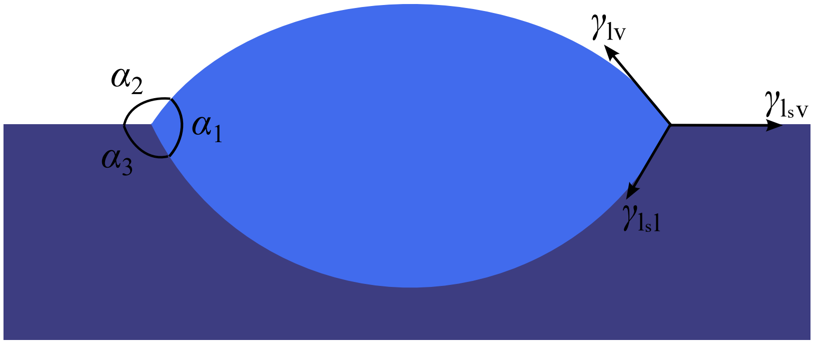

Figure 1.5: Partial wetting between a liquid droplet and a liquid substrate. The two droplet interfaces take the shape of spherical caps with different radii of curvature. The angles subtended between the three interfaces at the contact line are set by a Neumann construction balancing the three interfacial tensions of the system.

1.2.2 Partial wetting on a liquid

In contrast with the rigid solid, in the case of a liquid substrate, its interface is completely deformable. When a liquid droplet is deposited on an immiscible liquid substrate, it assumes the shape of a lens, as shown in Fig. 1.5 [6, 16]. The two interfaces of the liquid lens are spherical caps with different radii of curvature. In the absence of gravity (i.e. for droplet sizes $\ll L_{\text{GC}}$), the liquid substrate remains completely planar surrounding the droplet. If gravity is considered, the substrate interface becomes depressed near the contact line for droplets that are denser than the liquid bath and raised for droplets that are less dense [16]. The angles subtended between the three different interfaces can once again be determined by appealing to a balance of interfacial tensions at the contact line, as depicted in Fig. 1.5. The important distinction from the solid substrate is that the substrate is not elastic, and hence, the force balance must be simultaneously performed in the vertical and horizontal directions. As an example, using the cosine law, the internal angle α_1 subtended by the interfaces of the lens is given by:

$$\cos\alpha_1 = \frac{\gamma_{\text{l}_\text{s}\text{v}}^2 - \gamma_{\text{lv}}^2 - \gamma_{\text{l}_\text{s}\text{l}}^2}{2\gamma_{\text{lv}}\gamma_{\text{l}_\text{s}\text{l}}}\,. \tag{1.17}$$

Therefore, if the surface tensions of the the two liquids with vapour are known, it is possible to determine the interfacial tension between them by measuring α_1 (or α_2 or

α_3).

For droplet sizes $\ll L_{\mathrm{GC}}$, we know from Section 1.1.3 that the Laplace pressure must be constant within the liquid. Since gravity can be neglected, the ambient pressure of the vapour and the liquid bath below the lens is identical. Thus, the Laplace pressure across both interfaces must be equal:

$$\Delta P_{\mathrm{L}} = \frac{2\gamma_{\mathrm{lv}}}{R_{\mathrm{lv}}} = \frac{2\gamma_{\mathrm{l_sl}}}{R_{\mathrm{l_sl}}} \tag{1.18}$$

$$\frac{\gamma_{\mathrm{l_sl}}}{\gamma_{\mathrm{lv}}} = \frac{R_{\mathrm{l_sl}}}{R_{\mathrm{lv}}} \tag{1.19}$$

where R indicates the radius of curvature of the interface. The same result can be obtained by balancing the vertical component of the interfacial tensions at the contact line.

1.2.3 Dewetting

When $S < 0$, it is energetically favourable for a thin liquid film on a solid substrate to retract and eventually form droplets on the surface of the solid, a process termed "dewetting". In order for a flat liquid film to initiate the transition into droplets, it necessitates an intermediate step in which the liquid-vapour interface of the film is deformed, which increases the interfacial area of the system. Generally, films are subject to an increase in surface energy in this intermediate step, and as such, are metastable. In films thinner than ~ 100 nm, the surface energies are modified by long-range interactions, such as van der Waals forces between the solid and liquid molecules [6,17]. Under certain circumstances, these interactions can cause such thin liquid films to become wholly unstable, and dewetting initiates spontaneously by amplification of surface modulations through thermal fluctuations, which eventually reach the solid substrate [6, 17–21]. This process is called "spinodal dewetting". On the other hand, metastable films dewet by nucleation and subsequent growth of a dry spot (hole in liquid) [6, 17, 19, 20, 22–24]. Dewetting may be initiated by defects (heterogeneous nucleation), such as dirt particles, or by nucleation through a large enough thermal fluctuation (homogeneous nucleation) [17,25,26]. Homogeneous

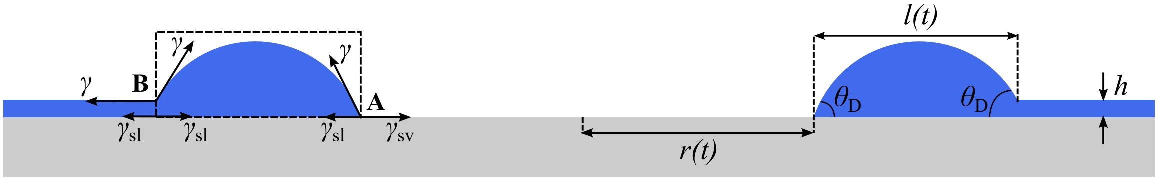

Figure 1.6: A schematic of a thin liquid film dewetting by nucleation and growth of holes off a rigid substrate. The interfacial tensions acting at contact lines **A** and **B** are indicated. The dashed box around the left rim represents treating the rim as a rigid body.

nucleation is typically not seen, as it requires extremely thin (a few nanometers) and clean liquid films. In nucleated dewetting, holes are cylindrical in shape, and the displaced liquid accumulates in a rim surrounding the hole.

To gain some insight into the dynamics, we present a slightly simplified version of the model of viscous dewetting presented in Refs. [6, 19, 24], which describes the growth of nucleated holes in a viscous liquid film on a rigid solid substrate on length scales $\ll L_{\rm GC}$. The hole growth is schematized in Fig. 1.6, where the width of the rim with time is indicated as $l(t)$ and the radius of the hole is $r(t)$. We begin with a few geometrical assumptions, as follows. The rims are circular in cross-section as the pressure is thought to be constant within the rim, and according to Laplace's law, their surface must have a constant curvature. We are interested in sufficiently late times that the rims have accumulated enough material to be much larger than the thickness of the liquid film, h. As such, the angles that the circular cap rims subtend to the solid substrate and to the liquid film (on either side) are roughly equal, and given by $\theta_{\rm D}$. We assume that $\theta_{\rm D}$ and $\theta_{\rm Y}$, the equilibrium contact angle of the liquid on the solid, are small angles.

We are interested in the growth of the hole with time: $r(t)$, but must begin with a scaling argument for the width of the rim. The rim collects all the liquid material that the hole displaces. The volume of liquid displaced by the hole is approximately $\sim hr^2$. At the scaling level, the volume held within the rim is roughly $\sim rl^2\theta_{\rm D}$. Assuring volume conservation implies:

$$l \sim \sqrt{\frac{hr}{\theta_{\mathrm{D}}}} \tag{1.20}$$

$$\frac{\mathrm{d}l}{\mathrm{d}t} \sim \sqrt{\frac{h}{\theta_{\mathrm{D}} r}} \frac{\mathrm{d}r}{\mathrm{d}t} \,. \tag{1.21}$$

Since we are dealing with thin films and late times, $h \ll r$. Together with Eq. 1.20 and Eq. 1.21, it implies that $l \ll r$ and $\frac{\mathrm{d}l}{\mathrm{d}t} \ll \frac{\mathrm{d}r}{\mathrm{d}t}$ at these times. Thus, for the sake of this model, the increase in rim width is treated to be negligible in comparison to the growth in hole radius, i.e. l is roughly constant. This approximation is in good agreement with experimental data [24].

In Fig. 1.6, we label the three phase contact line as **A** and the contact line with the liquid film as **B**. All the interfacial tensions acting at these two contact lines are shown. Since the rim is not changing in shape, we treat it as a rigid body (indicated by the dashed square in Fig. 1.6) and evaluate the net external force acting upon it. Interfacial tensions provide a net force per unit length on the rim given by:

$$F_\gamma = \gamma + \gamma_{\mathrm{sl}} - \gamma_{\mathrm{sv}} \tag{1.22}$$

directed radially outward from the hole's center. This unbalanced force on the rim serves as the driving force for dewetting. The power (per unit length) of this driving force is $P_\gamma = F_\gamma v$, where $v = \mathrm{d}r/\mathrm{d}t$ is the speed of the rim. Using Young-Dupré's law (Eq. 1.16), P_γ can be re-written as:

$$P_\gamma = \gamma v \big(1 - \cos\theta_{\mathrm{Y}}\big) \,. \tag{1.23}$$

Note that if $\theta_{\mathrm{D}} = \theta_{\mathrm{Y}}$, the interfacial energies at the three phase contact line (**A**, as seen in Fig. 1.6) would be balanced and the contact line would remain static, as in Section 1.2.1. We must have $\theta_{\mathrm{D}} < \theta_{\mathrm{Y}}$ in order for the interfacial energies acting at **A** to generate a net driving force for dewetting. In the limit of small angles, Eq. 1.23

simplifies to:

$$P_\gamma = \frac{\gamma v \theta_\mathrm{Y}^2}{2} \,. \tag{1.24}$$

Although the driving force could feed into the rim's kinetic energy when the dewetting liquid is highly inviscid [27], our focus here will be on viscous dewetting, since most dewetting studies are carried out with highly viscous fluids and at small length scales, and are thus characterized by a low Reynolds number[1]. In this regime, the power done by the driving force is immediately dissipated by viscous shear in the fluid [6,19,24,28]. In the presence of a three phase contact line, the viscous dissipation is generally concentrated right at the contact line [6, 12]. This is because viscous liquids must be stationary at a solid/liquid interface (known as the no-slip boundary condition), and hence, there is an enormous viscous shear in a moving contact line. The power expended in viscous dissipation (per unit length) in a moving contact line (P_η) is given by:

$$P_\eta \propto \frac{\eta v^2}{\theta_\mathrm{D}} \,, \tag{1.25}$$

where η is the viscosity and v is the speed of the contact line, equal to the hole growth speed in this case [6,12]. The constant of proportionality for Eq. 1.25 contains information regarding the molecular details of the contact line. Equating P_γ and P_η, we find that $v \propto \gamma\theta_\mathrm{D}\theta_\mathrm{Y}^2/\eta$. In a more thorough treatment of this problem, the balance between driving force and dissipation is considered separately for the two contact lines of the rim (with solid and with liquid film) [6, 19, 24]. Employing the fact that θ_D and v are approximated to be the same for each contact line, one can show in that approach that $\theta_\mathrm{D} \propto \theta_\mathrm{Y}$. Thus, we arrive at our final result:

$$v \propto \frac{\gamma \theta_\mathrm{Y}^3}{\eta} \,. \tag{1.26}$$

This canonical model for viscous dewetting, which is in good agreement with experi-

---

[1] The Reynolds number is a dimensionless number that quantifies the relative importance of inertial forces to viscous forces in fluid flow [28]. The approximate Reynolds number of the experiment from the study wherein this theoretical model was first tested was $\sim 1 \cdot 10^{-5}$, indicating that inertial forces could safely be ignored [24].

mental data [24], demonstrates that the radius of holes increases linearly in time.

Dewetting experiments are frequently carried out with polymer melts, as these liquids offer numerous practical advantages [17]. First and foremost, they have an accessible glass-transition temperature, above which the polymer behaves as a liquid, and below which the polymer behaves as a solid [5,17,29]. This property implies that the dewetting process can be "paused" and "resumed" by changing the temperature of the sample. When the sample is glassy, it is feasible to measure the morphology of the dewetting structures using probes such as atomic force microscopy (AFM) (see, for example, Refs. [25, 30–35]). The viscosity of polymer melts changes with temperature [5, 29], so the rate of the dewetting dynamics can be controlled using this variable. Thin, clean, and highly uniform polymer films can be prepared by a variety of techniques, permitting a robust initial condition for dewetting experiments. Finally, polymer melts are non-volatile and relatively inert at typical experimental temperatures [17].

Dewetting can be used to study physical properties of the solid-liquid system. Dewetting experiments can act as a probe of rheological properties of viscoelastic materials [32, 36], residual stresses from sample preparation of polymer films [30, 33], and van der Waals interactions between solid and liquid molecules [26,37,38]. Furthermore, on certain substrates, polymer melts violate the no-slip boundary condition. Information about this slippage of liquid at the solid interface can be obtained from dewetting experiments, as it causes important deviations from the constant speed of Eq. 1.26 [25, 31, 34, 35, 39, 40]. Dewetting can also be exploited to engineer patterns at microscopic length scales. Using a combination of chemical and topographical patterning of the substrate, dewetting can be guided to obtain novel morphologies (see for example Refs. [41–47]).

1.3 Elasticity of solid films

In the work comprising this thesis, basic results and concepts relating to continuum elasticity are employed. In this section, I will provide a cursory overview of the most important concepts and equations required to digest these principles. For a more detailed overview of continuum elasticity, the reader is referred to Refs. [48, 49].

1.3.1 Hooke's law

When a bulk solid is subjected to external forces, its deformation can be described using the strains ϵ_x, ϵ_y, ϵ_z which describe the unit elongation of an element of the material along each axis, and the shearing strains s_{xy}, s_{xz}, s_{yz} which describe the unit shear of an element of the material in each plane. When the solid is deformed, it also builds up internal elastic normal stresses: σ_x, σ_y, σ_z, and shearing stresses: τ_{xy}, τ_{xz}, τ_{yx}, τ_{yz}, τ_{zx}, τ_{zy}. By requiring that each solid element in equilibrium must be subject to zero net torque, it is straightforward to show $\tau_{xy} = \tau_{yx}$, $\tau_{xz} = \tau_{zx}$, and $\tau_{yz} = \tau_{zy}$, and hence, only six quantities are required to describe the elastic stresses on a solid element [48].

There is an empirically established relationship that relates the normal stresses and strains, which is known as Hooke's law. Hooke's law is typically only valid in a range of small strains which depends on the material in question. Hooke's law for an isotropic material in the context of continuum elasticity can be written as

$$\epsilon_x = \frac{1}{E}\big[\sigma_x - \nu(\sigma_y + \sigma_z)\big] \tag{1.27a}$$

$$\epsilon_y = \frac{1}{E}\big[\sigma_y - \nu(\sigma_x + \sigma_z)\big] \tag{1.27b}$$

$$\epsilon_z = \frac{1}{E}\big[\sigma_z - \nu(\sigma_x + \sigma_y)\big] , \tag{1.27c}$$

where ν is Poisson's ratio and E is the Young's modulus of the material which quantifies its stiffness, and will be an important parameter in Section 1.5. When a solid material is stretched in one direction, it contracts in the orthogonal directions. This property is incorporated in Hooke's law (e.g. setting $\sigma_x > 0$, $\sigma_y = 0$ and $\sigma_z = 0$, you find $\epsilon_y < 0$ and $\epsilon_z < 0$ for $\nu > 0$), and is controlled by ν. Most materials have $0 < \nu < 0.5$, where the upper limit $\nu = 0.5$ describes a perfectly incompressible material (volume is conserved). Similar equations exist for the shearing components

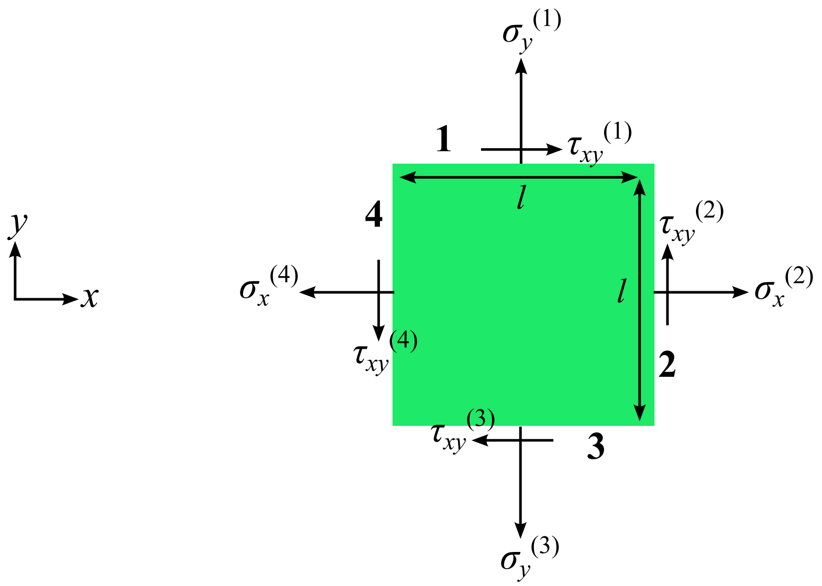

Figure 1.7: Equilibrium of stresses acting on a square segment in the plane of a solid in plane stress.

of stress and strain:

$$\tau_{xy} = \frac{1}{G} s_{xy}\,, \quad \tau_{xz} = \frac{1}{G} s_{xz}\,, \quad \tau_{yz} = \frac{1}{G} s_{yz}\,, \tag{1.28}$$

where G is the shear modulus of the material, and one can show that $G = E/2(1+\nu)$.

1.3.2 Plane stress

When the solid takes the form of a thin plate or film, numerous simplifcations to the elastic considerations emerge. One such simplification is in the case of "plane stress", wherein all the elastic stresses within the thin plate or film, which is presumed to lie in the xy-plane, act in the plane of the solid. In other words, there are no stress components in the out-of-plane direction, i.e. $\sigma_z = \tau_{xz} = \tau_{yz} = 0$. Thus, the state of stress within the film is described completely by σ_x, σ_y, and τ_{xy}. To derive the condition for equilibrium in plane stress, we consider the elastic forces acting on a square segment of side length l in the plane of the plate, as seen in Fig. 1.7. In the absence of body forces such as gravity, the elastic forces acting on each of the four sides must balance one another in x and y respectively:

$$\left(\sigma_x^{(2)} hl - \sigma_x^{4)} hl\right) + \left(\tau_{xy}^{(1)} hl - \tau_{xy}^{(3)} hl\right) = 0 \tag{1.29a}$$

$$\left(\sigma_y^{(1)} hl - \sigma_y^{3)} hl\right) + \left(\tau_{xy}^{(2)} hl - \tau_{xy}^{(4)} hl\right) = 0\,, \tag{1.29b}$$

where h is the film's thickness, assumed to be uniform, and the superscripts label the side of the square segment, as seen in Fig. 1.7. Shrinking the square segment to be infinitesimal in size, one derives the following equilibrium conditions:

$$\frac{\partial \sigma_x}{\partial x} + \frac{\partial \tau_{xy}}{\partial y} = 0 \tag{1.30a}$$

$$\frac{\partial \sigma_y}{\partial y} + \frac{\partial \tau_{xy}}{\partial x} = 0\,. \tag{1.30b}$$

When a thin plate or film is loaded by forces applied to to its boundaries, which are uniformly distributed over its thickness and are oriented parallel to plane of it, it is in a state of plane stress. In this case, the elastic stresses are also constant across the film's thickness, and the tensions in the film can be calculated as:

$$T_x = \sigma_x h\,, \quad T_y = \sigma_y h\,, \quad T_{xy} = \sigma_{xy} h\,, \tag{1.31}$$

where h is the thickness of the film, assumed to be constant. For the remainder of this subsection, we will consider this state of plane stress wherein the film is loaded in the plane and experiences no out-of-plane deformation.

Principal directions

If the tension components in x and y (i.e. T_x, T_y, and T_{xy}) are known, these can be used to calculate the tension components in any other pair of orthogonal directions (n,n') in the plane. As shown in Fig. 1.8, we imagine a balance of the elastic forces

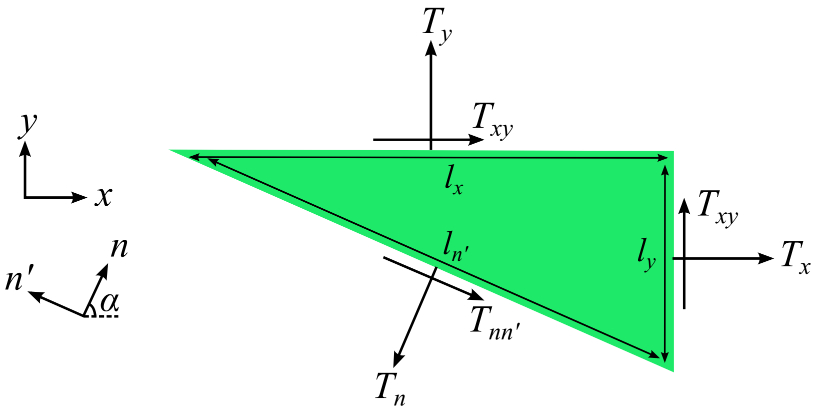

Figure 1.8: Equilibrium of tensions acting on a triangular segment in the plane of a solid in plane stress.

acting on a triangular segment of the film. Balancing the forces in the n direction:

$$0 = -T_n l_{n'} + T_x \cos\alpha \, l_y + T_y \sin\alpha \, l_x + T_{xy} \sin\alpha \, l_y + T_{xy} \cos\alpha \, l_x \tag{1.32}$$

where α is the angle between the x- and n-axes, and l_x, l_y, $l_{n'}$ are side lengths of the triangular segment depicted in Fig. 1.8 which multiply the tensions to yield forces. Noting that $l_x = l_{n'} \sin\alpha$ and $l_y = l_{n'} \cos\alpha$, we find:

$$T_n = T_x \cos^2\alpha + T_y \sin^2\alpha + 2T_{xy} \sin\alpha \cos\alpha \,. \tag{1.33}$$

Similarly, performing the force balance in the n' direction yields:

$$T_{nn'} = \left(T_y - T_x\right) \sin\alpha \cos\alpha + T_{xy}\left(\cos^2\alpha - \sin^2\alpha\right) . \tag{1.34}$$

From Eq. 1.34, it is clear that we can always find an angle α such that the shear component vanishes. Setting $T_{nn'} = 0$, we can find:

$$\frac{T_{xy}}{T_x - T_y} = \frac{\sin\alpha \cos\alpha}{\cos^2\alpha - \sin^2\alpha} = \tan 2\alpha \,. \tag{1.35}$$

From the above equation, two orthogonal directions (defined by values of α) can be found for which there is no shearing component of the tension. Those special directions are referred to as "principal directions" and the stresses, strains and tensions

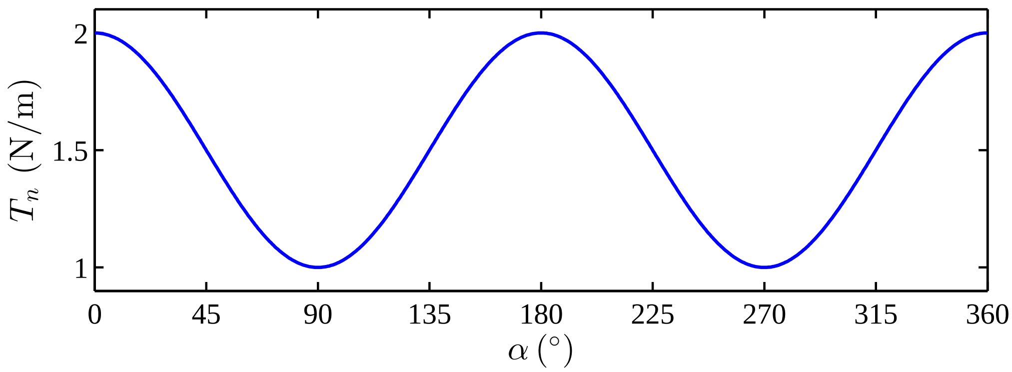

Figure 1.9: Plot of tension in the general direction n oriented at angle α to the x-axis of the film. In this plot, we have set $T_x = 2$ N/m and $T_y = 1$ N/m as an example.

in those directions are also prefaced by the word "principal". For instance, if a film with isotropic tension ($T_y = T_x = T$) is subjected to a pure shear ($T_{xy} > 0$), the principal directions are oriented at 45° to the x- and y-axes. It is often convenient to orient, or choose, the x- and y- axes to align with the principal directions [48]. As such, $T_{xy} = 0$, and Eq. 1.33 and Eq. 1.34 become:

$$T_n = T_x \cos^2\alpha + T_y \sin^2\alpha \tag{1.36}$$

$$T_{nn'} = \left(T_y - T_x\right) \sin\alpha \cos\alpha \,. \tag{1.37}$$

The result of Eq. 1.36 is plotted in Fig. 1.9 for $T_x = 2$ N/m and $T_y = 1$ N/m as an example. As demonstrated by Eq. 1.36, and exemplified by Fig. 1.9, the principal directions always coincide with the directions of highest and lowest tension. In addition, the tension is invariant upon a 180° shift in α, as we would expect.

Boundary conditions

Films under plane stress can be subject to a few different boundary conditions including: clamped, fixed tension, and free. A clamped boundary means that the film's boundary is held in place at a given spot. This condition is applicable to films that are suspended between fixed rigid supports, for instance. In a fixed tension boundary, the boundary of the film is not held in place, but is rather subject to a constant external tension in plane, which generally may have components normal and tangential to the boundary. In order to be in mechanical equilibrium, the tensions must be continuous across the boundary of the film. For instance, if a film boundary is oriented such that its normal and tangent point in the directions n and n', we must at the boundary have $T_n = T_{n,\text{ext}}$ and $T_{nn'} = T_{nn',\text{ext}}$, where "ext" indicates the externally applied tension [48]. A special case of the fixed tension boundary, is a free boundary. A free boundary is not held in place nor subjected to any external tension. As such, we must have $T_n = T_{nn'} = 0$ at these boundaries. Since the shear component $T_{nn'}$ vanishes at these boundaries, it necessarily implies that n and n' are the principal directions. Since $T_n = 0$, the orthogonal direction n' must be the one of highest tension (as long as the film is under tension rather than compression). Thus, at a free boundary of a taut film, the highest tension direction is tangential to the boundary.

Hooke's law for biaxial and isotropic plane stress

We now imagine applying Hooke's law to the case of a film being strained biaxially. A method for applying biaxial strains will be described in Section 2.2.3. The film is in the xy-plane and strained directly along x and y, which implies that $s_{xy} = 0$ and hence $\tau_{xy} = T_{xy} = 0$. Thus, the principal directions coincide with the x- and y-axes. Recognizing that $\sigma_z = 0$ for plane stress, we can simplify Eq. 1.27a and Eq. 1.27b:

$$\epsilon_x = \frac{1}{E}\big[\sigma_x - \nu\sigma_y\big] \tag{1.38a}$$

$$\epsilon_y = \frac{1}{E}\big[\sigma_y - \nu\sigma_x\big]\,. \tag{1.38b}$$

We can now invert these expressions to solve for the stresses, and hence tensions, in x and y:

$$T_x = \sigma_x h = \frac{Eh\big(\epsilon_x + \nu\epsilon_y\big)}{1-\nu^2} \tag{1.39a}$$

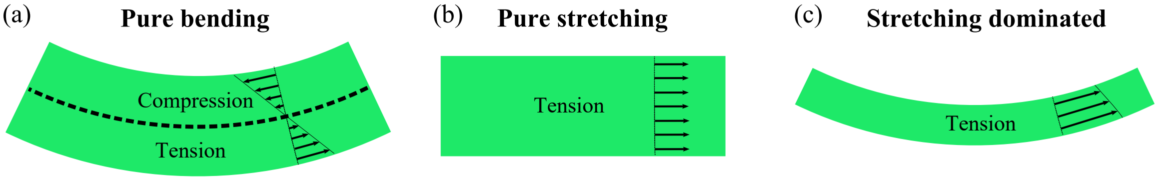

Figure 1.10: Schematics illustrating in-plane tensile and compressive plane stresses in the case of (a) pure bending, (b) pure stretching, and (c) a stretching-dominated regime.

$$T_y = \sigma_y h = \frac{Eh\left(\epsilon_y + \nu\epsilon_x\right)}{1-\nu^2}\,. \tag{1.39b}$$

Although the film is stress-free in the z direction, straining it in x and y will create a strain in the z-direction, given by:

$$\epsilon_z = \frac{-\nu}{E}\left[\sigma_x + \sigma_y\right] = \frac{\nu}{\nu - 1}\left[\epsilon_x + \epsilon_y\right]. \tag{1.40}$$

For most materials (i.e. when $0 < \nu < 0.5$), if $\epsilon_x > 0$ and $\epsilon_y > 0$ then $\epsilon_z < 0$, which implies that the film becomes thinner when strained.

The special case of isotropic tension ($T_x = T_y = T$) is attained when the film is strained equally in both principal directions ($\epsilon_x = \epsilon_y$). The tension T can be obtained from Eq. 1.39:

$$T = \frac{Eh\epsilon}{1-\nu}\,. \tag{1.41}$$

1.3.3 Transverse loading of a solid film

To this point, we have considered solid films that have been strained only in the plane of the film, assumed to lie in the xy-plane. However, it is also of great interest to consider the out-of-plane deformation of a film under the action of a transverse (or lateral) load. There are two chief modes of deformation through which a thin plate or film may deform laterally: bending and stretching [49,50]. When a thin plate or film deforms by either of these mechanisms, it is a good approximation to assume that the transverse components of the stress are negligible (i.e. $\sigma_z = \tau_{xz} = \tau_{yz} = 0$), which means that the solid is in a state of plane stress. Although flexure and stretching are generally both present, there are limits where one predominates over the other. When a plate is laterally deformed a distance much smaller than its thickness, bending typically dominates [49,50]. To understand this mechanism, we imagine a rectangular plate that is bent into a circular arc, shown in profile in Fig. 1.10(a). The typical assumption in pure bending is that the central plane of the plate (indicated by a dotted line in Fig. 1.10(a)) is undeformed (or neutral). To accomodate the shape change, the material that is on the same side of the plate as the concave surface becomes compressed, whereas the material on the other side of the neutral plane is stretched. This gradient in in-plane strain of the plate is the characteristic of bending. Pure stretching occurs only when the plate experiences a longitudinal (i.e. in-plane) tensile load, which is the case we have considered in Section 1.3.2. In pure stretching, the in-plane strain and stress exhibit no gradient across the plate's thickness, as seen in Fig. 1.10(b).

In the work comprising this thesis, the films are in a stretching-dominated state (Fig. 1.10(c)). Stretching dominates if the film is subjected to a large longitudinal tensile load before being subjected to a lateral load and/or if the film is sufficiently deformed (a distance much larger than its thickness) by the lateral load such that there is no neutral plane as all elements of the solid are under tension to accomodate the shape change. When tension dominates, the strain and stress exhibit a sufficiently small gradient across the film's thickness that they can be approximated to be constant, and the tensions can be calculated as in Eq. 1.31.

A quantitative description of the lateral deformation (w) through bending and stretching of a film when subjected to a transvese load (p) applied to the film's surface is given by the Föppl - von Kármán (FvK) equation [49]:

$$B\Big(\frac{\partial^4 w}{\partial x^4}+2\frac{\partial^4 w}{\partial x^2\partial y^2}+\frac{\partial^4 w}{\partial y^4}\Big)-h\Big(\sigma_x\frac{\partial^2 w}{\partial x^2}+2\tau_{xy}\frac{\partial^2 w}{\partial x\partial y}+\sigma_y\frac{\partial^2 w}{\partial y^2}\Big)=p\,, \tag{1.42}$$

where $B = Eh^3/12(1-\nu^2)$ is known as the bending rigidity. The first bracketed term on the left side represents the bending contribution to the deformation, whereas the second term is associated with stretching. The FvK equation is only valid for Hookean responses of the solid and small slopes of the deformed film. In addition to Eq. 1.42, the equilibrium condition given by Eq. 1.30 must also be satisfied. It should be noted that, in general, the stresses in Eq. 1.42 depend themselves on the deformation induced in the film, as these deformations are associated with strains in the solid [49]. Needless to say, these equations are notoriously difficult to solve and are only tractable in certain limiting cases, such as when stretching dominates over bending.

When stretching dominates, tensions can be introduced into Eq. 1.42 via Eq. 1.31. To gain some insight into this regime, we imagine a deformation in the film that is independent of y (i.e. $w = w(x)$). Then, the FvK equation becomes:

$$B\frac{\partial^4 w}{\partial x^4} - T_x\frac{\partial^2 w}{\partial x^2} = p\,. \tag{1.43}$$

At the scaling level, we can describe the deformation as having some amplitude A which occurs over a typical length scale L. Using these terms, the bending contribution is of order BA/L^4 and the stretching contribution is of order T_xA/L^2. Therefore, the film is in a stretching dominated regime when $T_xA/L^2 \gg BA/L^4$. From this, we find a useful criterion for the stretching dominated regime:

$$L \gg \sqrt{\frac{B}{T}} \tag{1.44}$$

where T is the tension in the film and L is the typical length scale over which the film is deformed (or over which the load acts). Thus, if the film is prepared with a large tension before a lateral load is applied, it is likely to be in a stretching dominated regime. It is important to note that, even in this case, if the film is inspected on length scales $L \ll \sqrt{B/T}$, bending plays an important role in dictating the film's deformation. Rather, stretching is dominant when the system is inspected over length scales relevant to the large-scale ("global") deformation or load distribution. The global deformation of a film is then described by [49]:

$$T_x\frac{\partial^2 w}{\partial x^2} + 2T_{xy}\frac{\partial^2 w}{\partial x \partial y} + T_y\frac{\partial^2 w}{\partial y^2} = -p\,. \tag{1.45}$$

If x and y are the principal directions, the shear component vanishes, and the equation becomes simpler:

$$T_x \frac{\partial^2 w}{\partial x^2} + T_y \frac{\partial^2 w}{\partial y^2} = -p\,, \tag{1.46}$$

although the tensions are still themselves functions of the film's deformation. The most significant simplifcation arises in the *membrane* limit. An elastic membrane is a thin plate or film that has been subjected to large in-plane tensile forces applied to the circumference. The *pre-tension* is then sufficiently large that any additional tension created by the lateral deformation of the film under load is negligible [49]. In other words, if the film is loaded with a large biaxial tension as in Eq. 1.39, the values of T_x and T_y are constants in Eq. 1.46. If the film is prepared with an isotropic pre-tension T, the elastic membrane equation becomes:

$$T\nabla^2 w = -p\,. \tag{1.47}$$

All the work contained in this thesis deals with films that reside within the membrane limit.

Analogy between elastic membrane tension and interfacial tension

The tension in an isotropically loaded elastic membrane can in many ways be thought of as an interfacial tension. As discussed in Section 1.1.2, surface tension can be thought of as a tensile force (per unit length) parallel to the interface. In the same way, the mechanical tension of an elastic membrane is a tensile force (per unit length) parallel to the plane of the elastic film. We can also reproduce the example of the liquid membrane on the wire frame given in Section 1.1.2, but replace the liquid with an elastic membrane. If we displace the straight wire to the right, we must do work against the film's tension. In the limiting case of an elastic membrane, the pre-tension is large enough that deforming the membrane in this way will not change its tension considerably. Since the tension is constant as the straight wire is displaced, the problem remains completely analogous to the liquid membrane, and we find that the tension T can be thought of as a force per unit length as well as an energetic cost per unit area. Finally, if we inspect Eq. 1.47, and recognize that, in the limit of small slopes, $\nabla^2 w/2$ is equivalent to the mean curvature of the surface, we see that the equation becomes $2TC = -p$. In other words, in order for an elastic membrane to have a positive curvature, it must be sustained by a net pressure acting down on the membrane. This result is completely equivalent to the Laplace pressure of fluid interfaces, given by Eq. 1.6. Hence, when an elastic membrane is acted upon by a constant pressure load, it assumes a spherical (constant curvature) deformation in the loaded region. The analogy between tension in elastic membranes and interfacial tension is highlighted even further by the work contained in this thesis.

1.3.4 Elastic materials

We have discussed the response of an elastic film under load and under deformation, and have made the assumption that the solid material exhibits a Hookean (or linear) stress-strain relationship. These solid films may be composed of one of several different classes of material that respond elastically under deformation.

Crystalline materials, such as metals and ionic crystals, have their constituent atoms (or ions or molecules) arranged in a 3D lattice structure and are held together by bonds (metallic or ionic). These materials can be thought of as a lattice of balls held together by springs [5]. As such, it is understandable that crystals conform most closely to an ideal linear elastic response [51]. However, the elastic response is only sustained for very small strains ($< 1\%$) before yield [52]. The Young's modulus for these materials is on the order of 10-100 GPa.

Glassy materials are amorphous solids, and as such, have no organized lattice structure. Polymer glasses, such as polycarbonates, are widely utilized materials because of their transparency and desirable mechanical properties [5]. These materials are held together by intermolecular van der Waals bonds which allow them to deform elastically under small strains ($< 10\%$ and varies greatly depending on the polymer) [53]. At larger strains, the bonds are broken and the glass breaks or deforms plastically. The initial elastic deformation is well approximated to be linear, and the Young's modulus for these materials is on the order of 1-10 GPa [53]. Strained glassy films were used in Papers I and III.

Elastomers, such as rubber, are a special class of polymeric materials. These are polymer melts that contain crosslinks, i.e. fixed points where individual chains are bonded together, which renders the material into one connected network [5].

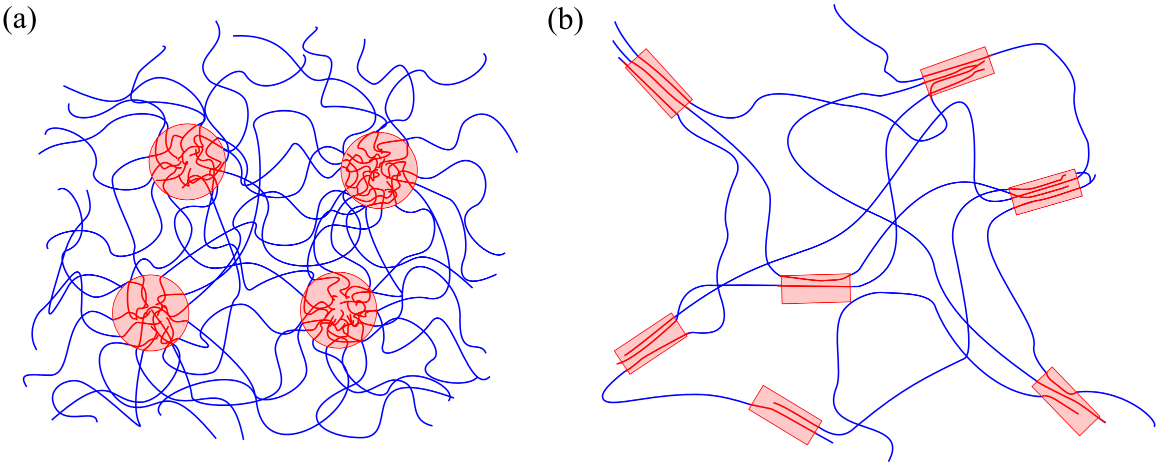

Figure 1.11: Physically crosslinked elastomers with soft (blue) and hard (red) segments. (a) A triblock copolymer, such as SIS, microphase separated into glassy spheres surrounded by a matrix of polymer chains in the melt state. (b) A multiblock copolymer, such as Elastollan, in which hard segments have aggregated to form small crystalline regions which act as physical crosslinks.

Locally (on a length scale much smaller than the distance between crosslinks), the material acts like a liquid, and as such, these materials are well approximated to be incompressible ($\nu \approx 0.5$). However, the crosslinks ensure that no macroscopic bulk flow can occur. When an elastomer is strained, the polymer chain segments in between crosslinks are forced to stretch (or compress, depending on the sign of the strain). Since ideal polymer chains in a melt are entropically favoured to have some equilibrium size [5, 29], there is a driving force which tends to restore the chains to that size. Thus, when deformed, the entire elastomer is driven to return to its natural size, and as such, is elastic. Hence, this type of elasticity is referred to as entropic elasticity. Elastomers are advantageous because they can be elastically deformed to much larger strains than glassy or crystalline materials and are also much more compliant. However, the entire elastic stress-strain relationship is not Hookean [5]. A simple statistical thermodynamics model of crosslinked polymer chains predicts a neo-Hookean relationship where the stress is linear in strain initially, but shows a substantial reduction in slope at sufficiently large strains. Thus, Hooke's law is only applicable within a range of strains which depends on the elastomer in question.

The crosslinks of an elastomer may either be chemical or physical in nature [5, 54].

In chemically crosslinked elastomers, the bonds between chains are permanent, covalent bonds. On the other hand, physically crosslinked elastomers contain crosslinks that are held together by physical bonds. In these cases, the polymers composing the elastomer contain "hard segments" and "soft segments" [54]. As an example, one commonly used physically crosslinked elastomer is composed of the triblock copolymer styrene-isoprene-styrene (SIS). The styrene segments, which are glassy at room temperature, are very short relative to the isoprene segment, which is in the melt at room temperature. SIS polymers will spontaneously microphase separate into small spherical domains of styrene in a matrix of isoprene [5, 54]. These hard glassy styrene spheres act as crosslinks for the isoprene matrix, as seen in Fig. 1.11(a). Another common elastomer is Elastollan (BASF), composed of polyurethane multiblock copolymers with small hard and long soft segments throughout [54]. The hard segments of different chains tend to aggregate and form small crystalline regions, which in turn, act as physical crosslinks for the long soft segments that are in the melt state (Fig. 1.11(b)). In either of these cases, at sufficiently high temperatures, the hard segments will also enter the melt state, and the material ceases to be elastomeric since the crosslinks have vanished. Thus, these physically crosslinked elastomers are known as "thermoplastic elastomers". SIS and Elastollan are used in all the papers in Chapter 3.

1.4 Surface energy and surface stress of solid interfaces

As described in Section 1.1, creating a liquid interface comes with an energetic cost, since molecules at the interface are stripped of roughly half their nearest neighbour interactions. Even though we typically think of surface tension as a liquid's property, solid interfaces are also associated with an energetic cost per unit area for the same reason as given for liquid interfaces. In addition, in analogy with liquids, there exists a force per unit length parallel to the interface. As an example, imagine a crystalline solid (thought of as a lattice of balls connected by springs) that is cleaved to form new interface. The atoms at the surface have been stripped of some nearest neighbour interactions, and thus they experience a net inwards force from the bonds with the atoms in the first crystal plane below the surface, leading to a contraction in these bond lengths [55–58]. In fact, this reorganization of electronic charge also causes a change in (typically a shortening of) the equilibrium bond length between the atoms at the surface. However, due to the periodic structure of a crystal, the atoms at the surface must be held in registry with the lateral structure of the crystal planes below. Thus, a force parallel to the interface exists, and is typically tensile. Unlike liquids, for solid materials, the force at the interface is referred to as the "surface stress" Υ_{AB} (for the interface between materials A and B) and is *not* necessarily equal to the surface energy. In this thesis, and traditionally in the literature, the energetic cost of forming interface (γ_{AB}) is referred to as "interfacial energy" or "interfacial tension". However, in any context where the distinction between γ and Υ is important, it is preferred to abstain from the usage of the term "interfacial tension" to eliminate ambiguity. The interfacial energy is a scalar quantity, whereas, in general, the surface stress is a tensor quantity, and may vary depending on the direction and also orientation of the surface. However, for an amorphous solid, the surface stress is expected to assume a single value for all surfaces and directions. In order to maintain a simpler discussion, and since only isotropic materials are employed in this thesis work, we will consider Υ to be independent of direction or orientation of the surface, and thus given by a single scalar quantity.

To understand the difference between γ and Υ, it is important to note that solid interface can be created in two ways: cleaving it and thus breaking the bonds at the interface, or reversibly deforming the solid to generate more interface [55–58]. The first protocol is associated with an energetic cost per unit area, γ_{AB}. On the other hand, the surface stress Υ_{AB} quantifies the force required to form new interface by elastically deforming the material. To evaluate the quantity Υ_{AB}, we imagine a semi-infinite solid, whose surface lies in the xy-plane, to be uniaxially deformed along x such that a rectangular segment of the interface with side lengths l_x and l_y elongates to length $l_x + \mathrm{d}x$ in x. If $\mathcal{F}_\mathrm{s}$ describes the free energy of the surface, the change in interfacial energy upon deformation is:

$$\Delta\mathcal{F}_\mathrm{s} = \left(\frac{\partial\mathcal{F}}{\partial A_{AB}}\right)_{l_y} \mathrm{d}A_{AB}\,, \tag{1.48}$$

where $A_{AB} = l_x l_y$ is the area of the rectangular segment of the interface between A

and B. The interfacial free energy is given by $\gamma_{AB}A_{AB}$. Thus, at constant l_y, the equation becomes

$$\Delta\mathcal{F}_{\mathrm{s}} = l_y \frac{\mathrm{d}}{\mathrm{d}l_x}\big(\gamma_{AB} l_x\big)\mathrm{d}l_x \, . \tag{1.49}$$

Of course, the change in interfacial free energy is also given by the work done against the force parallel to the interface: $\Delta\mathcal{F}_{\mathrm{s}} = \Upsilon_{AB} l_y \mathrm{d}l_x$. Thus, we have:

$$\Upsilon_{AB} = \frac{\mathrm{d}}{\mathrm{d}l_x}\big(\gamma_{AB} l_x\big) \, . \tag{1.50}$$

For fluid interfaces, γ_{AB} does not change as the interface is deformed, because molecules from the two fluids may simply rearrange themselves to maintain a constant average molecular environment at the interface. Thus, we recover $\Upsilon_{AB} = \gamma_{AB}$ for fluid interfaces, as expected. However, solid molecules do not have the ability to freely rearrange during material strain. Rather, as the material is strained, bonds at the interface are stretched and the surface atomic density is altered. Thus, it is generally expected that the energy of solid-vapour or solid-liquid interfaces changes as the material is deformed. With this concept in mind, Eq. 1.50 becomes:

$$\Upsilon_{AB} = \gamma_{AB} + l_x \frac{\mathrm{d}\gamma_{AB}}{\mathrm{d}l_x} \, . \tag{1.51}$$

Recognizing that the strain $\mathrm{d}\epsilon$ is given by $\mathrm{d}\epsilon = \mathrm{d}l_x/l_x$, we arrive at a simplified version of the Shuttleworth equation [59]:

$$\Upsilon_{AB}(\epsilon) = \gamma_{AB}(\epsilon) + \frac{\mathrm{d}\gamma_{AB}}{\mathrm{d}\epsilon} \, . \tag{1.52}$$

Therefore, when the interfacial energy is strain dependent, the force per unit length parallel to the interface is not equal to the energetic cost per unit area of the interface. Since solids have a force parallel to the interface, it implies that across a curved solid interface, there exists a Laplace pressure jump $\Delta P_{\mathrm{L}} = 2\Upsilon_{AB}C$, where C is the curvature of the surface [55].

For crystalline materials (ionic and metallic), the Shuttleworth effect (i.e. that $\gamma_{AB} = \gamma_{AB}(\epsilon)$, and hence $\Upsilon_{AB} \neq \gamma_{AB}$) is well established [55–58]. Given the regular lattice structure of these materials, rigorous theoretical calculations of surface energy and stress are tractable and have been carried out for a multitude of these materials that have simple constituents [55–60]. On the other hand, direct measurements of surface stress are scarce, as their effects are often masked by the elastic stresses which tend to be much larger in comparison [56]. Surface stress difference measurements can be performed using a thin cantilever or film [55, 56, 61–63]. In these measurements, the flexible object is made of one crystalline material and is prepared to be flat. Then, an adsorbate or oxide is grown on one side of the object, and the difference in surface stress between the two faces induces a bending of the object. The only studies which have succeeded in measuring the absolute value of the surface stress in these materials have done so by probing the change in lattice size [56, 60, 64–67]. For sufficiently small crystals (typically nanometers in size), the solid's Laplace pressure will generate measurable elastic deformations, and the change in lattice constants can be related to the surface stress. Measurements of surface energy of crystalline solids are also difficult, and typically rely on indirect methodologies that depend on theoretical models, such as studying crack propagation, healing of scratches, or even extrapolation from the surface energy in the molten state [68–70]. Unfortunately, the distinction between surface stress and surface energy in these studies is often blurred and sometimes even forgotten.

In fact, measurements of interfacial energies (γ_{sv} or γ_{sl}) of solids in general are notoriously difficult, even for amorphous materials such as glasses and elastomers [6]. For polymeric glasses, the surface energy is typically measured by extrapolation from the melt state [71–73]. Since these materials are amorphous in the solid state, and the glass transition is a kinetic transition [5], this method is thought to be fairly accurate. On the other hand, there have been no attempts (prior to Paper III) to determine the surface stresses of polymeric glasses. Elastomers have the advantage of being compliant (relative to polymer glasses or crystalline solids). Thus, measurements of γ_{sv} and γ_{sl} have been achieved by measuring the contact patch during adhesion between two elastomers [74, 75]. Although, generally the surface energy is expected to be close to that of the uncrosslinked melt. Surface stress measurements of elastomers have been carried out by deforming these materials in various geometries and incorporating surface stresses into theoretical models to interpret the solid's response [76–87]. Many of these experiments exploit "elastocapillary" phenomena, in which the surface tension of a contacting liquid (or surface stress of the solid itself) induces significant elastic deformations of the solid structure. However, there is currently significant debate whether or not surface stress and surface energy are distinct quantities for elastomers, as studies have reached conclusions both for and against [76–86, 88]. The disparity in the literature is likely rooted in the fact that interpretations of the data to determine Υ depend heavily on the model used to analyze them. In Paper III, we provide strong evidence for the absence of a Shuttleworth effect in elastomers and discuss why this result is not surprising given the nature of these materials.

1.5 Elastocapillarity

Elastocapillarity is the study of capillary induced deformations of solid structures. Although it is a marriage of two well-studied fields (elasticity and capillarity), it has been the subject of intense research activity over the last two decades. There are two chief classes of elastocapillary phenomena: deformations of a solid induced by its own surface stress and deformations of a solid induced by the capillarity of a contacting liquid. Examples of the former were given in the previous section, which described the bending of a cantilever due to differences in surface stress or the change in lattice parameters of a nanometric crystal. If we assume a spherical crystallite of radius R and an isotropic, constant surface stress Υ_{sv} for simplicity, the Laplace pressure is given by $P_{\mathrm{L}} = 2\Upsilon_{\mathrm{sv}}/R$. The elastic stresses in the crystallite are on the order $\sigma \sim \epsilon E$, where ϵ is the typical strain and E is the Young's modulus. At equilibrium, the elastic stresses must balance the Laplace pressure, so at the level of scaling: $\Upsilon_{\mathrm{sv}}/R \sim \epsilon E$. As ϵ approaches unity, the deformations of the solid become increasingly more significant. Thus, an important length scale emerges, called the elastocapillary length:

$$L_{\mathrm{EC}} = \frac{\Upsilon_{\mathrm{sv}}}{E}\,. \tag{1.53}$$

A solid is significantly deformed by its surface stresses on length scales $\ll L_{\mathrm{EC}}$, whereas elasticity dominates on length scales $\gg L_{\mathrm{EC}}$. For crystalline materials with $E \sim$ 10-100 GPa and $\Upsilon_{\mathrm{sv}} \sim 1$ N/m, we have $L_{\mathrm{EC}} \sim$ 0.1 - 1 Å, which is why nanometric crystals were used, yet the changes in lattice constants were still small [56, 60, 64–67]. However, if a gel or soft elastomer is used, L_{EC} can be made large enough for the solid's surface stress to induce deformations on near macroscopic length scales. In one experiment, researchers fabricated rods of agar- a gel with $E \sim 100$ Pa, $\Upsilon_{\mathrm{sv}} \sim 30$ mN/m, and thus $L_{\mathrm{EC}} \sim 300$ μm. In doing so, they found that when the fiber radius is $< \frac{1}{6}L_{\mathrm{EC}}$, the fiber developes a capillary instability completely analogous to the well-known Plateau-Rayleigh Instability (PRI) [89, 90]. The instability continues until elastic forces grow large enough to balance the capillary driving force, and the elastic rod reaches an equilibrium peristaltic shape. Moreover, soft structures of size larger than L_{EC} have been shown to spontaneously deform in an attempt to decrease surface area, such as rounding of any sharp corners and flattening of surface undulations [91–93].

The other class of elastocapillary phenomena concerns the deformation of solid structures driven by the surface tension forces of a contacting liquid. These interactions can lead to stunning displays of self-assembly and pattern formation. For instance, when a droplet is put into contact with a thin flexible sheet, if the solid sheet is sufficiently compliant, it will spontaneously wrap itself around the droplet [94–98]. This effect can be exploited to assemble the solid sheet into desired 3D configurations in a process dubbed "capillary origami" [1,94,99]. Elastocapillary mechanics are also prominent when surface tension forces act on thin solid fibers, as such structures are highly compliant too [1]. These interactions result in diverse phenomena such as the bundling of carbon nanotubes and nanowires during processing [3,4,100–102], coalescence of wet hair [103,104], and spontaneous coiling of fibers within as well as on the surface of a droplet (studied in Paper AII) [1,105–107]. In most of the examples listed above, the deformation of the solid is set by an equilibrium between surface tension forces of the liquid, which drive deformation, and elastic bending of the structure, which resists deformation. When these forces are compared, a natural length scale emerges called the bending-elastocapillary length, L_{BC} [1]:

$$L_{\mathrm{BC}} = \sqrt{\frac{B}{\gamma}}\,, \tag{1.54}$$

where B is the bending rigidity. If capillary forces act over length scales $\ll L_{\mathrm{BC}}$, the bending rigidity of the structure dominates, and it does not significantly deform. On the other hand, if surface tension forces act over length scales $\gg L_{\mathrm{BC}}$, capillarity dominates, and the structure readily deforms. This condition is reminiscent of

Eq. 1.44, which compares mechanical tension to bending rigidity.

However, a solid material can deform through other modes than just bending. For instance, a thin elastic film is highly compliant and may deform primarily by stretching. Moreover, a solid that has a low modulus is compliant even through bulk deformation. In the next two subsections, we will explore elastocapillary interactions when a droplet partially wets such substrates.

1.5.1 Partial wetting on a soft solid

When a droplet partially wets a soft solid, it exerts a contact line force through its surface tension which tugs on the substrate, and also exerts Laplace pressure onto the substrate over the entire wetting region. The balance between the capillarity of a liquid and the bulk elasticity of a solid is described by an elastocapillary length $L_{\text{EC}} = \gamma/E$ [1, 83]. This length scale is slightly modified from Eq. 1.53, because it is the surface tension of the liquid that drives the deformation in this case. Thus, when a droplet is sessile on a solid, the surface tension force at the contact line tugs at the solid to deform it into a wetting ridge on a length scale comparable to $L_{\text{EC}} = \gamma/E$, as seen in Fig. 1.12 [108–111]. For hard substrates, such as crystalline materials and glasses, $L_{\text{EC}} \sim 10^{-12}$ m and, since this is much smaller than atomic size, no wetting ridge forms. Thus, the picture drawn in Fig. 1.4 is completely valid for hard substrates. However, the wetting ridge can be seen in elastomeric substrates where $L_{\text{EC}} \sim 10 - 100$ nm, and is quite prominent for soft gels where L_{EC} may reach several hundred microns. How is then the Young-Dupré law of partial wetting modified when the substrate is deformable?

When the droplet radius r is much larger than L_{EC}, the deformation of the substrate is a small perturbation to the overall wetting between the solid and the substrate. This is the case drawn in Fig. 1.12, where the solid remains undeformed over the majority of the wetting region. As such, the free energy minimization presented in Section 1.2.1 for rigid substrates remains valid, becase the additional elastic and interfacial energy from the wetting ridge can be neglected. Therefore, Young-Dupré's law (Eq. 1.16) holds for the global contact angle subtended to the undeformed substrate (defined in Fig. 1.12 as θ_{Y}) when $r \gg L_{\text{EC}}$. On the other hand, the angles subtended between the three different interfaces in a local picture of the contact line

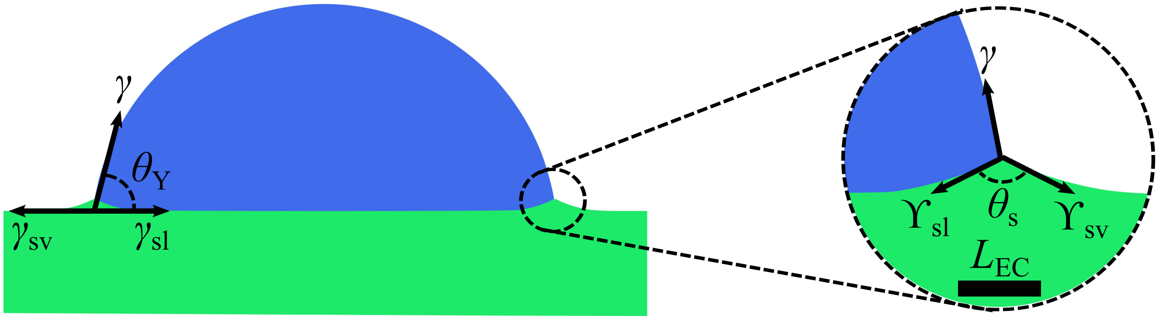

Figure 1.12: Partial wetting on a soft solid substrate. The global contact angle $\theta_{\rm Y}$ is set by Young-Dupré's law (left), but locally the solid is deformed into a wetting ridge (right zoom-in), in which the solid angle $\theta_{\rm s} < 180°$. The concept of a Neumann construction balance between γ, $\Upsilon_{\rm sl}$, and $\Upsilon_{\rm sv}$ to determine the wetting ridge geometry is currently debated.

(zoom-in of Fig. 1.12) are believed to be set by a Neumann construction in which the liquid surface tension γ is balanced by the solid surface stresses of the two solid interfaces $\Upsilon_{\rm sv}$ and $\Upsilon_{\rm sl}$ [78, 80, 83, 85, 86, 111–116].

In the regime of small droplets or vanishing Young's modulus, $r \ll L_{\rm EC}$, capillarity dominates over elasticity. In this case, the solid behaves as a liquid substrate, and the wetting resembles the picture drawn in Fig. 1.5. In this regime, the global contact angles between the three interfaces (analogous to α_1, α_2, α_3 in Fig. 1.5) are determined by a Neumann construction between γ, $\Upsilon_{\rm sv}$, and $\Upsilon_{\rm sl}$. Thus, as the modulus of the substrate or the droplet size is varied, there is a continuous transition from partial wetting on a rigid substrate (Young-Dupré's law) to partial wetting on a liquid substrate (Neumann's law) [78, 83, 113, 115].

The concept that the local contact line geometry (as depicted in Fig. 1.12) is set by a Neumann construction allows the surface stresses of the two solid interfaces to be determined. Since γ is known, if the angles between the three interfaces are measured at the contact line, $\Upsilon_{\rm sv}$ and $\Upsilon_{\rm sl}$ can be computed. Experiments using this methodology (or a simple variant thereof) have been carried out by using either confocal microscopy or X-ray microscopy to image the wetting ridge of polydimethylsiloxane (PDMS) gel with various liquids ($L_{\rm EC} \sim 10$ μm) in a regime where $r > L_{\rm EC}$ [78, 80]. These studies found values in the range of 30-60 mN/m for $\Upsilon_{\rm sv}$, larger than $\gamma_{\rm sv}$ of PDMS ($\sim$ 21 mN/m) [78, 80]. In later experiments, the PDMS substrates were pre-strained before the measurement [85, 86]. In addition, the local elastic strain induced by formation of the wetting ridge itself was measured using fluorescently labeled particles. Thus, the researchers measured surface stresses as a function of the total strain ϵ. For simplicity, they employed a liquid wherein $\theta_{\mathrm{Y}} \approx 90^{\circ}$ and the wetting ridge was observed to be symmetric, so the approximation that $\Upsilon_{\mathrm{sv}} \approx \Upsilon_{\mathrm{sl}} \equiv \Upsilon$ was made. In doing so, they found Υ to increase linearly with strain (due to an observed increase in θ_{s} in Fig. 1.12), with an extropolated value of $\sim$ 22 mN/m at $\epsilon = 0$, up to a value of $\sim$ 50 mN/m at $\epsilon = 25\%$. On the other hand, there was no change in the Young's contact angle with strain, implying that $\mathrm{d}\gamma_{\mathrm{sv}}/\mathrm{d}\epsilon = \mathrm{d}\gamma_{\mathrm{sl}}/\mathrm{d}\epsilon$ for this material. Interestingly, the zero-strain value of the surface stress found from this experiment coincides with the surface energy of PDMS, i.e. there is no Shuttleworth effect present at zero strain. The equality between surface stress and surface energy for unstrained PDMS has also been found independently using other experimental methods [81,84]. However, no other studies have verified the strong strain dependence of Υ in PDMS. In fact, molecular dynamics simulations on crosslinked polymer gels found the surface energies and stresses to be identical and strain-independent for strains comparable to those used in the PDMS experiments [87]. These simulations claim that the surface stress balance at the contact line is only valid in the limit of vanishing elastic contribution, i.e. $r/L_{\mathrm{EC}} \rightarrow 0$ [115]. Otherwise, the deformation of the substrate and formation of the wetting ridge lead to a significant elastic stress which must be included in the local force balance at the contact line [87,115]. Hence, measuring surface stresses from the wetting ridge without considering elastic stresses would lead to inaccurate results, and may be the cause of the increasing value of Υ with ϵ rather than the Shuttleworth effect being at play.

Beyond being useful for metrology, partial wetting on soft solids can lead to some interesting dynamics. Recent work demonstrated that soft substrates that are prepared with a gradient in compliance lead to spontaneous motion of the droplets [117, 118]. This "durotaxis" can be exploited to generate liquid patterning on soft substrates. In addition, the elastocapillary deformations generated by droplets can be sufficiently long range to cause interactions with neighbouring droplets [119]. In fact, droplets may attract or repel depending on the compliance of the substrate.

1.5.2 Partial wetting on a compliant solid film

Other than employing extremely soft solids, elastocapillary deformations in partial wetting can also be amplified by choosing a substrate that is compliant simply due to its geometry, such as a suspended thin film. In one realization of this system, a thin glassy polystyrene sheet is floating on the surface of a water bath [120–122]. The film is held taught by the surface tension of the water bath tugging at the edge of the film and serves as a fixed tension boundary condition. When a droplet is placed on this film, capillary forces of the droplet induce a global out-of-plane deformation of the film below the droplet (despite L_{EC} being less than atomic scale). The induced deformation, and consequent additional stresses in the film, have been deduced by solving Eq. 1.42 in the limit of small bending contribution [122]. Theoretical and experimental work showed that in certain regimes, the capillary forces of the droplet lead to an azimuthal compression of the film immediately surrounding the wetting region [121, 122]. This "hoop" strain is responsible for a beautiful wrinkling pattern that emerges surrounding the droplet, extending radially outward over a length comparable to the droplet size [120].

Another highly compliant geometry is that of a free-standing film that is clamped at its sides [77, 123–125]. Nadermann *et al.* placed droplets on free-standing films of PDMS elastomer ($E \sim$ MPa) that were tens of microns thick but carried no pretension [77]. They observed that the droplet induced a significant bulge in the film below itself, comparable in magnitude to the droplet size itself. The deformation was also computed by solving Eq. 1.42 in the limit of small bending contribution. In the calculation, the deformation was assumed to generate a constant tension T_{in} in the wetted region of the film, and a constant (but different) tension T_{out} in the unwetted region.

In this system, the effects of bending remain localized to a small region surrounding the contact line, and stretching dominates in a global picture of the droplet- the length scale of which is set by Eq. 1.44. Thus, these problems are characterized by a convenient separation of length scales, depicted in Fig. 1.13 [83]. On global length scales $L \gg \sqrt{B/T}$, stretching dominates, and the capillarity of the droplet is balanced by tensile forces in the film. On intermediate length scales $L_{\mathrm{EC}} \ll L \ll \sqrt{B/T}$, bending constitutes the dominant mode of deformation of the film. Finally, on length

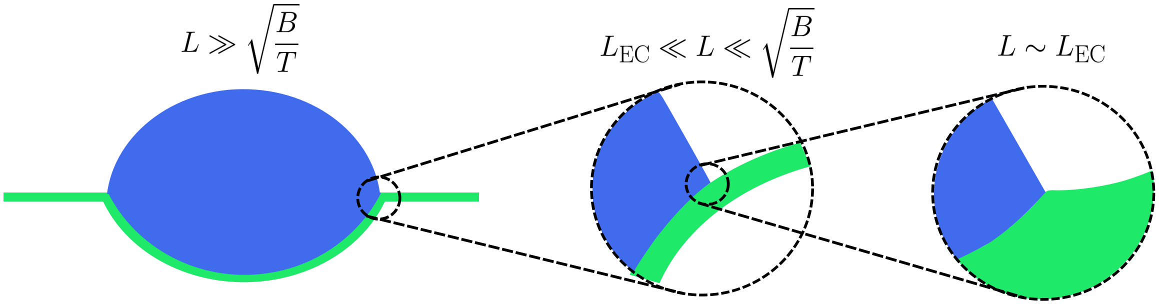

Figure 1.13: The separation of length scales which exist when a droplet partially wets a compliant free-standing film. The droplet's capillarity creates a global deformation of the film. In this deformation, stretching dominates globally (left), bending is the relevant elastic mode on intermediate length scales (middle), and bulk elastic deformation is seen on the smallest local length scales (right).

scales $L \sim L_{\mathrm{EC}}$ the solid is deformed into a wetting ridge, as discussed previously.

In the global picture, the film outside the wetted region remains planar. The Laplace pressure in the droplet (given by Eq. 1.5) is the source of the pressure term in Eq. 1.47 for the wetted region where $T = T_{\mathrm{in}}$ in this case. Since the film has a constant tension in this region, the curvature of the film must be constant to sustain a constant pressure load. Therefore, the bulge is a spherical cap on global length scales. It should be noted that the change in Gaussian curvature from a flat film to a spherical cap generally requires non-uniform additional stretching of the material. However, in the context of the membrane limit, these additional strains are negligible when compared to the pre-existing strain in the film, and thus, do not significantly modify the film's tension. Thus, by measuring the global radius of curvature of the bulge R_{b}, and comparing it to the Laplace pressure of the droplet, the tension in the wetted region of the film can be measured using the equation:

$$\frac{T_{\mathrm{in}}}{\gamma} = \frac{R_{\mathrm{d}}}{R_{\mathrm{b}}} \tag{1.55}$$

where R_{d} is the droplet's radius of curvature [77]. This result is completely analogous to Eq. 1.19. Nadermann *et al.* measured tensions on the order of ~ 0.1 N/m using this procedure, validating the separation of length scales ($L_{\mathrm{EC}} \sim 50$ nm $\ll \sqrt{B/T} \sim 50$ μm $\ll \sim 500$ μm - the size of the droplet, which sets the global scale).

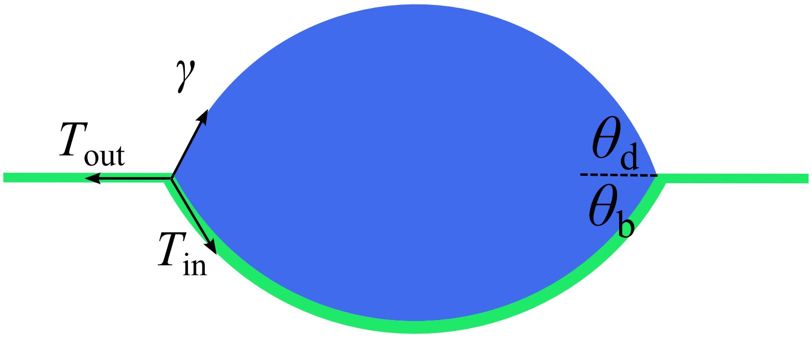

Figure 1.14: A global picture of the partial wetting of a droplet on a compliant free-standing film. The film is planar surrounding the droplet, and assumes the shape of a spherical cap in the wetted region. The contact line geometry is set by a Neumann construction that balances mechanical as well as interfacial tensions.

As seen in Fig. 1.14, the global contact line geometry is thus defined by two contact angles, θ_{b}- the angle subtended between the bulge and the unwetted film and θ_{d}- the angle subtended between the droplet-air interface and the unwetted film. Since the film is in mechanical equilibrium, it implies that the forces acting on the film at the point of the contact line must balance [77, 124, 125]. This equilibrium implies that a Neumann construction, as shown in Fig. 1.14, must be implemented at the contact line which balances T_{in}, T_{out}, and γ. In fact, performing this balance in the vertical direction yields the following relation:

$$\frac{T_{\text{in}}}{\gamma} = \frac{\sin\theta_{\text{d}}}{\sin\theta_{\text{b}}}\,. \tag{1.56}$$

Given the spherical cap identity $r = R\sin\theta$ where r is the contact radius, Eq. 1.55 and Eq. 1.56 are completely equivalent. Nadermann *et al.* used the horizontal force balance to determine T_{out}, although erroneously assumed that the internal angle of the liquid (i.e. $\theta_{\text{d}} + \theta_{\text{b}}$) was identical to Young's angle. In fact, Young-Dupré's law should be recovered when a liquid contact line meets a rigid substrate, and does not apply to the global picture here where the solid is cuspy at the contact line.

A further simplification arises when the film enters the membrane limit where the pre-tension is sufficiently large that the deformations imposed by the droplet do not significantly alter the tension [123]. The Neumann construction depicted in Fig. 1.14 remains unchanged, except for the modification that the mechanical tension in the film is identical in the wetted and unwetted regions. Thus, the partial wetting between elastic membrane and liquid is completely analogous to partial wetting of a droplet on a liquid substrate (Section 1.2.2), but with the interfacial tensions between the two liquids replaced with T_{in} and T_{out}. These total tensions (T_{in}, T_{out}) are a sum of the constant mechanical tension of the film T and interfacial tensions between film and vapour as well as film and liquid. Thus, we have:

$$T_{\mathrm{in}} = T + \gamma_{\mathrm{sl}} + \gamma_{\mathrm{sv}} \tag{1.57a}$$

$$T_{\mathrm{out}} = T + 2\gamma_{\mathrm{sv}} \, , \tag{1.57b}$$

which means there is a simple relationship between T_{in} and T_{out}:

$$T_{\mathrm{out}} = T_{\mathrm{in}} + \gamma_{\mathrm{sv}} - \gamma_{\mathrm{sl}} = T_{\mathrm{in}} + \gamma \cos\theta_{\mathrm{Y}} \, , \tag{1.58}$$

where we have made use of Young-Dupré's law. It is important to note that $\theta_{\mathrm{Y}} \neq \theta_{\mathrm{d}} + \theta_b$, but rather is the contact angle of the liquid on a supported (rigid) substrate of the elastic film. The above concepts, discussing the partial wetting between a liquid droplet atop an elastic membrane, serve as the basis for the work done in Papers I and II.

1.5.3 Elastocapillary interactions in dewetting

In order for a car to brake on a wet road, it is imperative that the rubber tires make direct contact with the asphalt. The pressure due to the car's weight causes the liquid film to drain until a dry patch is nucleated. At this point, dewetting is the process responsible for evacuating the remaining liquid, and ensuring that dry contact between the rubber tires and asphalt is established [6]. This example represents one of several motivations for studying elastocapillary interactions in dewetting. As we know from previous discussions, on length scales comparable to L_{EC}, the dewetting liquid will induce bulk deformations of the solid. In the case of the dewetting of a liquid film pressed between a rigid substrate and a bulk elastomer, these elastocapillary interactions determine the shape of the dewetting rim [6, 126]. Theoretical and experimental work on such systems showed that the dewetting velocity of holes is no longer constant in time as it is on a rigid substrate, but rather scales as $t^{-1/4}$, where t is time [126, 127]. The modified scaling arises in spite of the driving force to dewet deriving purely from interfacial energy changes as before and the dissipation in the system once again coming from viscous dissipation in the dewetting liquid rim. Other studies have investigated dewetting of a liquid film atop a soft semi-infinite substrate, although most have focused on spinodal dewetting [128–131]. In fact, one of these studies demonstrated that uniaxially stretching the elastomeric substrates can generate anisotropic spinodal dewetting morphologies [131]. Since dewetting receives significant attention for micropatterning purposes, this result demonstrates that morphology could potentially be tuned not just by pre-designing chemical and topographical patterns in the substrate, but also using elasticity. Another study examined dewetting by hole growth on soft substrates, and found that the formation of the wetting ridge at the moving contact line leads to viscoelastic dissipation within the elastomer which may actually dominate over viscous dissipation in the liquid, further retarding the dewetting process [128]. Rather than studying the dewetting between a rigid substrate and a soft semi-infinite elastomer, it is also interesting to replace the bulk elastomer with a thin, compliant elastic layer [129, 132–134]. In one set of experiments, the retraction of thin water films sandwiched between two flexible sheets of mica was observed [132, 133]. Although the influence of stiffness of the mica was not studied in detail, it was noted that thicker, less compliant sheets resulted in slower dewetting. In Paper IV, we study the dewetting of a liquid film capped by an elastic membrane with variable pre-tension.

Chapter 2

Experimental details

In the following section, I will summarize methods relevant to the experiments and subsequent data analysis of the papers in Chapter 3. Although the methods are described in each manuscript, this section should serve as a supplement for those who require further detail. In the following section, I will describe the materials and procedure for making thin polymer films (Section 2.1), several methods of introducing tension into these films (Section 2.2), how droplets are deposited onto the substrates (Section 2.3), and measurements of contact angle (Section 2.4).

2.1 Creating thin polymer films

2.1.1 Materials

In the experimental protocols for the papers in Chapter 3, a variety of polymers were used to make films. Elastomers were used in every experiment. Two physically crosslinked elastomers were chiefly used: Styrene-isoprene-styrene (SIS) triblock copolymer (Sigma-Aldrich) with a 14% styrene content and Elastollan TPU 1185A (BASF). Solutions of SIS were made by dissolving in toluene (Fisher Scientific, Optima grade) at mass concentrations c ranging from 4% to 20%. Elastollan was dissolved in cyclohexanone (Sigma-Aldrich, puriss p.a. >99.5%) with c ranging from 2% to 7%. In Paper III, polyvinyl siloxane (PVS), a chemically crosslinked elastomer, was also employed, and made by mixing base and catalyst (RTV EC00 Translucid) at a 1:1 ratio. In Papers I and III, polymers that are glasses at room temperature were used. In Paper I, we made films of poly(n-butyl) methacrylate (PnBMA) with number averaged molecular weight $M_n = 66$ kg/mol and polydispersity index PI = 1.05 (Polymer Source Inc.). This polymer was dissolved in toluene at c of 1% and 2%. This polymer was used because it has a low glass transition temperature ($T_\mathrm{g} \sim 30$°C), which permitted lower pre-tensions to be introduced in free-standing films of these materials (see Section 2.2.1). In Paper III, we used polysulfone (PSf) with $M_n = 22$ kg/mol (Sigma-Aldrich) and poly(bisphenol-A) carbonate (PC) with $M_n = 22$ kg/mol and PI = 1.9 (Polymer Source Inc.). PSf and PC were dissolved in cyclohexanone and chloroform (Fischer Scientific, Optima grade) respectively at concentrations of 7% and 5%. These materials were chosen for Paper III because they have large elongations at yield (6% and 8% respectively for bulk samples) [135]. Finally, in Paper IV, polystyrene (PS) with $M_n = 15.8$ kg/mol and PI = 1.05 (Scientific Polymer Products) was used. PS solutions were made by dissolving in toluene at $c = 3\%$. This polymer was used because it readily dewets in the experimental geometry of Paper IV and because it is a standard polymer choice for dewetting studies.

In addition, primarily two materials were used as substrates. Silicon wafers (University Wafer) were cleaved into 1 cm x 1 cm pieces to serve as a supporting rigid substrate for polymer films. Freshly cleaved 3 cm x 3 cm mica substrates (Ted Pella Inc.) were used solely as an intermediary for films that were to be strained or made free-standing, as will be described in more detail in the following section. Silicon and mica are ideal substrates because they are extremely smooth and clean when freshly cleaved.

2.1.2 Film preparation

Uniform polymer films were made by spincoating with a commercial spincoater (Headway Research Inc., Model PWM32). In this process, a few drops of polymer solution are placed on a substrate (be it silicon or mica) which is then rotated at high rates (2000-5000 rpm). When the sample is rotated initially, most of the solution is ejected, leaving behind a layer of solution on the substrate. As the rotation proceeds, the solution continues to flow outwards, causing the layer of solution to thin over time and become highly uniform. This stage occurs very quickly, and the solution does not evaporate coniderably during this period. After some time, the evaporation of the solvent from the solution becomes significant. During this stage, the polymer solution increases in concentration, and hence, becomes significantly more viscous, and thinning of the film occurs mainly due to evaporation rather than outwards flow. In the case of polymers that are glassy at room temperature, the concentration eventually becomes sufficiently high that the polymer chains lose mobility and the film vitrifies. For the physically crosslinked elastomers, the polymers assemble into hard and soft regions during spinning, and are elastomeric at the end of the process. The entire spinning process is typically set to 20 s for solutions with toluene and chloroform as solvents. However, cyclohexanone is much less volatile, and the spinning is programmed to continue for 100 s to ensure most of the solvent has evaporated. In order to vary the final film thickness, there are two adjustable parameters: film thickness increases with concentration and decreases with spin speed. The final film thickness can then be measured using various techniques. In this thesis work, we used ellipsometry (Accurion, EP3). In the experiments for the papers in Chapter 3, films were made with thicknesses ranging from 65 nm to 3 μm. Spincoating is an excellent method for creating highly uniform, thin polymer films. For films less than 1 μm thick, the thickness variation is typically less than 5%. For thicker films, we observe thickness variations on the order of 10%. Once cast, all films were annealed for 10 minutes on a hot-stage (Linkam) to remove residual solvent and relax the polymer chains. Glassy films were annealed tens of degrees above T_{g}, whereas elastomeric films were annealed at elevated temperatures but where the material remains physically crosslinked.

As mentioned previously, polymer films that were intended to be strained or made free-standing were first prepared on mica as an intermediary substrate. Mica is advantageous because it has a high affinity for water, which means that films are easily delaminated from the substrate by dipping the sample into a water bath. To remove films from the substrate, the films on mica are first scored into rectangular sections. The scoring is done using a scalpel for glassy films or Elastollan films of thickness $\gtrsim$ 400 nm. For SIS and thin Elastollan films, scoring is achieved by wetting a cotton swab with acetone and tracing out the perimeter of a rectangle on the mica, which removes the elastomer from the traced path. The mica sheet is then dipped into an ultra-pure water bath (18.2 MΩ·cm, Pall, Cascada, LS). In doing so, a thin film of water wedges itself between the polymer film and the mica substrate. This method can be used to fully release the polymer film from the mica, which leaves it floating on the surface of the bath. The film is then picked up using a different substrate, such as those described in Section 2.2.1 or Section 2.2.2. Alternatively, the mica can be removed from the water bath before the film has been released. In this way, a thin water film exists between the polymer film and the mica. The polymer film can then be brought into adhesive contact with another substrate, allowing the mica to be removed easily, thus completing the transfer of the polymer film. This protocol was used to transfer elastomeric films onto the straining apparatus described in Section 2.2.3.

2.2 Creating tension in solid films

Every project included in this dissertation has employed taut polymer films. In the process, we discovered that applying a well controlled pre-tension to such thin films is not trivial. Therefore, increasingly more sophisticated techniques were employed over the course of this PhD. In this section, the various methods will be described in detail, beginning from the least controlled and finishing with the most tunable.

2.2.1 Method 1: isotropic tension set by film thickness

In the first technique, the polymer film is floated onto the surface of the ultra-pure water bath. A stainless steel washer with a circular hole is dipped into the water bath, positioned underneath the floating film, and then picked up along with the film. In doing so, the solid film is suspended over the hole as shown in Fig. 2.1. The strong adhesion between the film and the washer ensures that the film is clamped around the perimeter of the hole. Any residual water is then left to dry.

When the film is composed of an elastomeric material, it is found to be taut with an isotropic tension as prepared (verified and measured in Paper I). In addition, the tension is varied by creating samples with different elastic film thicknesses. Although this is an excellent technique for simply introducing an isotropic pre-tension, the mechanism by which the tension is generated is not understood. As mentioned in Section 1.5.2, when a film is floating on the surface of water, it experiences a constant

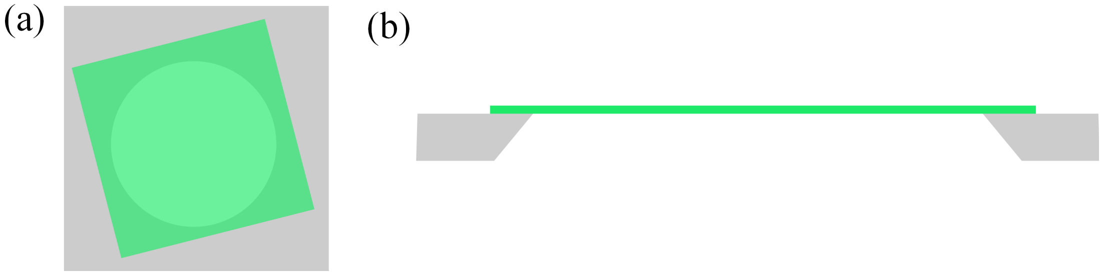

Figure 2.1: Schematic of the simplest method for making films with isotropic tension. (a) Top view and (b) side view perspective of the washer with a free-standing film suspended over its circular hole.

isotropic tension given by the surface tension of water. Since the elastic films in our experiments are picked up directly from the water surface, this effect is responsible for a constant minimum value of the film's tension, but does not explain why it increases with film thickness. Our current hypothesis is that the water bath causes a minute swelling of the elastic film. After floating, when the sample is left to dry, the water escapes the elastic film causing it to contract. However, since it is clamped at its boundaries, it is restricted from doing so, and thus becomes loaded with a constant strain which leads to a tension proportional to film thickness (Eq. 1.41). We have deduced that the strain needed to explain the measured tensions is minute, on the order of 1-2%.

When the film is glassy, the film is not taut and quite wrinkled as prepared. To introduce tension, the sample is first heated above the glass transition. In this state, the film is liquid and rapidly flows to eliminate wrinkles and become perfectly planar. Next, the film is quenched to room temperature, and thus returned to the glassy state. As the film and washer are cooled, they contract. However, the thermal expansion coefficient is much larger for polymeric materials compared with stainless steel. As a result, the glassy film is driven to contract more than the washer, but it is restricted from doing so because it is clamped at its edges. Therefore, a constant strain proportional to the difference between the two thermal expansion coefficients is introduced into the sample, and the tension can be calculated from this strain using Eq. 1.41, as was done in Paper AIII. Thus, for glassy films, the tension may also be varied by changing the film thickness. In addition, the strain resulting from

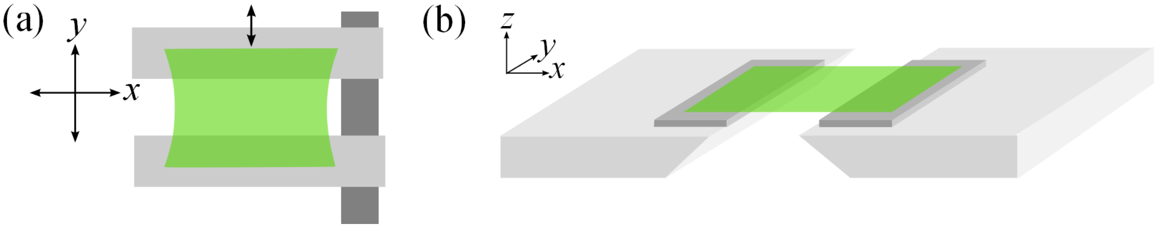

Figure 2.2: (a) Uniaxial stretcher in which the film is strained by hand by translating the top support in the direction indicated by the arrow. (b) Straining apparatus used to generate highly precise uniaxial strains. One of the aluminum blocks is held fixed while the other is translated using a motorized translation stage.

thermal contraction depends on the difference between T_{g} and room temperature. Since PnBMA has a low T_{g}, it was used in Paper I to create tensions comparable to those obtained in the elastic films.

These methods for creating isotropic tension by varying film thickness were employed in Paper I, and the tension in the film was measured using Eq. 1.56. In later work, other techniques were used that permitted greater control of the magnitude and anisotropy of the tension.

2.2.2 Method 2: biaxial tension from tunable uniaxial strain

In order to create films with biaxial tension, a different technique must be used. An elastic film is instead picked up off the water surface by a uniaxial stretcher shown in Fig. 2.2(a). The film is suspended (clamped by adhesion) between two silicon wafer supports, but its boundaries are free in the orthogonal planar direction. Therefore, the free boundaries acquire a bowed configuration, as depicted. For reasons described in the previous section, the film is already taut when prepared. However, an additional biaxial tension can be introduced by uniaxially stretching the film by translating the top support, seen in Fig. 2.2(a), by hand along the y-direction. Through this protocol, the film acquires a high tension along the y-direction. However, the film is not able to freely contract in response along the x-direction because it is pinned to the supports at the extremities of the free boundary. Therefore, straining the film along the y-direction also introduces a small tension in the x-direction. Although the tension field must vary significantly near the boundaries (we know from Section 1.3.2

that the tension normal to a free boundary must be identically 0), it is expected to be fairly uniform near the center. As such, close to the center of the film, there is a uniform biaxial tension with $T_y > T_x$. This method was used in Paper II to study the partial wetting of droplets on films with biaxial tension. Since the applied strains are not well controlled in this method, the tensions were determined *a posteriori* using a Neumann construction akin to the one depicted in Fig 1.14.

If highly precise uniaxial strains are required, a different system should be used. Depicted in Fig. 2.2(b), the straining apparatus consists of two aluminum blocks that are separated by a gap. Attached to the surface of these aluminum blocks are two silicon wafers. The film is picked up off the water surface to be suspended across the gap between the blocks, as shown in the figure. Silicon wafers are used because their smoothness ensures that good adhesive contact exists with the polymer film, which prevents delamination during strain. To prepare for straining, one of the blocks is held in place while the other is attached to a motorized translation stage (Newport MFA-CC, SMC100CC). One block is then translated by a pre-determined amount which increases the gap spacing, and the film is thus stretched along the x-axis. Although the strain in the x-direction is known precisely, the strain in the y-direction is once again not known. This methodology was employed in Paper III because the uniaxial strain was the control parameter in that case, and glassy films were used which had to be precisely strained in the range of 0-8%. In order to further increase adhesion of these films with the sample holder to prevent delamination, the silicon wafers were coated in advance with the same polymer as was to be strained. Elastomeric films were also strained uniaxially up to 100% using this apparatus. In this study, the objective was to create strained films supported on rigid substrates. Therefore, once the films were strained, the sample holder depicted in Fig. 2.2(b) was turned upside down and carefully brought down until the stretched film formed contact with a silicon wafer that was placed below. The strong adhesion between film and wafer ensured that the film could not relax the applied strain. At this point, a scalpel was used to cut the edges of the film in order to release it from the sample holder.

Although the latter apparatus is capable of applying precise strains, the first stretcher (Fig. 2.2(a)) is much smaller and is able to fit under the microscope for a contact angle measurement (refer to Section 2.4). For this reason, and since precise strains were not needed, the first uniaxial straining apparatus was used for Paper II.

2.2.3 Method 3: biaxial or isotropic tension from tunable biaxial strain

The final technique that will be discussed allows for complete biaxial control of the strain in an elastic film. The straining apparatus is depicted in Fig. 2.3(a). It is composed of a 200 μm Elastosil (Wacker Chemie) elastic sheet which has been cut into a rounded plus shape. In addition, the sheet is prepared with a circular hole at its center. Each of the four edges of the plus shape is held by a clamp which is attached to a post that is capable of being translated in the directions indicated in Fig. 2.3(a).

To use this straining set-up, the mica is retracted from the water bath before the thin elastomeric film has been released, such that a thin water film is wedged between the polymer film and the mica. The mica sheet is then placed, film-side down, atop the hole in the Elastosil sheet. The elastomeric film forms a strong adhesive contact with the Elastosil surrounding the hole, which allows the mica sheet to be removed. In the end, a thin elastomeric film is left free-standing over the hole in the Elastosil.

The elastomeric film can now be strained by translating the posts holding the clamps. When the posts are translated, the hole in the Elastosil, and hence, the free-standing elastomeric film suspended across it, stretches or compresses (depending on the direction of translation). In this way, the strain in the film can be tuned along both x- and y-axes. The first step in the straining protocol is to relieve the pre-existing tension in the elastomeric film from preparation. This is accomplished by translating all four posts inwards to compress the film until wrinkles appear. At this precise point, the film is at its natural size, which serves as the initial condition. Thereafter, the four posts may be translated outward by a desired amount to stretch the elastomeric film and induce the desired strain. For instance, if an isotropic tension is desired, the four posts are translated outward by an equal amount Fig. 2.3(b). This increases the diameter of the suspended elastomeric film from d_i to d_f, creating a uniform isotropic strain of $\epsilon = (d_f - d_i)/d_i$. If the strain is small enough that the elastomer can be treated as Hookean, Eq. 1.41 can be used to calculate the tension. If a biaxial strain is desired, the posts translating along the y-axis are moved a different amount than

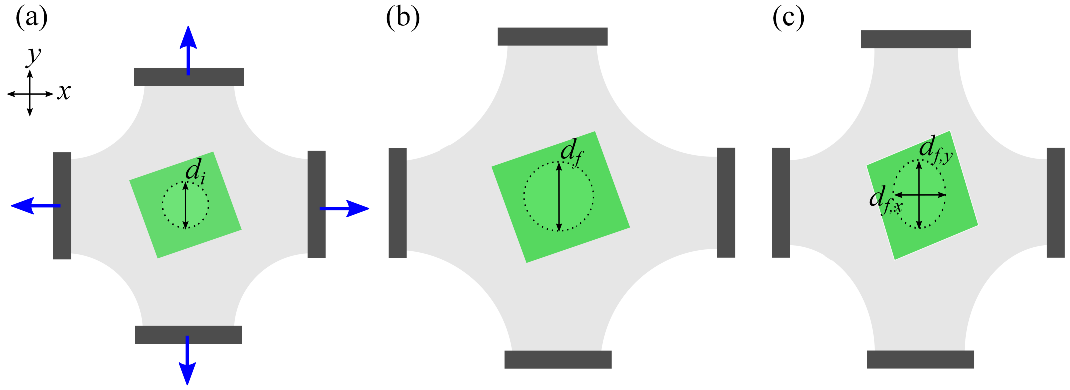

Figure 2.3: Top view of the straining apparatus used to apply tunable biaxial strains to an elastic film. (a) The initial condition of the film after the pre-existing tension is removed. The four supports may be translated in the directions indicated by the arrows to stretch the thin film. (b) All four supports displaced an equal amount to create an isotropic tension. (c) The elastic film is stretched more along the y-axis compared to the x-axis, to create a biaxial tension with $T_y > T_x$.

the two translating along the x-axis. These actions stretch the suspended film into an elliptical shape, with major axes $d_{f,x}$ and $d_{f,y}$, as seen in Fig. 2.3(c). Therefore, a uniform biaxial strain is introduced into the film with components $\epsilon_x = (d_{f,x} - d_i)/d_i$ and $\epsilon_y = (d_{f,y} - d_i)/d_i$. Once again, if the strain is small enough to be in the Hookean regime of the elastomer, Eq. 1.39 can be used to compute the tensions along the two axes. Thus, using this technique, tension can be modulated using the applied strain as well as with the thickness of the elastomer.

This method was used to create isotropic and biaxial tensions in Papers IV and V. In these projects, the stretched film served as a capping elastic membrane for dewetting (Paper IV) and partial wetting (Paper V). Once stretched, the elastic film was transferred onto a substrate. For the dewetting project, the substrate was a silicon wafer coated with a thin PS film. For the partial wetting project, the substrate was comprised of a silicon wafer coated with an elastomeric film with liquid droplets deposited atop. In either case, the substrate was placed on a stage situated directly

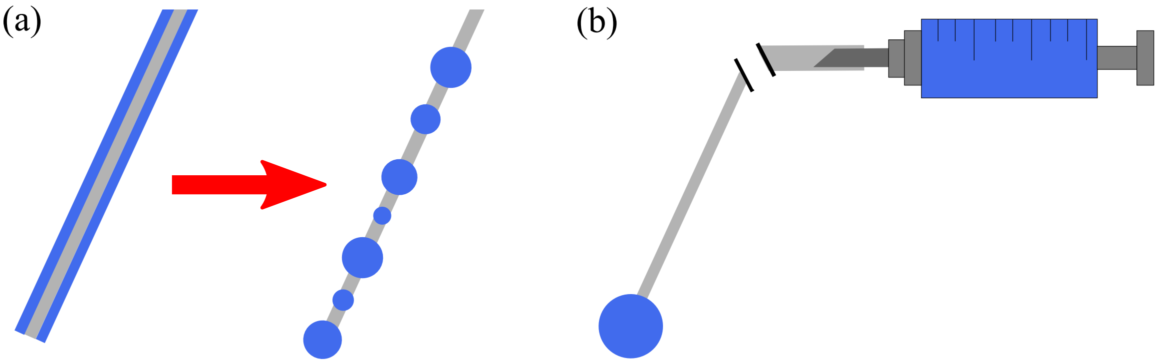

Figure 2.4: (a) The micropipette is coated with a film of the viscous liquid after being removed from the bath. The film rapidly evolves into an array of droplets via the PRI. (b) Droplets can be created at the tip by connecting the micropipette to a syringe containing the liquid.

below the stretched film. The stage was then vertically translated until the substrate formed a strong adhesive contact with the entire elastic film. Finally, the sample was removed from the straining apparatus by cutting the excess stretched film surrounding the substrate with a scalpel.

2.3 Droplet deposition

In all the papers in Chapter 3, with the exception of Paper IV, droplets of sizes in the range $25 < r < 500$ μm were used , where r represents the contact radius of the droplet on the substrate (volumes in the range 1-10^5 fL). These droplets were deposited using various techniques. All of the techniques make use of thin glass micropettes. Micropipettes are fabricated by stretching hollow glass capillary tubes with an inner diameter of 0.7 mm and an outer diameter of 1 mm (World Precision Instruments Inc.) with a specialized pipette puller (Narishige PN-30) over a heated filament. Once pulled, the resultant micropipettes are thin (outer diameter of ~ 20 μm), long (1-3 cm), hollow, and flexible.

In this thesis work, three different test liquids were used to produce droplets: glycerol (Caledon Laboratories Ltd.), polyethylene glycol (PEG) with $M_n = 0.6$ kg/mol (Sigma-Aldrich), and diiodomethane (Sigma-Aldrich, Reagent Plus, 99%). Glycerol and PEG are both non-volatile and much more viscous than water. Thus, when a micropipette is dipped into a bath of these liquids and withdrawn, it entrains a liquid film. The liquid film is unstable and breaks up into droplets via the PRI, as seen in Fig. 2.4(a). The pipette can then be held above a substrate and flicked using a pair of tweezers. This action leads to a "spray" of droplets being deposited on the substrate below. Although this process is poorly controlled in terms of the number of droplets created and their position, it is useful for producing a multitude of droplets simultaneously with a wide range of sizes, including ones which are very small ($r \sim 25$ μm). This technique was employed in Papers I, III, and V, because a multitude of droplets of various sizes were desired. On the other hand, there is usually a droplet which is trapped at the tip of the pipette, as seen in Fig. 2.4(a). This droplet can be directly transferred onto a substrate by gently bringing the two into contact. This technique has the advantage of depositing a single droplet at a controlled position, but is not capable of producing small droplets (typically, $r > 150$ μm). This technique was used exclusively in Paper II, as only two droplets were deposited on a sample, and their location had to be precisely controlled. For an inviscid liquid, such as water or diiodomethane, the above techniques are not suitable, as the micropipette does not entrain a sufficiently thick film when retracted from the bath. Instead, the micropipette can be connected to a syringe containing the liquid to be deposited. By applying pressure to the plunger of the syringe, a small droplet is formed at the tip of the pipette, as depicted in Fig. 2.4(b). Thereafter, the procedure is the same as in the previous technique. This technique was used to deposit diiodomethane droplets in Paper III.

2.4 Contact angle measurements

Contact angle measurements have been performed using two different methods. In the first technique, the droplet (or bulge in a compliant free-standing film) to be measured is viewed from the side with an optical microscope. In Fig. 2.5, we schematize a contact angle measurement on a free-standing isotropic tension film (as described in Section 2.2.1). In this example, the profile of the droplet spherical cap (i.e. corresponding to the liquid-vapour interface) is imaged to measure the droplet contact angle θ_{d}. Bulge contact angles (θ_{b}) are performed in the same way, but the droplet

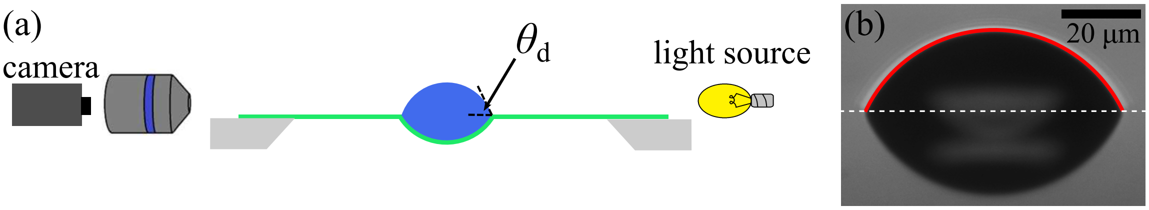

Figure 2.5: (a) Schematic of a side view set-up for contact angle measurements. Here, we depict the contact angle measurement of a droplet on compliant film, but the same set-up is used for rigid substrates as well. (b) An image of a droplet with contact angle $\theta_d = 64 \pm 1^\circ$ determined using Eq. 2.1. The red curve is the best spherical cap fit to the profile. Everything below the white dashed line is a reflection off the film itself.

is deposited on the underside of the film instead. The same experimental set-up is also used for measuring contact angles of droplets on the uniaxial straining set apparatus described in Section 2.2.2 as well as on silicon wafers. An image of the droplet (or bulge) profile is acquired with a camera (Fig. 2.5(b)). The edge of the profile is detected using a thresholding algorithm written in MATLAB, and subsequently fit to a spherical cap of radius R. The reflection of the profile to be measured is seen directly below itself (i.e. everything below the white dashed line in Fig. 2.5(b)), but is not used for any analysis. An image of the droplet (or bulge) is also acquired from a top view by rotating the sample. In doing so, the contact radius r can be precisely measured. Thereafter, the contact angle θ can be determined using the spherical cap identity:

$$\theta = \sin^{-1}\left(\frac{r}{R}\right). \tag{2.1}$$

This technique is most suited for measuring contact angles in the range of $10^\circ < \theta < 85^\circ$. The upper limit exists because Eq. 2.1 is poorly behaved close to 90°, which makes θ difficult to determine in that range. This method was employed in Papers I, II, III, and V to measure contact angles.

In Paper V, contact angles were also determined using interferometry. In this study, droplets were flattened due to being capped by a taut elastic film to contact angles of $3 < \theta < 20^\circ$. These droplets were sufficiently flat that concentric Newton rings were seen when viewed from above with an optical microscope through a red

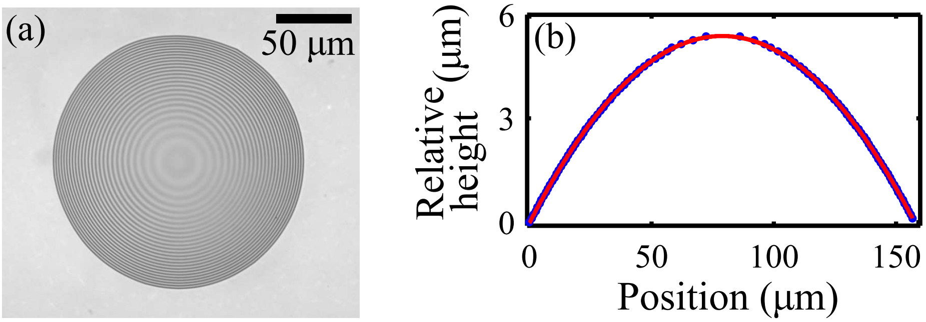

Figure 2.6: (a) Optical image of a flattened droplet capped by an elastic membrane. Interference fringes are seen since the droplet is viewed through a red filter. (b) Plot of the height of the droplet, relative to the height of the first fringe, as a function of position for a horizontal section through the droplet in (a). The spherical cap fit (red curve) is used to determine the contact angle.

monochromatic filter ($\lambda = 632.8$ nm, Newport, 10LF10-633). An example is shown in Fig. 2.6(a). From such an image, the MATLAB function `findpeaks` can be used to detect the locations of the minima and maxima in intensity, corresponding to dark and light fringes, for a section through the center of the droplet. The change in thickness between subsequent light and dark fringes, Δh, is given by:

$$\Delta h = \frac{\lambda}{4n}\,, \tag{2.2}$$

where n is the index of refraction of the liquid. Using this procedure, the height profile of the droplet (relative to the height of the first fringe) can be plotted as a function of position for the particular section (Fig. 2.6(b)). A spherical cap fit (red curve) to the height profile data is then used to extract R, and θ is finally computed using Eq. 2.1.

Chapter 3

Papers

The following chapter contains the papers which comprise the work that is central to this thesis. Each paper will be prefaced with a summary of the project, key findings, and conclusions. Since research is a highly collaborative process, my contribution to each project will be made explicit at the end of each preface. Additional papers for which I am not the main contributor or which are tangential to the theme of this dissertation are listed in Appendix A.

These papers focus on elastocapillary interactions in wetting between liquids and solid films under tension. With the exception of Paper III, all papers study how compliant elastic boundaries cause modifications from wetting phenomena on rigid substrates. In Paper I, we study the deformations produced by partially wetting liquid droplets which are sessile on compliant elastic membranes with isotropic tension. In particular, we measure contact angles of the droplet and bulge, and prove the validity of the Neumann construction depicted in Fig. 1.14. In Paper II, we generalize the system by studying partial wetting on elastic membranes with biaxial tension. In this work, we show that droplets elongate along the high tension direction, and thus serve as "compass needles" for the principal directions in a free-standing elastic film. The Shuttleworth effect is the subject of Paper III. In this project, we use partial wetting to probe how interfacial energies of polymer glasses and elastomers change with strain. We show that polymer glasses do indeed exhibit a Shuttleworth effect, and give strong evidence for the absence of this effect in elastomers. In Paper IV, we return to studying how elastic boundaries alter wetting phenomena. We show that the dewetting of a thin liquid film can be tuned by capping the liquid with an elastic membrane. In particular, elastic boundary conditions permit control of the rate as well as the morphology of dewetting. Finally, in Paper V, we investigate the partial wetting of a liquid which is capped by an elastic membrane. A Young's law construction which incorporates mechanical as well as interfacial tensions captures the measured contact angles. Further, we find that this system can be used to measure the interfacial energy between elastomer and liquid. Once more, we show that elastic boundaries can be exploited for liquid patterning.

3.1 Paper I

Liquid droplets on a highly deformable membrane

R. D. Schulman and K. Dalnoki-Veress, Phys. Rev. Lett., **115**, 206101 (2015).

This paper represents our first attempt at understanding how wetting phenomena are altered in the presence of a compliant elastic boundary. Here, we study the partial wetting of liquid droplets on elastic membranes. Free-standing elastomeric and glassy films are prepared suspended over the hole of a washer and contain an isotropic tension. We observe that droplets produce an elastocapillary deformation, or bulge, in the film below which is comparable in size to the droplet itself, but the surrounding film remains completely planar. By viewing the sample from the side, the global droplet and bulge contact angles (θ_d and θ_b depicted in Fig. 1.14) are measured, and the normalized tension T_in/γ is determined from Eq. 1.56. The value of the tension is found to be uniform throughout the film, and independent of droplet size or the number of droplets deposited, thus validating the notion that these elastic films can be treated as membranes. These tensions are also verified using mechanical indentation measurements with a micropipette deflection technique to measure forces.

Knowing T_in/γ and the Young's angle θ_Y of the liquid on a supported substrate of the solid film, we show that a Neumann construction which incorporates mechanical and interfacial tensions can be used to fully predict the droplet and bulge contact angles. In this way, the partial wetting between a droplet and an elastic membrane is completely analogous to the partial wetting between a droplet and a liquid membrane. As the tension in the film increases, the deformation in the film, and hence θ_b, decreases, whereas θ_d increases. For finite tension, we find that the internal angle ($\theta_\mathrm{d} + \theta_\mathrm{b}$) is larger than Young's angle. In the limit of infinite tension, wherein the film is undeformable, Young-Dupré's law of partial wetting on a rigid solid is recovered.

This project was the idea of Dr. Dalnoki-Veress and myself. Under his guidance, I designed the experimental set-up. Thereafter, I made the samples, performed the experiments, and analyzed the data. Through numerous discussions, Dr. Dalnoki-Veress and I worked out the kinks in the theoretical model together. I wrote the first draft of the manuscript, which was revised by Dr. Dalnoki-Veress.

PRL 115, 206101 (2015) PHYSICAL REVIEW LETTERS week ending 13 NOVEMBER 2015

Liquid Droplets on a Highly Deformable Membrane

Rafael D. Schulman[1] and Kari Dalnoki-Veress[1,2,*]
[1]Department of Physics and Astronomy, McMaster University, 1280 Main St. W, Hamilton, ON, L8S 4M1, Canada
[2]Laboratoire de Physico-Chimie Théorique, UMR CNRS Gulliver 7083, ESPCI, Paris, France

(Received 12 September 2015; published 9 November 2015)

We examine the deformation produced by microdroplets atop thin elastomeric and glassy free-standing films. Because of the Laplace pressure, the droplets deform the elastic membrane thereby forming a bulge. Thus, two angles define the droplet or membrane geometry: the angles the deformed bulge and the liquid surface make with the film. These angles are measured as a function of the film tension, and are in excellent agreement with a force balance at the contact line. Finally, we find that if the membrane has an anisotropic tension, the droplets are no longer spherical but become elongated along the direction of high tension.

DOI: 10.1103/PhysRevLett.115.206101 PACS numbers: 68.03.Cd, 47.55.D-, 68.08.Bc

The interaction between a liquid's surface tension and a solid's elasticity, or elastocapillarity, is relevant in a wide variety of systems including capillary origami and folding [1–4], soft tissues [5–7], wetting of fibers [8–10], and micropatterning of elastomeric surfaces [11–13]. Despite the multitude of applications utilizing this physics, one of the most fundamental properties has only recently started to be understood: the contact angle of a liquid droplet atop a soft solid [14–17].

On rigid substrates, the contact angle of a droplet can be found through a horizontal force balance between the interfacial tensions of the system, known as Young's law [18]. The vertical component of the force is balanced by the elasticity of the solid. In the opposite regime, a liquid droplet atop a liquid substrate, the contact line geometry is determined by a Neumann construction, in which the interfacial tensions are simultaneously balanced in the vertical and horizontal directions [19,20]. Intermediate to these extremes is a droplet atop a soft surface. In such a case, the liquid contact line deforms the solid into a cusp on a length scale given by the elastocapillary length γ/E, where γ is the surface tension and E is Young's modulus [15–17,21–24]. Microscopically, the contact line geometry and local contact angles are described by Neumann's law balancing the surface tension of the liquid with the surface stresses of the solid-vapor and solid-liquid interfaces. The global contact angle, the angle at which the spherical cap intersects the flat undeformed substrate, satisfies Young's law for droplets larger than γ/E [14–17]. However, droplets on the order of γ/E display global contact angles which deviate from Young's law [15]. Elastocapillary phenomena are also present in rigid materials, such as glasses; however, in such cases γ/E is on the order of the molecular size. Therefore, elastocapillary experiments have been limited to soft materials, with moduli on the order of kilo Pascals, to attain deformations and elastocapillary lengths in the μm range.

Alternatively, the length scale of the deformation can be amplified by selecting a more compliant geometry, such as flexible sheets, fibers, or free-standing films, while employing materials with moduli in the MPa to GPa range [1,3,8–10,25–27]. In a seminal study, the surface tension of droplets on free-standing elastomeric films tens of μm thick generated deformations visible to the naked eye [26]. By modeling the system at the contact line, the authors were able to determine the tensions in their films. However, the tensions were never quantitatively verified using other techniques, and the relevant contact angles of the system were solely used to determine the tension and not compared to theoretical expectations.

In this Letter, we present measurements of the global contact angle of droplets atop thin free-standing films of an elastomer ($E \sim$ MPa) and a glass ($E \sim$ GPa) as a function of the tension within the films. We find the contact angles to be in excellent agreement with a Neumann construction in which interfacial and mechanical tensions are balanced at the contact line. In the limit of high tensions, our model and measured contact angles tend towards Young's law. Finally, we show that droplets placed atop films with an anisotropic biaxial tension become elongated in the direction of high tension.

Elastomeric films with thickness ranging from $h \sim 280$ to 3500 nm were prepared from a styrene-isoprene-styrene (SIS) triblock copolymer and subsequently supported on a washer with a circular hole to produce free-standing films 3 mm in diameter [28]. Free-standing glassy films of poly (n-butyl methacrylate) (PnBMA) with $h \sim 65$ to 140 nm were similarly prepared. For the liquid droplets, we use glycerol and polyethylene glycol (PEG). Droplets were placed on either side of the free-standing film as seen in Fig. 1(a) and viewed from the side with an optical microscope. In this geometry, droplets and bulges could be directly imaged on the top side of the washer (the edges of the washer obscures the bottom side). Images of the corresponding droplets or bulges were also obtained from a top view for a more precise measurement of the contact radii r_c [Fig. 1(a)]. Contact angle measurements were performed within ~4 min of droplet deposition to ensure negligible evaporation of the liquid. We found that the

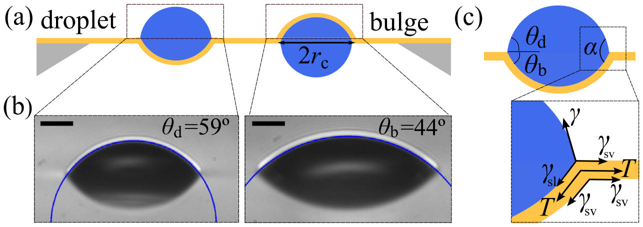

FIG. 1 (color online). (a) Schematic of the side view of liquid droplets on the top and bottom side of the film, not to scale. (b) Microscope images of the side view of a droplet (left) and bulge (right). The top half of the image is the direct visualization of the droplet or bulge, while the bottom half corresponds to a reflection off the film itself. The curves represent spherical cap fits to the profiles. The scale bar represents 20 μm. (c) Schematic of a droplet and bulge with the relevant angles identified. The expanded view shows the interfacial and mechanical tensions acting on the contact line.

contact radii and contact angles of sufficiently large droplets ($r_c > 25$ μm) exhibited negligible change over this experimental time scale. Therefore, our measurements were limited to droplets with $r_c > 25$ μm to be completely confident that evaporation does not play a role.

Examples of optical images of a droplet and bulge are shown in Fig. 1(b). The droplet or bulge profiles are well fit to spherical caps, represented by curves in Fig. 1(b). From each fit, we extract the radius of curvature, R_d or R_b, for droplets and bulges. The droplet and bulge contact angles [Fig. 1(c)], θ_d and θ_b, are defined as the contact angles with which the respective spherical caps intersect the undeformed film and are calculated using the identities $\sin\theta_d = r_c/R_d$, $\sin\theta_b = r_c/R_b$. We find that the contact angles show no systematic dependence on droplet size within the range investigated ($r_c \sim 25$–200 μm). Therefore, on a given sample, several droplets and bulges are deposited and average values of θ_d and θ_b are found. The total internal liquid angle α is simply the sum of the average values of θ_d and θ_b.

As will be justified below, we make the reasonable assumption that only tensile forces (surface tensions and mechanical tension in the film) are relevant and that bending can be neglected. The elastocapillary length (<100 nm) in our system is much smaller than the size of our droplets, so surface stresses of the solid or ridges at the contact line do not influence the global contact angles we measure. Furthermore, the droplet sizes employed are well below the capillary length of the system. Thus, gravitational effects are negligible. In this limit, the film deformation can be understood rather simply. The Laplace pressure within the droplet causes the film below it to bulge into a spherical cap. Outside the droplet, the film is undeformed and flat. In addition, as seen in Fig. 1(c), the contact line geometry results from a force balance between the interfacial tensions of the system and the mechanical tension T within the film. Analogous to a Neumann construction, the liquid-vapor γ, solid-liquid γ_{sl}, and solid-vapor surface tensions γ_{sv} tug at the triple point. However, we must also include the additional contributions from the mechanical tension in the film, as well as the solid-vapor surface tensions present on the opposite side of the film. We label the three tensions pulling the film down as $T_{in} \equiv T + \gamma_{sl} + \gamma_{sv}$ and the three tensions pulling away from the droplet as $T_{out} \equiv T + 2\gamma_{sv}$. We assume that T is the same in the region under the droplet compared to outside the droplet. From the definitions of T_{in} and T_{out}, we see that $T_{out} = T_{in} - \gamma_{sl} + \gamma_{sv} = T_{in} + \gamma\cos\theta_y$, where θ_y is the Young's angle of the liquid atop a supported substrate of the material, which we measure independently. A vertical force balance at the contact line yields

$$\frac{T_{in}}{\gamma} = \frac{\sin\theta_d}{\sin\theta_b}, \tag{1}$$

which can also be attained by balancing the Laplace pressure with the restorative pressure from the film. Equation (1) is convenient: the normalized tension T_{in}/γ is obtained from the measured angles θ_d and θ_b. A similar approach (assuming $\alpha = \theta_y$) has been employed to determine tensions in thicker films [26]. Furthermore, we use the cosine law to obtain

$$\cos\theta_d = \frac{(T_{out}/\gamma)^2 + 1 - (T_{in}/\gamma)^2}{2T_{out}/\gamma} \tag{2a}$$

$$\cos\theta_b = \frac{(T_{out}/\gamma)^2 - 1 + (T_{in}/\gamma)^2}{2T_{out}T_{in}/\gamma^2}, \tag{2b}$$

where we have made use of the fact that the film is flat outside the droplet. Since $T_{out} = T_{in} + \gamma\cos\theta_y$, we see that Eq. (2) allows us to predict the individual contact angles knowing the Young's angle and the normalized tension T_{in}/γ given by Eq. (1). Similarly, the total internal angle α is given by

$$\cos\alpha = \cos\theta_y - \frac{\gamma}{2T_{in}}\sin^2\theta_y. \tag{3}$$

In the limit of $T_{in}/\gamma \to \infty$ the equations reduce to $\theta_d \to \theta_y$, $\alpha \to \theta_y$, and $\theta_b \to 0$. That is, in the limit of high tensions, we recover Young's law, since the droplet is sessile on a completely rigid substrate. In Figs. 2(a) and Fig. 2(b) we plot our data for θ_d and θ_b as a function of T_{in}/γ found using Eq. (1) for glycerol on SIS and PnBMA. The droplet contact angle increases with increasing tension while the bulge contact angle decreases as the surface becomes less deformable at high tensions. Various tensions were achieved by changing film thickness and through sample-to-sample variation [29]. We find thicker films to have a higher tension, in accordance with previous work [26]. In Fig. 2(c) we plot the total internal liquid angle α

against the normalized tension and find it to decrease with higher tension. It is important to note that at all finite tensions one has $\theta_d < \theta_y$ while $\alpha > \theta_y$. This result is in contrast with previous studies which have assumed α to be constant and equal to the contact angle on a supported substrate [26,27]. In Figs. 2(a)–2(c), the predictions of Eqs. (2) and (3) are plotted, with the Young's angle of glycerol atop SIS fixed to $81 \pm 1.5°$. The simple force balance at the contact line captures the data, validating that at finite tensions the contact angles can be found through a Neumann construction which includes interfacial and mechanical tensions. As $T_{\text{in}}/\gamma \to \infty$ Young's law is recovered. In Figs. 2(a)–2(c) the SIS and PnBMA data are found to collapse onto the same curve, despite being completely different materials. This collapse is due to the coincidental fact that Young's angle of glycerol on SIS is equal to the Young's angle of glycerol on PnBMA $(82.5 \pm 1.5°)$ within experimental error. Since the theoretical curves are completely determined by T_{in}/γ (as seen in the plots) and θ_y, the data fall along the same curve.

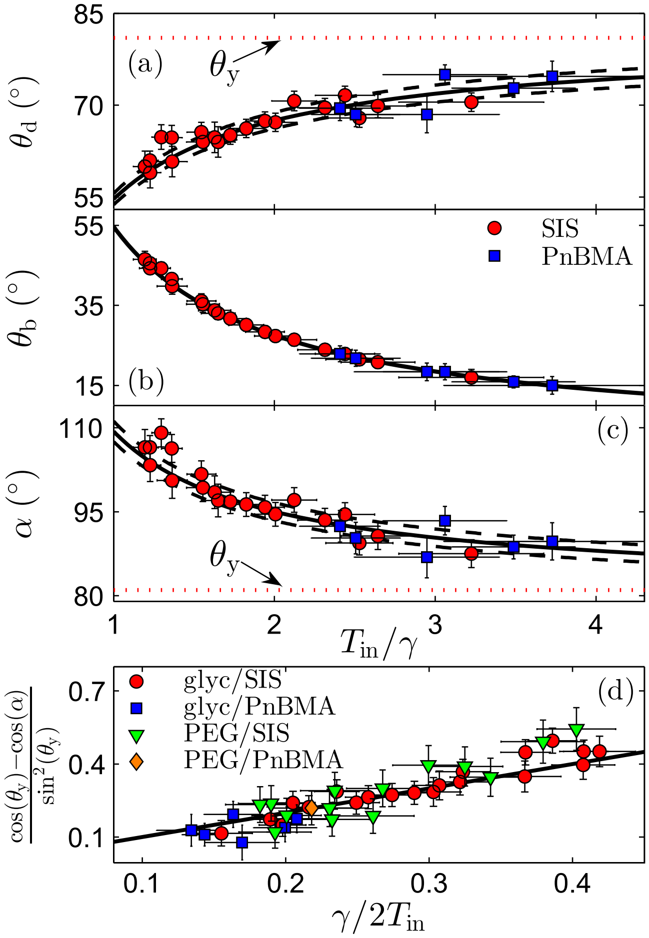

FIG. 2 (color online). (a) The droplet contact angle, (b) the bulge contact angle, and (c) the total internal liquid angle plotted as a function of the normalized tension [see Eq. (1)] for glycerol on SIS (circles) and glycerol on PnBMA (squares). The curves are Eq. (2) and Eq. (3) with θ_y given by the Young's angle of glycerol on SIS (represented by the dotted horizontal lines). The dashed black lines are bounds to the theory due to uncertainty in θ_y. The uncertainty in the theoretical curve for θ_b is on the order of the thickness of the curve itself. (d) $(\cos\theta_y - \cos\alpha)/\sin^2\theta_y$ as a function of $\gamma/2T_{\text{in}}$ for four liquid-substrate combinations. The black line is the theoretical prediction. The vertical and horizontal error bars stem from uncertainties in the measured values of θ_d and θ_b.

In the model, we assume the mechanical tension T to be the same in the region under the droplet compared with the rest of the film. In fact, the theoretical curves in Figs. 2(a)–2(c) are remarkably sensitive to this assumption. If we, for instance, enforce the two tensions to differ by as little as 5 mN/m (which corresponds to only 7% of T_{in} for the lowest tension data), the theoretical curves are inconsistent with the data [28]. Therefore, the assumption of constant mechanical tension throughout the film must be valid.

We also perform experiments with another liquid, PEG, atop SIS and PnBMA, for which the Young's angle is substantially different from glycerol $(55.3 \pm 1.5°$ and $58.4 \pm 1.5°)$. To demonstrate that the theory is valid for all tested combinations of liquid and substrate material, we can rearrange Eq. (3) into the following form $(\cos\theta_y - \cos\alpha)/\sin^2\theta_y = \gamma/2T_{\text{in}}$. In Fig. 2(d), we plot the left hand side of this equation against $\gamma/2T_{\text{in}}$ for the four liquid-substrate combinations tested. As expected, these data all fall along a line of unity slope passing through the origin. The measured droplet and bulge contact angles are also well predicted by Eq. (2) for PEG [28].

In our experiments, we obtain T_{in}/γ from $\sin\theta_d/\sin\theta_b$. Although this procedure was used in a previous study, the tensions were never quantitatively verified using alternate methods [26]. In order to completely demonstrate the success of the model, we must test the measured tensions against some predictions. First, if the tension of the same film is measured with two different liquids, glycerol, and PEG, then $T_{\text{in,PEG}} = T_{\text{in,glyc}} - \gamma_{\text{sl,PEG}} + \gamma_{\text{sl,glyc}} = T_{\text{in,glyc}} - \gamma_{\text{glyc}}\cos\theta_{y,\text{glyc}} + \gamma_{\text{PEG}}\cos\theta_{y,\text{PEG}}$, where subscripts PEG and glyc denote the two liquids. Substituting in literature values for $\gamma_{\text{PEG}} = 46$ mN/m and $\gamma_{\text{glyc}} = 63$ mN/m [30,31], the expected relationship becomes $T_{\text{in,PEG}} = T_{\text{in,glyc}} - (16 \pm 3\ \text{mN/m})$. We performed simultaneous tension measurements using the two liquids atop SIS as seen in Fig. 3(a). The data are well fit to a line of slope 0.98 ± 0.07 and intercept of -22 ± 8 mN/m, which agrees with the theoretical result within error. The difference in the intercept can be explained by discrepancies in the literature values of γ for our liquids.

To further validate the tensions obtained with the droplets, we also measure the tensions mechanically using a home built micropipette deflection apparatus [32]. In this technique, the tip of a flexible micropipette, which serves as a force transducer, is pressed against the film. In doing so, the deformation of the membrane as well as the force acting

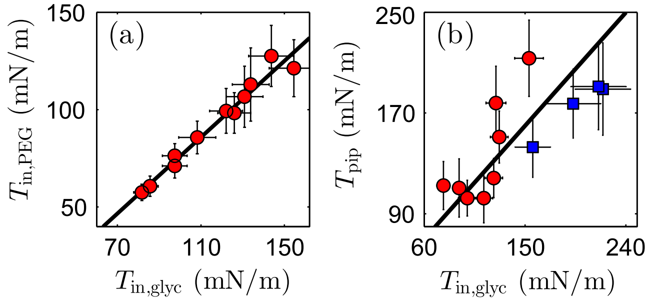

FIG. 3 (color online). (a) The tension as measured with PEG compared to those measured with glycerol on the *same* SIS sample. The black line is a linear fit to the data. (b) The tension as measured with micropipette deflection correlated to those measured with glycerol on SIS (circles) and PnBMA (squares). The black line represents the theoretical relationship, where the thickness of the line is indicative of its upper and lower bound given uncertainties in θ_y. Error bars for liquid tensions stem from uncertainties in determining θ_d and θ_b, whereas error bars for pipette tensions arise from uncertainties in the spring constant of the pipette as well as in measuring the deformation of the film.

on it are known. Since the shape of a taut membrane between two axisymmetric rings (the pipette tip and washer) is known [33], we can determine the tension from the force-deformation data. The measured tension must be equal to $T_{\mathrm{pip}} = T + 2\gamma_{\mathrm{sv}} = T_{\mathrm{in}} + \gamma \cos\theta_y$. Measurements were carried out on both SIS and PnBMA films [34], and the results of T_{pip} as a function of $T_{\mathrm{in,glyc}}$ are displayed in Fig. 3(b). The data are in agreement with the expected trend. Any systematic differences between the SIS and PnBMA data can be attributed to differences in adhesion between the pipette and the respective films, as well as bending being locally important near the pipette tip and influencing the measured tensions. The pipette measurements are prone to scatter due to the alignment of the pipette relative to the film. As evidenced by the significantly reduced scatter in Fig. 3(a), we conclude that tension is more accurately measured using the droplet technique. These tests show that the model is fully consistent in terms of both tension and contact angle data.

Recently, there has been disparity in the literature regarding whether or not the surface tension of an elastomeric film is equal to its surface free energy [26,35]. Following the procedure of Ref. [26], the surface tension of the film can be found by computing the extrapolated zero-thickness value of T_{in} for a SIS film with glycerol droplets. In doing so, we find that $T_{\mathrm{in}} \sim 60$ mN/m. This surface tension compares well with the surface free energy of the film under the droplet, given by $\gamma_{\mathrm{sv}} + \gamma_{\mathrm{sl}} = 2\gamma_{\mathrm{sv}} - \gamma \cos\theta_y \sim 50$ mN/m [36–38].

In this Letter, we make the assumption that our system is dominated by tension and that bending can be neglected. That is, stretching dominates, and the influence of bending is only manifested in a small region around the contact line of characteristic size $\sqrt{Eh^3/12T_{\mathrm{tot}}}$, where T_{tot} is the total tension in the film [26,27]. In our experiments this region is maximally ~ 4 μm but most typically below ~ 2 μm, and thus small in comparison to the droplet sizes employed in this study, indicating that bending can be safely ignored in both materials. The fact that bulges and droplets are well fit to spherical caps and that the contact angles are size independent further validates the assumption.

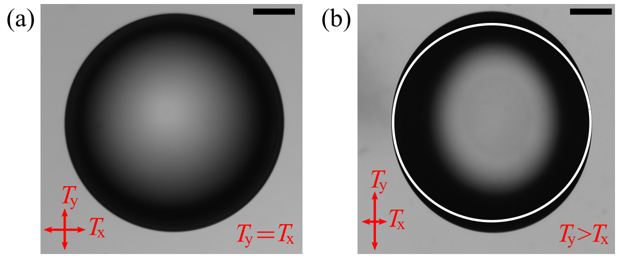

FIG. 4 (color online). (a) Top view of a water droplet atop a SIS film with isotropic tension ($T_x = T_y$). The droplet is round when viewed from above. (b) Top view of a water droplet atop a SIS film which has been stretched in the y direction ($T_y > T_x$). A white circle is superimposed to emphasize that the droplet is elongated along the direction of high tension. The scale bar represents 50 μm.

We have performed experiments with droplets atop thin free-standing films, wherein the surface tension of the liquid produces significant deformation of the film. We measure contact angles of the droplets and bulges relative to the flat film, as well as the total internal liquid angle, and find these to be well described by a Neumann construction in which the interfacial and mechanical tensions are balanced at the contact line. In the high tension limit, the film is essentially undeformable, and Young's law is recovered. Conversely, in the limit of vanishing mechanical tension, we expect to recover the classical Neumann construction where only interfacial tensions are balanced. The tensions we measured using the droplet experiments, which have contributions from both mechanical and interfacial tensions, were quantitatively verified using a purely mechanical technique and by comparing the measured tensions from two different liquids. The experiments described in this manuscript were carried out on a film with a constant isotropic tension, in which case the droplets are perfectly round when viewed from above, as seen in Fig. 4(a). However, an interesting option exists that does not for a droplet on a simple liquid: if a film is floated onto a support and then preferentially stretched along one axis, then the droplets no longer assume a circular equilibrium contact. In Fig. 4(b), a liquid droplet has been placed atop a film which has been stretched in the vertical (y) direction. The droplets become elongated along the axis of higher tension which provides an exciting opportunity for studying equilibrium liquid droplets that deviate from the expected geometry.

The authors are grateful to Anand Jagota, René Ledesma-Alonso, Elie Raphaël, and Thomas Salez for valuable discussions. Discussions with Salez and Raphaël stimulated these experiments. The financial support by Natural Science and Engineering Research Council of Canada is gratefully acknowledged.

Note added.—We refer the reader to current theoretical work on the topic by Hui and Jagota [39].

---

[*] dalnoki@mcmaster.ca

[1] C. Py, P. Reverdy, L. Doppler, J. Bico, B. Roman, and C. N. Baroud, Phys. Rev. Lett. **98**, 156103 (2007).

[2] N. Patra, B. Wang, and P. Král, Nano Lett. **9**, 3766 (2009).

[3] J. van Honschoten, J. Berenschot, T. Ondarcuhu, R. Sanders, J. Sundaram, M. Elwenspoek, and N. Tas, Appl. Phys. Lett. **97**, 014103 (2010).

[4] J. Bae, T. Ouchi, and R. C. Hayward, ACS Appl. Mater. Interfaces **7**, 14734 (2015).

[5] O. Campàs, T. Mammoto, S. Hasso, R. A. Sperling, D. O'Connell, A. G. Bischof, R. Maas, D. A. Weitz, L. Mahadevan, and D. E. Ingber, Nat. Methods **11**, 183 (2014).

[6] J. B. Grotberg and O. E. Jensen, Annu. Rev. Fluid Mech. **36**, 121 (2004).

[7] A. L. Hazel and M. Heil, Proc. R. Soc. A **461**, 1847 (2005).

[8] C. Duprat, S. Protiere, A. Y. Beebe, and H. A. Stone, Nature (London) **482**, 510 (2012).

[9] J. Bico, B. Roman, L. Moulin, and A. Boudaoud, Nature (London) **432**, 690 (2004).

[10] A. Fargette, S. Neukirch, and A. Antkowiak, Phys. Rev. Lett. **112**, 137802 (2014).

[11] S. Shojaei-Zadeh, S. R. Swanson, and S. L. Anna, Soft Matter **5**, 743 (2009).

[12] R. W. Style, Y. Che, S. J. Park, B. M. Weon, J. H. Je, C. Hyland, G. K. German, M. P. Power, L. A. Wilen, J. S. Wettlaufer *et al.*, Proc. Natl. Acad. Sci. U.S.A. **110**, 12541 (2013).

[13] A. Chakrabarti and M. K. Chaudhury, Langmuir **29**, 6926 (2013).

[14] R. W. Style and E. R. Dufresne, Soft Matter **8**, 7177 (2012).

[15] R. Style, R. Boltyanskiy, Y. Che, J. Wettlaufer, L. A. Wilen, and E. Dufresne, Phys. Rev. Lett. **110**, 066103 (2013).

[16] A. Marchand, S. Das, J. H. Snoeijer, and B. Andreotti, Phys. Rev. Lett. **109**, 236101 (2012).

[17] S. J. Park, B. M. Weon, J. S. Lee, J. Lee, J. Kim, and J. H. Je, Nat. Commun. **5**, 4369 (2014).

[18] T. Young, Phil. Trans. R. Soc. A **95**, 65 (1805).

[19] F. E. Neumann, *Vorlesungen über die Theorie der Capillarität* (BG Teubner, Leipzig, 1894).

[20] P. de Gennes, F. Brochard-Wyart, and D. Quere, *Capillarity and Wetting Phenomena* (Springer, New York, 2008).

[21] G. Lester, J. Colloid Sci. **16**, 315 (1961).

[22] R. Pericet-Cámara, A. Best, H. J. Butt, and E. Bonaccurso, Langmuir **24**, 10565 (2008).

[23] E. R. Jerison, Y. Xu, L. a. Wilen, and E. R. Dufresne, Phys. Rev. Lett. **106**, 186103 (2011).

[24] C.-Y. Hui and A. Jagota, Proc. R. Soc. A **470**, 20140085 (2014).

[25] J. Huang, M. Juszkiewicz, W. H. de Jeu, E. Cerda, T. Emrick, N. Menon, and T. P. Russell, Science **317**, 650 (2007).

[26] N. Nadermann, C.-Y. Hui, and A. Jagota, Proc. Natl. Acad. Sci. U.S.A. **110**, 10541 (2013).

[27] C.-Y. Hui, A. Jagota, N. Nadermann, and X. Xu, Procedia IUTAM **12**, 116 (2015).

[28] See Supplemental Material at http://link.aps.org/supplemental/10.1103/PhysRevLett.115.206101 for a more detailed overview of the sample preparation, a plot of θ_d and θ_b vs T_{in}/γ for PEG atop SIS with the prediction of Eq. (2) included, and a plot supporting the assumption that T is the same in the film under the droplet and outside the droplet.

[29] The tension in the film is a result of the sample preparation and is not found to change appreciably as droplets are deposited.

[30] G. Korosi and E. Kovats, J. Chem. Eng. Data **26**, 323 (1981).

[31] D. R. Lide, *CRC Handbook of Chemistry and Physics* (CRC Press, Boca Raton, 2004), p. 6.

[32] M. J. Colbert, A. N. Raegen, C. Fradin, and K. Dalnoki-Veress, Eur. Phys. J. E **30**, 117 (2009).

[33] A. N. Raegen, K. Dalnoki-Veress, K.-T. Wan, and R. A. L. Jones, Eur. Phys. J. E **19**, 453 (2006).

[34] In these experiments, $T_{\mathrm{in,glyc}}$ was measured on the film either before or after the pipette measurements had been taken, but no systematic difference in T_{pip} with respect to the order of the measurements was found. Both measurements were performed on the same film with the exception of the thinnest SIS and PnBMA films which were too fragile to be subject to both measurements without damaging the integrity of the samples.

[35] A. Chakrabarti and M. K. Chaudhury, Langmuir **31**, 1911 (2015).

[36] B. Zuo, F. F. Zheng, Y. R. Zhao, T. Chen, Z. H. Yan, H. Ni, and X. Wang, Langmuir **28**, 4283 (2012).

[37] S. Wu, J. Phys. Chem. **74**, 632 (1970).

[38] L.-H. Lee, J. Polym. Sci. Pol. Phys. **5**, 1103 (1967).

[39] C.-Y. Hui and A. Jagota, Soft Matter, doi:10.1039/C5SM02157J (2015).

Liquid Droplets on a Highly Deformable Membrane: Supplemental Information

Rafael D. Schulman[1] and Kari Dalnoki-Veress[1, 2, *]
[1] *Department of Physics and Astronomy, McMaster University,*
1280 Main St. W, Hamilton, ON, L8S 4M1, Canada
[2] *Laboratoire de Physico-Chimie Théorique, UMR CNRS Gulliver 7083, ESPCI, Paris, France*

(Dated: October 18, 2015)

SUPPLEMENTARY METHODS

Elastomeric films were prepared from a styrene-isoprene-styrene (SIS) triblock copolymer (Sigma-Aldrich) with a 14% styrene content. Solutions of SIS in toluene (Fisher Scientific, Optima grade) were prepared with various weight fractions. Upon spincoating these solutions, the triblock copolymers self-assemble to form an elastomeric material in which the matrix is composed of polyisoprene while the polystyrene segments form glassy spheres which serve as physical crosslinks. The SIS solutions were spincoated onto freshly cleaved mica substrates (Ted Pella Inc.) to produce uniform (<10% variation) films with thicknesses in the range of $h \sim 280$ nm - 3500 nm, measured using ellipsometry (Accurion, EP3). The films were floated onto the surface of an ultrapure water bath (18.2 MΩ·cm, Pall, Cascada, LS) and subsequently picked up by a circular metal washer to produce free-standing films 3 mm in diameter. Free-standing glassy films of poly(n-butyl) methacrylate (PnBMA) with number averaged molecular weight $M_n =$ 66 kg/mol and polydispersity index PI = 1.05 (Polymer Source Inc.) of thicknesses in the range of $h \sim 65$ nm - 140 nm (with <5% variation) were made following the same protocol. These free-standing films were heated above the glass transition (at 42°) for 1 min to eliminate wrinkles and ensure the films were taut. For the liquid droplets, we use glycerol (Caledon Laboratories Ltd.) and polyethylene glycol (PEG) with $M_n = 0.6$ kg/mol (Sigma-Aldrich).

SUPPLEMENTARY RESULTS

Contact angle experiments on SIS were performed using both glycerol and PEG. In Fig. S1, we plot θ_{d} and θ_{b} as a function of T_{in}/γ for both glycerol (red) and PEG (blue) atop SIS. The circle markers indicate droplet contact angles, while bulge contact angles are represented by square markers. Evidently, the contact angle data of PEG assumes the same qualitative behaviour as the glycerol data, but the PEG contact angles are smaller due to the smaller Young's angle atop a supported SIS substrate. In Fig. S1, the theoretical predictions for the contact angles are plotted as solid curves for θ_{d} and dashed curves for θ_{b}. We see that the PEG data is also in excellent agreement with the theoretical predictions.

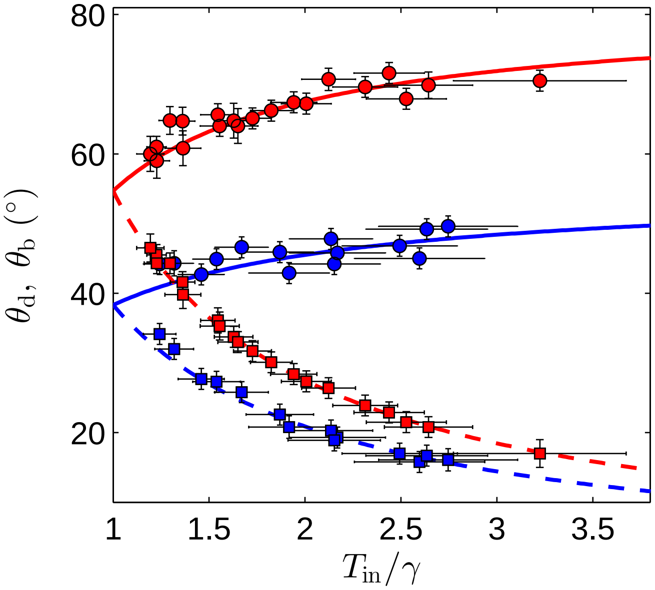

FIG. S1. The droplet and bulge contact angles as a function of the normalized tension atop SIS films. The red markers correspond to glycerol and the blue markers correspond to PEG. Circle markers indicate droplet contact angles and square markers indicate bulge contact angles. The curves represent theoretical predictions from Eq. 2 in the main text for glycerol on SIS (red) and PEG on SIS (blue), where the appropriate θ_{y} has been inputted. Solid curves indicate predictions for θ_{d} and dashed curves indicate predictions for θ_{b}.

In developing our theoretical prediction, we make the reasonable assumption that the mechanical tension in the film is the same in the portion of the film directly below the droplet and in the undeformed film. In fact, we find the theoretical predictions to be very sensitive to this assumption. In Fig. S2, θ_{d} (circle markers) and θ_{b} (square markers) are plotted against T_{in}/γ for glycerol atop SIS. The red curves correspond to the theoretical predictions (given by Eq. 2 in the main text) for the droplet (solid curve) and bulge (dashed curve) contact angles. Now, if we enforce that the mechanical tension in the two regions differs by as little as 5 mN/m in our model, we attain new predictions for the contact angles, shown in blue in Fig. S2. Upper/lower blue curves for θ_{d} and θ_{b} correspond to the mechanical tension being smaller/larger in the undeformed film compared to the film below the droplet. A 5 mN/m tension change corresponds to only

7% of T_{in} for the lowest tension data on the plot and 2.5% for the highest tension data. We see that even for a small change in the tension, the curves systematically deviate from the data. In addition, this systematic difference grows larger as the tension change is increased. Evidently, even a small difference in T for the two regions causes the theory to fail systematically, indicating that our data is fully consistent with the assumption we have made.

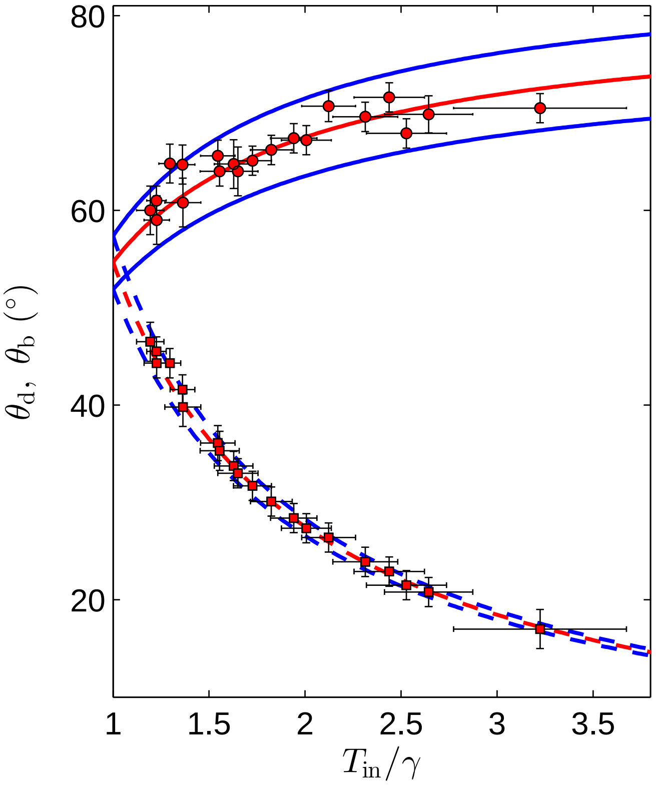

FIG. S2. The droplet and bulge contact angles as a function of the normalized tension for glycerol atop SIS films. Circle markers indicate droplet contact angles and square markers indicate bulge contact angles. The curves represent theoretical predictions from Eq. 2 in the main text for glycerol on SIS, where solid curves indicate predictions for θ_{d} and dashed curves indicate predictions for θ_{b}. The blue curves represent the theoretical curves when T is enforced to be different by 5 mN/m in the two regions. Upper/lower blue curves for θ_{d} and θ_{b} correspond to T being smaller/larger in the region outside the droplet compared to inside.

---

* dalnoki@mcmaster.ca

3.2 Paper II

Liquid droplets act as "compass needles" for the stresses in a deformable membrane

R. D. Schulman, R. Ledesma-Alonso, T. Salez, E. Raphaël and K. Dalnoki-Veress, Phys. Rev. Lett, **118**, 198002 (2017).

In this project, we again study partial wetting on a compliant elastic membrane, but generalize the system from the previous paper by using films with biaxial tension. Free-standing elastic films are prepared on a home-built apparatus which allows the films to be strained uniaxially. We find that droplets deposited on these films assume a shape which is elongated along the high tension direction. In addition, the film surrounding the droplet is no longer planar, but depressed on the low tension side of the wetting region, and raised on the high tension side of the wetting region. Using optical contact angle measurements, we perform measurements of θ_d and θ_b along both high and low tension directions. In addition, we use optical profilometry to map the out-of-plane deformation of the film surrounding the wetting region, and measure the angle subtended by the membrane at the contact line relative to the horizontal (θ_m) along the high and low tension axes. Using these two methods, the angles between the three surfaces at the contact line (defined by the angles $\theta_\mathrm{d} + \theta_\mathrm{m}$, $\theta_\mathrm{d} + \theta_\mathrm{b}$, $\theta_\mathrm{b} - \theta_\mathrm{m}$) are completely determined along both the high and low tension axes. We appeal to an independent Neumann construction along each of these axes, which dictates the contact line geometry as a function of θ_Y, as well as $T_\mathrm{in,high}/\gamma$ for the high tension direction or $T_\mathrm{in,low}/\gamma$ for the low tension direction. Fitting the three measured angles $\theta_\mathrm{d} + \theta_\mathrm{m}$, $\theta_\mathrm{d} + \theta_\mathrm{b}$, $\theta_\mathrm{b} - \theta_\mathrm{m}$ to the Neumann construction prediction along the two orthogonal axes lets us independently extract $T_\mathrm{in,high}/\gamma$ and $T_\mathrm{in,low}/\gamma$.

We use minimal theoretical arguments incorporating the elastocapillary membrane deformation (by solving Eq. 1.46) and the Neumann construction at the contact line to generate several predictions. We forge predictions for the shape of the droplet's footprint (i.e. projection of the wetting region onto the horizontal plane), the aspect ratio of the elongated droplets, and the vertical oscillation of the contact line position around the circumference of the wetting region. For all of these, we find good agreement between the model results and experimental data.

Since droplets elongate along the high tension axis in a region of biaxial tension, it also implies that their short and long axes align with the principal directions in the membrane. To test this principle more generally, we perform separate experiments where films are made with different tension fields in which the principal directions are known. In one experiment, we show that droplets which are deposited near the bowed free boundaries of the film elongate in the direction which is tangential to the boundary. This is consistent with the fact that the principal directions at a free boundary of a film are oriented normal and tangential to the boundary (Section 1.3.2). Furthermore, we deposit droplets on a film with an initially isotropic tension which is subsequently subjected to a pure shear stress τ_{xy}. Droplets elongate such that their major axes are oriented at 45° to the x- and y-axes, in complete accordance with the expected orientation of the principal directions (refer to Eq. 1.35). Thus, we conclude that droplets act as "compass needles" to map out the tension field in an elastic membrane.

This project arose as a natural extension of the former study. Here, I designed the experimental protocol and created the straining apparatus. Once again, I made the samples, performed the measurements, and analyzed the data. The theoretical work was a collaborative effort between Dr. Ledesma-Alonso and I, with significant input from Dr. Salez, Dr. Dalnoki-Veress, and Dr. Raphaël. I wrote the first draft of the manuscript, which was subsequently edited by all the other contributors.

Liquid Droplets Act as "Compass Needles" for the Stresses in a Deformable Membrane

Rafael D. Schulman,[1] René Ledesma-Alonso,[2,3] Thomas Salez,[3,4] Elie Raphaël,[3] and Kari Dalnoki-Veress[1,3,*]
[1]*Department of Physics and Astronomy, McMaster University, 1280 Main Street West, Hamilton, Ontario, L8S 4M1, Canada*
[2]*CONACYT—Universidad de Quintana Roo, Boulevar Bahía s/n, Chetumal, 77019 Quintana Roo, México*
[3]*Laboratoire de Physico-Chimie Théorique, UMR CNRS Gulliver 7083, ESPCI Paris, PSL Research University, 75005 Paris, France*
[4]*Global Station for Soft Matter, Global Institution for Collaborative Research and Education, Hokkaido University, Sapporo, Hokkaido 060-0808, Japan*

(Received 1 March 2017; published 11 May 2017)

We examine the shape of droplets atop deformable thin elastomeric films prepared with an anisotropic tension. As the droplets generate a deformation in the taut film through capillary forces, they assume a shape that is elongated along the high tension direction. By measuring the contact line profile, the tension in the membrane can be completely determined. Minimal theoretical arguments lead to predictions for the droplet shape and membrane deformation that are in excellent agreement with the data. On the whole, the results demonstrate that droplets can be used as probes to map out the stress field in a membrane.

DOI: 10.1103/PhysRevLett.118.198002

The physics of liquid droplets in contact with soft or deformable solids, elastocapillarity, is an active subject of research. Between capillary origami and wrinkling instabilities of thin films [1–9], the bending, coiling, and winding of slender structures [10–16], and elasticity-mediated propulsion of droplets [17–19], there is no shortage of complexity, self-assembly, or beautiful examples of pattern formation in the field. In addition, some recent results have forced us to question familiar concepts of solid-liquid interactions. For instance, studies on the partial wetting of liquid drops on soft solids show that Young's law is applicable on length scales much larger than the bulk elastocapillary length γ/E, where γ is the liquid-air surface tension and E is the Young's modulus of the solid. However, on smaller length scales, the contact line reveals a wetting ridge set by a Neumann construction involving surface stresses [20–26].

Partial wetting on deformable substrates may also be studied by employing a highly compliant geometry, such as a droplet on a thin freestanding film [27–31]. These studies have considered clamped films which are held taut and support a uniform and isotropic tension. As shown in Fig. 1(a), the Laplace pressure of the droplet creates a bulge in the film below it, in the shape of a spherical cap, which is of the same order in size as the droplet itself. The deformations generated may be orders of magnitude larger than the bulk elastocapillary length, because stretching of the membrane is the relevant mode of elasticity [28–31]. The contact line profile is determined by a Neumann construction, which incorporates both mechanical and interfacial tensions. This profile is characterized by the angles subtended by the liquid (θ_d) and bulge (θ_b) to the surrounding film [Fig. 1(a)], which remains completely flat, i.e., the film's angle relative to the horizontal $\theta_m = 0$. From the Neumann construction, these angles are set by two parameters: the Young's angle θ_Y of the same solid supported on a rigid substrate and the ratio T_{in}/γ, where T_{in} is the total mechanical and interfacial tension acting inside the contact region of the membrane or drop system [31]. In the limit of infinite tension, the bulge vanishes and Young's law is recovered.

In this study, we explore the partial wetting of a liquid droplet resting on an elastomeric membrane with an anisotropic tension. Surprisingly, the droplet assumes a shape which is elongated along the direction of high tension. We show from minimal theoretical considerations that the tensions in the film determine both the elongated shape of the wetting region and an observed out-of-plane deformation of the film surrounding the droplet. Therefore, liquid droplets serve as nondestructive probes for mapping out the stress field in a membrane.

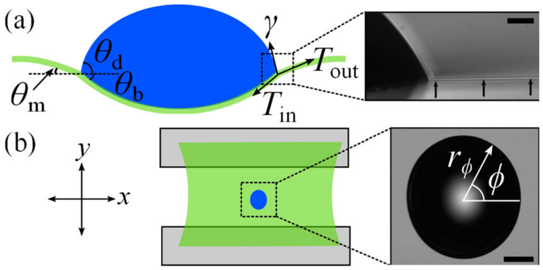

FIG. 1. (a) Schematic of the side view of the drop and membrane system. The contact angle profile is determined by the force balance shown. On the right, an optical image of the contact line region taken along the x direction is shown. The dark part is the liquid, the lighter gray part below is simply a reflection of the droplet off the film, and the thin light curve on the right (indicated by arrows) is the film itself. (b) Schematic of a freestanding elastomeric film between two supports with a single droplet atop. An optical top view image of the droplet is shown on the right. Scale bars = 200 μm.

Freestanding elastomeric films of thickness $h \sim 240$ nm were prepared from Elastollan TPU 1185A (BASF) and suspended between two supports, as seen in Fig. 1(b) [32]. The sample is then stretched along the y direction to produce a biaxial mechanical tension T, such that $T_y > T_x$. As can be seen in Fig. 1(b), since the edges in the x direction of the film are free, the membrane assumes a bowed configuration. However, at the center of the film, far from the edges, there is a biaxial tension which is uniform. In an experiment, a droplet of glycerol is placed near the center of the film. In doing so, we find that the droplet assumes a noncircular footprint which is elongated along the high tension direction [Fig. 1(b)]. Initially, the contact line is seen to move as the droplet configuration equilibrates, indicating that there is no pinning in our system. Thus, we wait until the contact line reaches equilibrium (~5 min) before performing measurements. We advise that contact angle hysteresis should be minimized *a priori* so that equilibrium contact angles are indeed measured. Optical contact angle measurements are performed by viewing the sample from the side. These measurements are taken in two directions: viewing the sample from the x direction, where the bulge and liquid-air interface can be simultaneously seen [as in Fig. 1(a)], and viewing the sample from the y direction. When observing from the y direction, the supports block the view of the lower side of the film; hence, two separate droplets are needed, one on the top side and one on the bottom side of the film, to get images of both the bulge and liquid-air interface. Images of the two droplets are also taken from above, from which we obtain precise measurements of the contact radii r_x and r_y and, hence, the aspect ratio $\epsilon \equiv r_y/r_x$. We use droplets with contact radii in the range of $300-450$ μm, small enough that gravity does not play a role but large enough that evaporation does not influence our measurements over the experimental time scale. The droplets are much smaller than the overall lateral size of the film.

A sample optical image taken from the x direction is shown in Fig. 2(a), where the droplet is sessile on top of the film, generating a bulge below it. The true 3D shape of the liquid-air interface is unknown. Nevertheless, its interface must have a constant mean curvature to ensure a constant internal pressure. However, to simplify our analysis, we fit all liquid-air interface profiles to circular caps and extract the average radii of curvature $R_{d,x}$ and $R_{d,y}$. As can be seen by the solid curve in Fig. 2(a), these fits exhibit excellent agreement with our experimental images [32]. We note that $R_{d,y} > R_{d,x}$ in further support that the droplet's shape is not spherical. Knowing r_i and R_i in each direction $i = x, y$, the contact angles $\theta_{d,x}$ and $\theta_{d,y}$ [defined as the angles the liquid-air cap makes at the contact line relative to the $x-y$ plane as seen in Fig. 1(a)] can be determined. Furthermore, the bulge profiles are fit to parabolas, the justification for which will be provided later. As can be seen by the dashed curve in Fig. 2(a), we find these fits to capture the bulge profile well [32]. From these fits, we determine $\theta_{b,x}$ and $\theta_{b,y}$, defined as the angles the bulge makes at the contact line relative to the $x-y$ plane, as defined in Fig. 1(a).

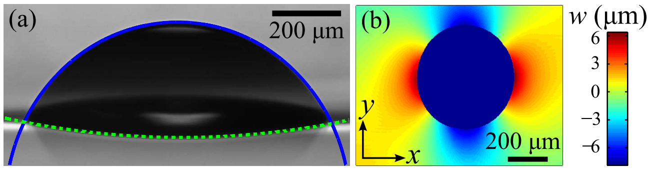

FIG. 2. (a) Optical side view taken from the x direction. The solid curve is a circular fit to the liquid-air interface, and the dashed curve is a parabolic fit to the bulge. (b) Optical profilometry scan taken from above the droplet depicting the z displacement w of the film surrounding the wetting region (dark elliptical area).

We describe our films as membranes where bending can be ignored, and, hence, the membrane slope is thought of as being discontinuous at the contact line. In reality, there exists a narrow region near the contact line where bending dominates and the membrane curves to connect the bulge region to the outside region. However, since this bending region is too small to be measured in our experiments, the membrane description is appropriate. For droplets on membranes with isotropic tension, the film is flat outside the contact region, and the contact line shape is completely determined by θ_d and θ_b [28–31]. However, for films with anisotropic tension, the film experiences an out-of-plane deformation outside the wetting region. Therefore, a complete picture of the contact line profile must include the angle of the membrane relative to the $x-y$ plane at the contact line which we denote with θ_m. As can be seen in Fig. 1(a), the membrane curves down towards the droplet in the y direction, which we define to correspond to $\theta_m > 0$. Conversely, the film curves up towards the droplet in the x direction and $\theta_m < 0$. Since $|\theta_m|$ is small ($< 4°$) and the membrane is difficult to resolve optically, we employ optical profilometry (Veeco, Wyko NT1100) to probe the out-of-plane deformation of the membrane, w, where $w > 0$ is defined to indicate the side from which the liquid droplet is placed. One such profilometry scan taken from the droplet side is shown in Fig. 2(b). The membrane is pulled towards positive w on the low tension side while being displaced towards negative w on the high tension side. From the profilometry data, it is straightforward to determine the values of θ_m in the two principal directions: x and y.

Although the tension in the membrane is not known *a priori*, it may be determined using the contact line profile, as has been demonstrated in previous studies [28–31]. Through a Neumann construction, as depicted in Fig. 1(a), where T_{in} and $T_{\text{out}} = T_{\text{in}} + \gamma \cos\theta_Y$ contain mechanical and interfacial tensions (see Ref. [31]), the contact line profile in a given direction is completely determined by the values of T_{in}/γ and θ_Y. The contact line profile is entirely

TABLE I. Sample fit of contact angle data in the x direction to a Neumann construction to extract $T_{\mathrm{in},x}/\gamma = 2.7 \pm 0.15$.

	Experiment	Best fit
$(\theta_{d,x} + \theta_{m,x})$	$57.8 \pm 1.2°$	$59.5 \pm 0.6°$
$(\theta_{d,x} + \theta_{b,x})$	$76.6 \pm 1.1°$	$78.1 \pm 0.6°$
$(\theta_{b,x} - \theta_{m,x})$	$18.8 \pm 0.8°$	$18.7 \pm 1.1°$

characterized by the three internal angles subtended at the contact line: $\pi - \theta_d - \theta_m$, $\theta_d + \theta_b$, and $\pi - \theta_b + \theta_m$. The Neumann construction is able to predict only these internal angles, *not* θ_d, θ_b, and θ_m individually. Therefore, using the value for θ_Y and the angles θ_d, θ_b, and θ_m, we fit the internal angles to the Neumann construction prediction in x and y with $T_{\mathrm{in},x}/\gamma$ and $T_{\mathrm{in},y}/\gamma$ as the fitting parameters (see Ref. [32]). The best fit allows us to extract values of $T_{\mathrm{in},x}/\gamma$ and $T_{\mathrm{in},y}/\gamma$. A sample fit is provided in Table 1, where it is clear that a single value of $T_{\mathrm{in},x}/\gamma$ captures the data well. The tensions measured in this way were found to be consistent with tensions computed from the strains in the film during stretching, attained using particle tracking in a separate experiment [32].

We now turn to theoretical considerations and begin with some simplifications to render the problem more tractable. First, we restrict our analysis to the case in which ϵ is close to unity, where the shape of the droplet may be treated as a perturbation to a spherical cap. As such, we make the assumption that the liquid-air interface profile as viewed along a general sight line oriented at ϕ [Fig. 1(b)] is simply a circular cap with its own radius of curvature. This assumption is validated by the fact that such profiles are well fitted to circular caps [32]. Similarly, as will be justified later, all profiles of the bulge are parabolic in a good approximation. We make the simplistic assumption that the deformations produced by the two droplets on the film are perturbative only to the pretension. This assumption was found to be valid in a previous study done with isotropic tension [31] but is further supported by the fact that the contact angles are unchanged as additional droplets are placed onto the film as well as by the tension measurement done using particle tracking [32]. Finally, we make small angle approximations when appropriate [37]. To predict the shape of the droplet's footprint, i.e., projection of the wetted region onto the $x-y$ plane, we make use of the fact that the total height from the bottom of the bulge to the top of the droplet must be equal in every profile. We find that the contact radius r_ϕ [defined in Fig. 1(b)] of the footprint is given by (see Ref. [32])

$$r_\phi \left[\arccos\left(\cos\theta_Y - \frac{\gamma}{2T_{\mathrm{in},\phi}}\sin^2\theta_Y\right)\right] = C, \qquad (1)$$

where $T_{\mathrm{in},\phi}$ is the total (mechanical and interfacial) tension in the ϕ direction in the region under the droplet and C is a constant which simply sets the overall length scale. We see that r_ϕ increases with $T_{\mathrm{in},\phi}$, consistent with the observation that droplets are elongated along the direction of highest tension. Since the membrane tensions are assumed to be unchanged by the addition of droplets, the tension remains purely biaxial with its principal axes aligned along x and y, and $T_{\mathrm{in},\phi} = T_{\mathrm{in},x}\cos^2\phi + T_{\mathrm{in},y}\sin^2\phi$ [38]. In Fig. 3(a), we show an optical top view of an elongated droplet on a film, where we also plot Eq. (1) as a solid curve with $C = 514\ \mu$m found by fitting. We see that Eq. (1) provides an excellent approximation of the elongated shape of the footprint. Furthermore, Eq. (1) can be used to determine ϵ without any free parameters. We see that the aspect ratio is high when $T_{\mathrm{in},y}$ is large while retaining a small $T_{\mathrm{in},x}$. For a quantitative comparison with our experimental observations, we refer to Fig. 3(b), where all measurements of the aspect ratio ϵ_{exp} are plotted against their predicted values ϵ_{th}, computed using Eq. (1) and the measured values of $T_{\mathrm{in},x}/\gamma$ and $T_{\mathrm{in},y}/\gamma$. We find a good agreement between the experimental and theoretical values of ϵ. We note that ϵ_{th} is systematically smaller than ϵ_{exp}, which we attribute to the simplifications made in the theory.

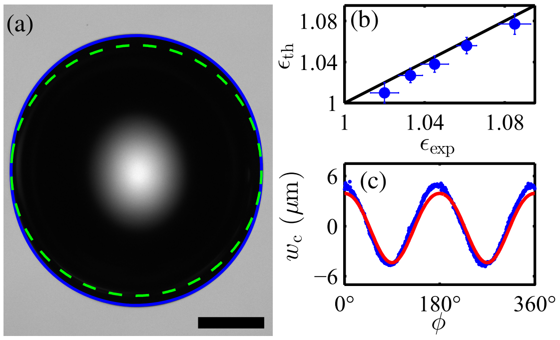

FIG. 3. (a) Top view image of an elongated droplet ($\epsilon \sim 1.09$) where the solid curve represents the best fit of Eq. (1) and the dashed curve is a circle drawn for comparison. Scale bar = 200 μm. (b) A comparison between the experimental and theoretical values of ϵ for all samples. The line drawn represents $\epsilon_{\mathrm{th}} = \epsilon_{\mathrm{exp}}$. (c) Vertical position of the contact line around a sample droplet, where the points correspond to experimental data and the solid curve is calculated from Eqs. (1) and (3) with A and B obtained from bulge profile fits.

To construct a full theoretical treatment of the membrane deformation, one may follow the approach laid out in articles by Davidovitch and co-workers, where the Föppl–von Kármán equations are solved in the limit of negligible bending contributions [7,8,39]. However, further simplifications can be made when the deformation of the membrane by the droplet does not notably modify the pre-existing tension. Justified by our experimental observations, we have already made this assumption (in the claim that $T_{\mathrm{in},\phi}$ remains biaxial) to simplify the description of our system. As such, the deflection of a membrane (w) carrying a uniform biaxial tension of $T_{\mathrm{in},x}$, $T_{\mathrm{in},y}$ is given by [32,40]

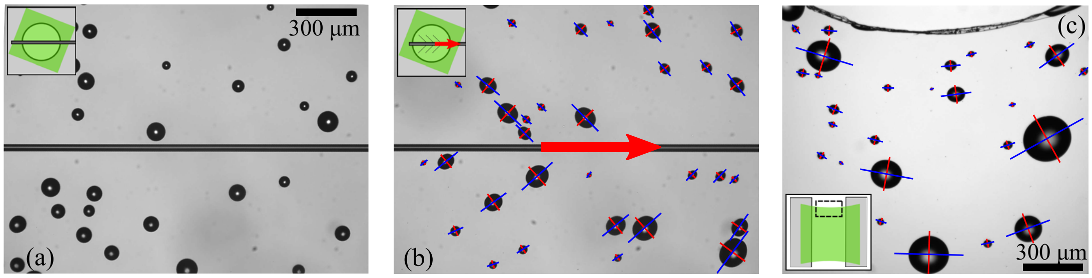

FIG. 4. (a) Droplets on a film with isotropic tension with a pipette laid across the film (schematized in the inset). (b) The pipette is moved in the direction indicated by the arrow to shear the film (schematized in the inset, where the thin diagonal lines indicate the principal direction of high tension). (c) Droplets deposited near the boundary (see the inset) of a film. The major (minor) axis of the droplets are indicated by a long (short) line in (b) and (c).

$$T_{\mathrm{in},x}\frac{\partial^2 w}{\partial x^2}+T_{\mathrm{in},y}\frac{\partial^2 w}{\partial y^2}=-p(x,y), \tag{2}$$

where p is the pressure distribution acting on the film. This equation is essentially Laplace's law but with anisotropic tension and in the limit of small membrane slopes. The small slope approximation is appropriate in this case, since the bulge contact angles are always below 25°. From this equation, it is straightforward to solve for the shape of the bulge, which forms in response to the uniform Laplace pressure over the wetted region. We propose a solution of the form

$$w=Ax^2+By^2+w_0, \tag{3}$$

where w_0 is an arbitrary vertical shift and A and B are found experimentally [32]. Thus, any vertical cross section of the bulge passing through its apex is simply a parabola, which is the reason for fitting the bulge profiles with parabolas to extract $\theta_{b,x}$ and $\theta_{b,y}$. From these parabolic fits, the values of A and B are determined. Of course, we must still ensure Eq. (2) is satisfied. Substituting w back into Eq. (2) generates a criterion which can be written as [32]

$$\frac{T_{\mathrm{in},x}}{\gamma}\theta_{b,x}+\frac{T_{\mathrm{in},y}}{\gamma\epsilon}\theta_{b,y}=\sin\theta_{d,x}+\frac{1}{\epsilon}\sin\theta_{d,y}. \tag{4}$$

Evaluating both sides of Eq. (4) using all our data yields a constant value of 1.75 ± 0.03 for the left side and 1.70 ± 0.06 for the right side, indicating that the data and theory are consistent.

A striking aspect of the system is the out-of-plane deformation of the membrane surrounding the wetting region, as evidenced in Fig. 2(b). As shown for a sample droplet in Fig. 3(c), the vertical position w_c of the contact line relative to its average value oscillates with ϕ. Knowing all parameters in Eqs. (1) and (3), we may attain a prediction for w_c by evaluating Eq. (3) at the position of the contact line given by Eq. (1). Therefore, we plot the prediction of the data in Fig. 3(c) with a solid curve and find that it exhibits excellent agreement with the data.

As we have seen, droplets are elongated along the high tension direction; i.e., the major and minor axes of the droplets' footprints align with the principal tension directions in the membrane [38]. We can further test this property by a separate experiment where samples are made with different stress fields in which the principal directions are known. As shown in Fig. 4(a), water droplets have been sprayed onto a freestanding elastomeric film on a circular washer, where the tension is completely isotropic and uniform. A thin glass pipette has then been placed into contact across the film but does not significantly modify the film's stresses. As such, the droplets are completely round, in agreement with previous work done with isotropic tension [31]. After these droplets have evaporated, we displace the pipette slightly towards the right, as seen in Fig. 4(b), which generates a shear stress in the membrane. If a membrane with isotropic stress is subjected to a shear stress τ_{xy}, the principal directions of the stress are aligned at 45° to the x and y axes regardless of the shear's magnitude [38]. To employ this known stress field as a test, we spray water droplets onto the film and fit the footprints of these with ellipses to extract the major (minor) axis, which is displayed in Figs. 4(b), 4(c) as a long (short) line. Computing the average angle that the major axes subtend to the pipette, we find $44\pm8°$, as we would expect. Finally, at a free (i.e., stress-free) boundary, the principal directions are tangent (high tension) and normal (low tension) to the boundary [38]. We thus purposely deposit liquid droplets near the bowed edges [see Fig. 1(b)] of our stretched sample, as seen in Fig. 4(c). Indeed, the major and minor axes plotted atop the droplets align with the principal directions. Note that, although we do not observe any mutual influence between droplets, we expect such an effect to become important at sufficiently small separations.

In this work, the droplets' elongated shape stems from the anisotropy in the compliance of the freestanding film in the two orthogonal directions. On the other hand, it is known that droplets atop stretched substrates which are noncompliant in the out-of-plane direction may also experience anisotropic wetting conditions and become elongated [41–43]. This is a result of two effects: anisotropic molecular forces or compositions caused by stretching the molecules at the surface [41,42] or an induced anisotropy in the topographical roughness [43,44]. These effects do not contribute to the results within our study, since droplets are round when placed atop stretched films which have been transferred onto a rigid substrate.

We have performed experiments studying liquid droplets atop deformable membranes which carry an anisotropic tension. Droplets assume shapes which deviate from spherical caps and become elongated along the direction of highest tension. By measuring the contact line profile, we completely determine the tensions in the membrane. Using these tensions, along with a minimal theoretical model, we are able to form accurate predictions for the elongated shape of the droplet's footprint and the out-of-plane deformation of the membrane surrounding this region. Thus, liquid droplets may be used as a tool to map out the magnitudes and directions of the stresses in a membrane—analogous to iron filings in magnetic fields.

The financial support by Natural Science and Engineering Research Council of Canada and the Global Station for Soft Matter, a project of Global Institution for Collaborative Research and Education at Hokkaido University, is gratefully acknowledged.

---

[*] dalnoki@mcmaster.ca

[1] C. Py, P. Reverdy, L. Doppler, J. Bico, B. Roman, and C. N. Baroud, Phys. Rev. Lett. **98**, 156103 (2007).

[2] N. Patra, B. Wang, and P. Král, Nano Lett. **9**, 3766 (2009).

[3] J. van Honschoten, J. Berenschot, T. Ondarcuhu, R. Sanders, J. Sundaram, M. Elwenspoek, and N. Tas, Appl. Phys. Lett. **97**, 014103 (2010).

[4] J. Bae, T. Ouchi, and R. C. Hayward, ACS Appl. Mater. Interfaces **7**, 14734 (2015).

[5] J. Huang, M. Juszkiewicz, W. H. de Jeu, E. Cerda, T. Emrick, N. Menon, and T. P. Russell, Science **317**, 650 (2007).

[6] D. Vella, M. Adda-Bedia, and E. Cerda, Soft Matter **6**, 5778 (2010).

[7] H. King, R. D. Schroll, B. Davidovitch, and N. Menon, Proc. Natl. Acad. Sci. U.S.A. **109**, 9716 (2012).

[8] R. D. Schroll, M. Adda-Bedia, E. Cerda, J. Huang, N. Menon, T. P. Russell, K. B. Toga, D. Vella, and B. Davidovitch, Phys. Rev. Lett. **111**, 014301 (2013).

[9] B. Andreotti, O. Baumchen, F. Boulogne, K. E. Daniels, E. R. Dufresne, H. Perrin, T. Salez, J. H. Snoeijer, and R. W. Style, Soft Matter **12**, 2993 (2016).

[10] B. Roman and J. Bico, J. Phys. Condens. Matter **22**, 493101 (2010).

[11] M. Rivetti and S. Neukirch, Proc. R. Soc. A **468**, 1304 (2012).

[12] A. Fargette, S. Neukirch, and A. Antkowiak, Phys. Rev. Lett. **112**, 137802 (2014).

[13] H. Elettro, F. Vollrath, A. Antkowiak, and S. Neukirch, Int. J. Nonlinear Mech. **75**, 59 (2015).

[14] A. Sauret, F. Boulogne, K. Somszor, E. Dressaire, and H. A. Stone, Soft Matter **13**, 134 (2017).

[15] H. Elettro, S. Neukirch, F. Vollrath, and A. Antkowiak, Proc. Natl. Acad. Sci. U.S.A. **113**, 6143 (2016).

[16] R. D. Schulman, A. Porat, K. Charlesworth, A. Fortais, T. Salez, E. Raphaël, and K. Dalnoki-Veress, Soft Matter **13**, 720 (2017).

[17] R. W. Style *et al.*, Proc. Natl. Acad. Sci. U.S.A. **110**, 12541 (2013).

[18] S. Karpitschka, A. Pandey, L. A. Lubbers, J. H. Weijs, L. Botto, S. Das, B. Andreotti, and J. H. Snoeijer, Proc. Natl. Acad. Sci. U.S.A. **113**, 7403 (2016).

[19] T. Liu, X. Xu, N. K. Nadermann, Z. He, A. Jagota, and C.-Y. Hui, Langmuir **33**, 75 (2017).

[20] R. Pericet-Cámara, A. Best, H. J. Butt, and E. Bonaccurso, Langmuir **24**, 10565 (2008).

[21] E. R. Jerison, Y. Xu, L. A. Wilen, and E. R. Dufresne, Phys. Rev. Lett. **106**, 186103 (2011).

[22] R. W. Style and E. R. Dufresne, Soft Matter **8**, 7177 (2012).

[23] R. W. Style, R. Boltyanskiy, Y. Che, J. S. Wettlaufer, L. A. Wilen, and E. R. Dufresne, Phys. Rev. Lett. **110**, 066103 (2013).

[24] A. Marchand, S. Das, J. H. Snoeijer, and B. Andreotti, Phys. Rev. Lett. **109**, 236101 (2012).

[25] S. J. Park, B. M. Weon, J. S. Lee, J. Lee, J. Kim, and J. H. Je, Nat. Commun. **5**, 4369 (2014).

[26] C.-Y. Hui and A. Jagota, Proc. R. Soc. A **470** (2014).

[27] M. E. Shanahan, J. Adhes. **18**, 247 (1985).

[28] N. Nadermann, C.-Y. Hui, and A. Jagota, Proc. Natl. Acad. Sci. U.S.A. **110**, 10541 (2013).

[29] C.-Y. Hui, A. Jagota, N. Nadermann, and X. Xu, Procedia IUTAM **12**, 116 (2015).

[30] C.-Y. Hui and A. Jagota, Soft Matter **11**, 8960 (2015).

[31] R. D. Schulman and K. Dalnoki-Veress, Phys. Rev. Lett. **115**, 206101 (2015).

[32] See Supplemental Material at http://link.aps.org/supplemental/10.1103/PhysRevLett.118.198002 for a more detailed overview of the sample preparation, optical profiles of a droplet and bulge viewed along the y direction, an explanation of the particle tracking experiment to verify measured tensions, the theoretical arguments leading to Eqs. (1), (3), and (4), the Neumann construction used in the fits, and Refs. [33–36].

[33] R. Pan and D. Wati, Polymer Composites **17**, 486 (1996).

[34] P. Russo, M. Lavorgna, F. Piscitelli, D. Acierno, and L. Di Maio, Eur. Polym. J. **49**, 379 (2013).

[35] H.-Y. Mi, X. Jing, M. R. Salick, W. C. Crone, X.-F. Peng, and L.-S. Turng, Adv. Polym. Tech. **33**, 21380 (2014).

[36] D. R. Lide, *CRC Handbook of Chemistry and Physics* (CRC Press, Boca Raton, FL, 2004), pp. 6–154.

[37] In the theoretical model and we make the approximation that $\tan\theta_b \approx \theta_b$ and $\tan\theta_d/2 \approx \theta_d/2$. In our experiments, $\theta_b < 25°$ and $\theta_d/2 < 33°$, so there is less than ~10% error in making these approximations.

[38] S. Timoshenko and J. Goodier, *Theory of Elasticity*, 2nd ed. (McGraw-Hill, New York, 1951).

[39] B. Davidovitch, R. D. Schroll, D. Vella, M. Adda-Bedia, and E. A. Cerda, Proc. Natl. Acad. Sci. U.S.A. **108**, 18227 (2011).

[40] L. Landau and E. Lifshitz, *Theory of Elasticity*, 3rd ed. (Butterworth-Heinemann, New York, 1986).

[41] R. J. Good, J. A. Kvikstad, and W. O. Bailey, J. Colloid Interface Sci. **35**, 314 (1971).

[42] E. H. Cirlin and D. H. Kaelble, J. Polym. Sci., Polym. Phys. Ed. **11**, 785 (1973).

[43] N. Sung, H. Lee, P. Yuan, and C. Sung, Polym. Eng. Sci. **29**, 791 (1989).

[44] H. Schonhorn, J. Adhes. **23**, 147 (1987).

Supplemental Information for: "Liquid droplets act as "compass needles" for the stresses in a deformable membrane"

Rafael D. Schulman,[1] René Ledesma-Alonso,[2,3] Thomas Salez,[3,4] Elie Raphaël,[3] and Kari Dalnoki-Veress[1,3,*]

[1]*Department of Physics and Astronomy, McMaster University,*
1280 Main St. W, Hamilton, ON, L8S 4M1, Canada.
[2]*CONACYT - Universidad de Quintana Roo, Boulevar Bahía s/n, Chetumal, 77019 Quintana Roo, México*
[3]*Laboratoire de Physico-Chimie Théorique, UMR CNRS Gulliver 7083,*
ESPCI Paris, PSL Research University, 75005 Paris, France.
[4]*Global Station for Soft Matter, Global Institution for Collaborative Research and Education,*
Hokkaido University, Sapporo, Hokkaido 060-0808, Japan.

(Dated: April 6, 2017)

SAMPLE PREPARATION

Elastomeric films were prepared from Elastollan TPU 1185A (BASF). Solutions of Elastollan in cyclohexanone (Sigma-Aldrich) were prepared at 3% weight fraction. Upon spincoating these solutions, the Elastollan polymers, which contain hard and soft segments, assemble to form an elastomer with physical crosslinks. The Elastollan solutions were cast onto freshly cleaved mica substrates (Ted Pella Inc.) to produce highly uniform (<5% variation) films with of thickness $h \sim 240$ nm, measured using ellipsometry (Accurion, EP3). These films were subsequently heated at 100°C for 90 min to remove any residual solvent from the elastomer. After annealing, these films were floated onto the surface of an ultrapure water bath (18.2 MΩ·cm, Pall, Cascada, LS) and picked up between two supports to form our sample. In our experiments, the liquid we use is glycerol (Caledon Laboratories Ltd.).

LIQUID CAP AND BULGE PROFILES

As explained in the main text, two droplets are placed on the film: one on each side. The purpose of doing so is to be able to visualize both the liquid-air interface and the bulge when viewing the sample from the y-direction, where the supports obscure our view of the lower side of the film. Sample optical microscopy images of the two profiles when viewed from the y-direction are shown in Fig. S1. In Fig. S1(a), the solid curve represents the best fit of a circular cap to the liquid-air interface profile, and in Fig. S1(b), the dashed curve represents the best fit of a parabola to the bulge profile. The fits describe the optical profiles well.

From optical profilometry, we find that the film is always pulled up towards the droplet on the low-tension side. This is seen in Fig.2(b) of the main text, where we observe a positive w on the sides of the droplet along the x-direction. In fact, this small deformation can be visualized in Fig. S1, where the film is seen to be pulled up towards the droplet in (a) and suppressed leading into the bulge in (b).

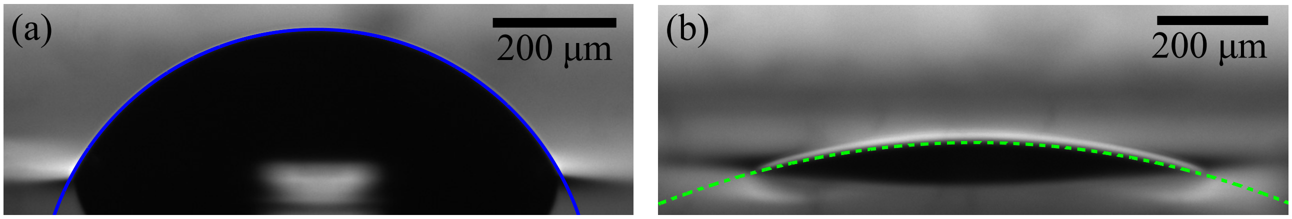

FIG. S1. (a) An optical sideview of a liquid-air interface profile taken from the y-direction, where the solid curve represents the circular cap fit to the profile. (b) An optical sideview of a bulge as seen from the y-direction. The dashed curve corresponds to the parabolic fit to the profile.

As mentioned in the main text, to derive Eq. 1, we assume that the liquid-air interface profile is well described by a circular cap when viewed along any general direction oriented at ϕ to the x-axis. Experimentally, we observe that this assumption is fully reasonable. In Fig. S2, we show a sample profile of a liquid-air interface taken along a sightline corresponding to $\phi = 45°$, where we show the circular fit as a solid curve. As can be seen from this image, as well as any other sightline we have tested, the profile is always well described by a circular cap. Of course, since

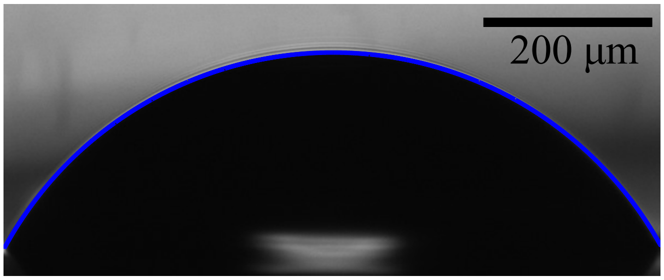

FIG. S2. An optical sideview of the liquid-air interface taken from a sightline oriented at $\phi = 45^\circ$ to the x-axis. The solid curve represents the circular fit to the profile.

the 3D shape of the liquid-air interface is not spherical, the radius of curvature of the circular cap extracted from the profile fits changes along the various sightlines.

TENSION VERIFICATION

Although the technique of using liquid contact angles to measure the tension in deformable membranes has been employed and verified in previous studies [1, 2], we perform an additional validation here. In this experiment, we prepare a film where the tension is isotropic (droplets are completely round within experimental error) and is measured to be $T_{\text{in}}/\gamma = 2.1 \pm 0.1$ using the contact angle technique from the main manuscript. Near the center of the film, we place small dirt particles to act as tracer particles. Next, we stretch the film along the y-axis, and from the tracer particles, the strains induced in the film in both directions are measured to be $e_x = -0.016 \pm 0.006$ and $e_y = 0.195 \pm 0.015$. Next, we perform contact angle measurements once again to determine the tension in this way. We find the change in tension from the initial state to be $\Delta T_{\text{in},y}/\gamma = 6.6 \pm 0.8$ and $\Delta T_{\text{in},x}/\gamma = 2.3 \pm 0.3$. If we suppose the interfacial tensions do not change appreciably upon stretching, the change in tension is purely mechanical.

To derive a theoretical expression for the change in tension upon straining the film, we employ Hooke's law [3]. We assume that there is no stress acting in the z-direction across the film, i.e. $\sigma_z = 0$. We also know that the mechnical tension is related to stress through film thickness $\Delta T = h\Delta\sigma$. Once again, the Δ signifies changes from the reference state of isotropic tension. As such, we may derive simple expressions for the changes in mechanical tension upon stretching:

$$\Delta T_x = \frac{Eh(e_x + \nu e_y)}{1 - \nu^2}, \tag{S1}$$

$$\Delta T_y = \frac{Eh(e_y + \nu e_x)}{1 - \nu^2}, \tag{S2}$$

where ν is the Poisson ratio of the elastomer, which can be assumed to be 0.5 and E is the Young's modulus. Some other quantities of interest to compute are the tension ratio

$$(\Delta T_y/\Delta T_x) = \frac{e_y + \nu e_x}{e_x + \nu e_y}, \tag{S3}$$

since this quantity is independent of the modulus and film thickness, as well as the strain in the vertical direction, representing the fractional change in film thickness upon straining

$$e_z = \frac{\nu}{\nu - 1}(e_x + e_y). \tag{S4}$$

Substituting our measured strain values for the strains into Eq. S3, we find $(\Delta T_y/\Delta T_x) = 2.3 \pm 0.1$. This value is in agreement with the value measured using contact angles $(\Delta T_{\text{in},y}/\Delta T_{\text{in},x}) = 2.9 \pm 0.5$ within experimental error. In addition, as a consistency check, we verify Eq. S4 by measuring the film thickness before and after stretching, to find a change in film thickness of -18.3%, which agrees nicely with the predicted strain of -17.9% from Eq. S4.

To compare the individual values of the tension from contact angles against those from particle tracking, we must know E and γ. We may find values for E in the literature; nevertheless, this introduces error, as E will depend on the details of the sample preparation for a physically cross-linked elastomer. With this caveat in place, we find measured literature values for the Young's modulus of Elastollan be roughly within the range $E = 9 \pm 1.5$ MPa [4–6]. The surface tension of glycerol is $\gamma = 0.063$ N/m [7]. For h in Eqs. S1 and S2, we use the stretched film thickness. As such, our predicted values from particle tracking are $\Delta T_x/\gamma = 3.1 \pm 0.9$ and $\Delta T_y/\gamma = 7 \pm 2$, which compare well with the tensions determined from contact angles.

SHAPE OF THE WETTING REGION PERIMETER

In this section, we outline the arguments used to attain Eq. 1 in the main manuscript. We make some simplifying assumptions to render the problem more tractable. First and foremost, we assume that the shape of the liquid-air interface is a perturbation from a spherical cap. Given this assumption, there are two reasonable approximations which can be made. First, we approximate that any vertical cross-section of the liquid-air interface done along a general line oriented at ϕ (see Fig. 1(b) in the main manuscript) is a circular cap with its own radius of curvature. This assumption is found to be in agreement with the experimental observation that sideview profiles of the liquid-air interface from any such sightlines are well-described by circular caps (example seen in Fig. S2). From the elliptical paraboloid shape of the bulge, which will be discussed in the following section, we know that all cross-sections of the bulge done in the same way are parabolas. Next, if we define ϕ' to be the angle subtended between the x-axis and the in-plane normal of the footprint perimeter, we make the approximation that $\phi' \approx \phi$. Of course, true equality only holds in the limit that the footprint shape is circular ($\epsilon = 1$), but it remains a good approximation for ϵ close to 1.

To begin the derivation, we point out that the vertical distance from the apex of the bulge to the top of the droplet, h_{tot}, must be the same for any profile taken from a cross-section along a line oriented at ϕ. For a given ϕ, this height is found as the sum of the liquid cap height $h_{\mathrm{d},\phi}$ and the bulge height $h_{\mathrm{b},\phi}$. The height of the liquid cap can be found through a simple circular cap identity $h_{\mathrm{d},\phi} = r_\phi \tan\theta_{\mathrm{d},\phi}/2$, where r_ϕ is the footprint radius and $\theta_{\mathrm{d},\phi}$ is the cap's contact angle, both for this value of ϕ. A similar relationship can be found for the parabola which represents the bulge, $h_{\mathrm{b},\phi} = \frac{r_\phi}{2}\tan\theta_{\mathrm{b},\phi}$. Therefore, we can write

$$h_{\mathrm{tot}} = r_\phi\Big(\frac{1}{2}\tan\theta_{\mathrm{b},\phi} + \tan\frac{\theta_{\mathrm{d},\phi}}{2}\Big). \tag{S5}$$

Our final simplification in this derivation is to assume that θ_{b} and $\theta_{\mathrm{d}}/2$ are small angles, such that $\tan\theta_{\mathrm{b}} \approx \theta_{\mathrm{b}}$ and $\tan\theta_{\mathrm{d}}/2 \approx \theta_{\mathrm{d}}/2$. This approximation is reasonable for our experiments where $\theta_{\mathrm{b},\phi} < 25°$ and $\theta_{\mathrm{d},\phi}/2 < 33°$, so there is less than 11% error in making this approximation at this point. Generally these assumptions become increasingly more appropriate the smaller θ_{Y} is. Employing the small-angle limit, we are left with

$$h_{\mathrm{tot}} = \frac{r_\phi}{2}\Big(\theta_{\mathrm{b},\phi} + \theta_{\mathrm{d},\phi}\Big). \tag{S6}$$

The angle sum $\theta_{\mathrm{b},\phi} + \theta_{\mathrm{d},\phi}$ represents the internal angle of the liquid at the contact line, and can be simply predicted using a Neumann construction, as was shown in previous work [2].

$$\theta_{\mathrm{b},\phi} + \theta_{\mathrm{d},\phi} = \arccos\Big(\cos\theta_{\mathrm{Y}} - \frac{\gamma}{2T_{\mathrm{in},\phi}}\sin^2\theta_{\mathrm{Y}}\Big). \tag{S7}$$

This Neumann construction should be set up normal to the contact line. However, since $\phi' \neq \phi$ as outlined before, the normal line does not pass through the droplet center. Therefore, to simplify the problem, we assume that $\phi' \approx \phi$, which implies that the Neumann construction above represents the internal angle of the liquid for a cross-section taken from the contact line to the droplet center, oriented at an angle ϕ to the x-axis. Thus, noting that h_{tot} in Eq. S6 is just some constant value, we arrive at the final result

$$r_\phi = \frac{C}{\arccos\Big(\cos\theta_{\mathrm{Y}} - \frac{\gamma}{2T_{\mathrm{in},\phi}}\sin^2\theta_{\mathrm{Y}}\Big)}, \tag{S8}$$

where $T_{\mathrm{in},\phi}$ is the total tension in the ϕ direction in the region under the droplet, and C is a constant which simply sets the overall scale of the region. As discussed in the main text, we assume that the deformations produced by the two liquid drops on the film are only perturbative to the pre-tension of the membrane. This assumption was validated in previous study done with isotropic tension [2], but is further supported by the experimental observation that the contact angles remain constant as additional droplets are placed onto the film and also by the tension confirmation using tracer particles described in the previous section. Since we have prepared the film to have a biaxial tension with principal directions in x and y, the tension in any direction ϕ is $T_{\mathrm{in},\phi} = T_{\mathrm{in},x}\cos^2\phi + T_{\mathrm{in},y}\sin^2\phi$ [3].

DERIVATION OF THE BULGE SHAPE

The small-slope out-of-plane deformation of a film $w\left(x,y\right)$ subjected to a transverse pressure is described by the Föppl-von Kármán equations [8]:

$$D\Delta^2 w - h\nabla\cdot\left(\sigma\cdot\nabla w\right) \; = p, \tag{S9a}$$

$$\nabla\cdot\sigma = 0 \ , \tag{S9b}$$

where p is the transverse pressure distribution, D is the flexural rigidity, h is the film thickness, and σ is the stress tensor. In our system, bending can be neglected, and the first term in Eq. S9a can be ignored. Motivated by experimental observations, we make the simplifying assumption that the deformation of the membrane by the droplet does not notably modify the pre-existing tension. Therefore, the stress in the membrane is the as-prepared biaxial stress which is uniform in the region near the center of the film where the experiment is performed. Since the stress is uniform, Eq. S9b is automatically satisfied, and Eq. S9a can be simplified to:

$$T_{\mathrm{in},x}\frac{\partial^2 w}{\partial x^2} + 2T_{\mathrm{in},xy}\frac{\partial^2 w}{\partial x\partial y} + T_{\mathrm{in},y}\frac{\partial^2 w}{\partial y^2} = -p, \tag{S10}$$

where we have used the general relation that tension is stress multiplied by film thickness. Since the film is prepared with a biaxial tension in which the principal directions are aligned with x and y, it implies that $T_{\mathrm{in},xy} = 0$, thus we are left with

$$T_{\mathrm{in},x}\frac{\partial^2 w}{\partial x^2} + T_{\mathrm{in},y}\frac{\partial^2 w}{\partial y^2} = -p\left(x,y\right) \ , \tag{S11}$$

Since there is no flow within the liquid, the droplet must contain a uniform pressure, so p is a constant value in our case and given by the Laplace pressure of the droplet $p = -\gamma\left(\frac{1}{R_{\mathrm{d},x}} + \frac{1}{R_{\mathrm{d},y}}\right)$, where the negative sign indicates that the pressure acts on the film in the negative z-direction. Note that Eq. S11 is simply the anisotropic Laplace's law in the limit of small slopes.

For the particular case in which $T_{\mathrm{in},x} = T_{\mathrm{in},y}$, we recover the isotropic Laplace's law (small slopes), for which the solution is given by

$$w\left(r\right) = \frac{pr^2}{4T_{\mathrm{in},x}} + c_0\ln(r) + c_1 \ , \tag{S12}$$

with $r = \sqrt{x^2+y^2}$. Since the position of the membrane at $x = y = 0$ must be finite, we find that $c_0 = 0$, whereas $c_1 = w_0$, an arbitrary vertical shift of the system. Therefore, the isotropic solution becomes

$$w\left(x,y\right) = \frac{p}{4T_{\mathrm{in},x}}\left(x^2+y^2\right) + w_0 \ , \tag{S13}$$

For the anisotropic case, since ϵ is near 1, we expect that the solution should be very similar to the isotropic case. Thus, we propose

$$w\left(x,y\right) = Ax^2 + By^2 + Cxy + Dx + Ey + F \ . \tag{S14}$$

In addition, we know that $\partial_x w = \partial_y w = 0$ at $x = y = 0$, which provides the values $D = 0$ and $E = 0$. Once more, at $x = y = 0$ an arbitrary vertical shift of the system w_0 is asigned to the coefficient F. Additionally, we must consider the symmetry conditions: 1) $\partial_x w = 0$ at $x = 0$; 2) $\partial_y w = 0$ at $y = 0$; both implying that $C = 0$.

Therefore, we have

$$w\left(x,y\right) = Ax^2 + By^2 + w_0 \ . \tag{S15}$$

Plugging this ansatz back into Eq. S11 leads to

$$2T_{\mathrm{in},x}A + 2T_{\mathrm{in},y}B = \gamma\Big(\frac{1}{R_{\mathrm{d},x}} + \frac{1}{R_{\mathrm{d},y}}\Big)\ . \tag{S16}$$

We can also write A and B in terms of $\theta_{\mathrm{b},x}$ and $\theta_{\mathrm{b},y}$. At $x = r_x$, $y = 0$ we have $\partial_x w = 2Ar_x = \tan\theta_{\mathrm{b},x} \approx \theta_{\mathrm{b},x}$. Similarly, $2Br_y \approx \theta_{\mathrm{b},y}$. In addition, a circular cap identity can be used to write $R_{\mathrm{d},x}$ and $R_{\mathrm{d},y}$ in terms of $\theta_{\mathrm{d},x}$ and $\theta_{\mathrm{d},y}$. Thus, Eq S16 becomes

$$\frac{T_{\mathrm{in},x}\theta_{\mathrm{b},x}}{r_x} + \frac{T_{\mathrm{in},y}\theta_{\mathrm{b},y}}{r_y} = \gamma\Big(\frac{\sin\theta_{\mathrm{d},x}}{r_x} + \frac{\sin\theta_{\mathrm{d},y}}{r_y}\Big)\ . \tag{S17}$$

Finally, we arrive at Eq. 4 in the main manuscript

$$\frac{T_{\mathrm{in},x}\theta_{\mathrm{b},x}}{\gamma} + \frac{T_{\mathrm{in},y}\theta_{\mathrm{b},y}}{\gamma\epsilon} = \sin\theta_{\mathrm{d},x} + \frac{1}{\epsilon}\sin\theta_{\mathrm{d},y}\ . \tag{S18}$$

NEUMANN CONSTRUCTION

The three internal angles characterizing the contact line profile are $\pi - \theta_{\mathrm{d}} - \theta_{\mathrm{m}}$, $\theta_{\mathrm{d}} + \theta_{\mathrm{b}}$, and $\pi - \theta_{\mathrm{b}} + \theta_{\mathrm{m}}$. Thus, the internal angles are set by three different linear combinations of the measured angles: $\theta_{\mathrm{d}} + \theta_{\mathrm{m}}$, $\theta_{\mathrm{d}} + \theta_{\mathrm{b}}$, and $\theta_{\mathrm{b}} - \theta_{\mathrm{m}}$. As was done in Ref. [2], one may apply a Neumann construction to attain predictions for these three angle combinations:

$$\cos\left(\theta_d + \theta_m\right) = \frac{\left[T_{out}/\gamma\right]^2 - \left[T_{in}/\gamma\right]^2 + 1}{2\left[T_{out}/\gamma\right]}, \tag{S19a}$$

$$\cos\left(\theta_b + \theta_d\right) = \frac{\left[T_{out}/\gamma\right]^2 - \left[T_{in}/\gamma\right]^2 - 1}{2\left[T_{in}/\gamma\right]}, \tag{S19b}$$

$$\cos\left(\theta_b - \theta_m\right) = \frac{\left[T_{out}/\gamma\right]^2 + \left[T_{in}/\gamma\right]^2 - 1}{2\left[T_{out}/\gamma\right]\left[T_{in}/\gamma\right]}, \tag{S19c}$$

where $T_{\mathrm{out}} = T_{\mathrm{in}} + \gamma\cos\theta_{\mathrm{Y}}$. These predictions depend only on two parameters: T_{in}/γ and θ_{Y}. Of course, this Neumann construction may be carried out normal to the contact line at any point along the perimeter. Thus, using the value we measure for θ_{Y}, we fit these predictions separately to the measured internal angles in x and in y to find the best fit parameter values of $T_{\mathrm{in},x}/\gamma$ and $T_{\mathrm{in},y}/\gamma$. The best fitted values of $\theta_{\mathrm{d}} + \theta_{\mathrm{m}}$, $\theta_{\mathrm{d}} + \theta_{\mathrm{b}}$, and $\theta_{\mathrm{b}} - \theta_{\mathrm{m}}$ are listed in Table I of the main manuscript.

---

[*] dalnoki@mcmaster.ca

[1] N. Nadermann, C.-Y. Hui, and A. Jagota, Proc. Natl. Acad. Sci. U.S.A. **110**, 10541 (2013).
[2] R. D. Schulman and K. Dalnoki-Veress, Phys. Rev. Lett. **115**, 206101 (2015).
[3] S. Timoshenko and J. Goodier, *Theory of Elasticity, 2nd* (McGraw-Hill Book Company, Inc., New York, 1951).
[4] R. Pan and D. Wati, Polym. Composite **17**, 486 (1996).
[5] P. Russo, M. Lavorgna, F. Piscitelli, D. Acierno, and L. Di Maio, Eur. Polym. J. **49**, 379 (2013).
[6] H.-Y. Mi, X. Jing, M. R. Salick, W. C. Crone, X.-F. Peng, and L.-S. Turng, Adv. Polym. Tech. **33** (2014).
[7] D. R. Lide, *CRC Handbook of Chemistry and Physics* (CRC Press, 2004) pp. 6–154.
[8] L. Landau and E. Lifshitz, *Theory of Elasticity, 3rd* (Butterworth-Heinemann, New York, 1986).

3.3 Paper III

Surface energy of strained amorphous solids

R. D. Schulman, M. Trejo, T. Salez, E. Raphaël and K. Dalnoki-Veress, Nat. Commun., **9**, 982 (2018).

In this study, we digress from examining elastocapillary deformations of elastic membranes to focus on the Shuttleworth effect. Since several of our studies employ strained elastomeric materials, it is of fundamental interest to address whether the interfacial energy of these materials changes with strain. Here, we extend our experiment to investigate polymeric glasses as well, since the Shuttleworth effect has not been studied for this class of materials.

To probe the Shuttleworth effect, we prepare thin glassy and elastomeric polymer films. The films are uniaxially strained with high precision using the apparatus depicted in Fig. 2.2(b), and then transferred onto a silicon substrate for measurement. The experiment consists of measuring Young's angle θ_{Y} on these strained films. Since $\gamma\cos\theta_{\mathrm{Y}} = \gamma_{\mathrm{sv}} - \gamma_{\mathrm{sl}}$, any changes in θ_{Y} implies changes in the interfacial energy difference $\gamma_{\mathrm{sv}} - \gamma_{\mathrm{sl}}$. The contact angle measurements are performed with two standard test liquids of known surface energy: glycerol and diiodomethane.

For the glassy polymers, polysulfone and polycarbonate are used since these have high elongations at yield. We find that $\gamma_{\mathrm{sv}} - \gamma_{\mathrm{sl}}$ decreases with strain for diiodomethane but observe a strong increase in $\gamma_{\mathrm{sv}} - \gamma_{\mathrm{sl}}$ with strain using glycerol. These results indicate, for the first time, that glassy polymer interfaces have strain-dependent surface energies, which implies that $\Upsilon_{AB} \neq \gamma_{AB}$ for interfaces involving these materials. In addition, the opposite behaviour for the two test liquids is attributed to be caused by differences in polarity: diiodomethane is non-polar whereas glycerol is highly polar. Since γ_{sl} quantifies intermolecular interactions between solid and liquid, it is not surprising that polarity of the liquid plays an important role.

A simple integration of dispersive (van der Waals) intermolecular interactions across the interface (Hamaker's calculation) shows that the quantity $\gamma_{\mathrm{sv}} - \gamma_{\mathrm{sl}}$ depends linearly on the density of the solid. Since the density of glassy solids decreases with strain ($\nu = 0.37$ for the materials chosen), it is expected that $\gamma_{\mathrm{sv}} - \gamma_{\mathrm{sl}}$ should also decrease with strain for the non-polar test liquid. We find that a model which incorporates only these density changes does not fully capture the magnitude of the trends we observe for diiodomethane, and implies that there are other effects at play as well, such as the polarizability of the molecules in the solid changing with strain. This model does not account for interactions involving permament dipoles, and thus should not be applied to data attained with the polar test liquid.

For the elastomers, two physically crosslinked elastomers (SIS and Elastollan) and one chemically crosslinked elastomer (polyvinyl siloxane) are used. Although the films are strained up to 100%, we find no change in θ_Y for any of these elastomers using two test liquids. This observation implies that $\frac{\mathrm{d}\gamma_\mathrm{sv}}{\mathrm{d}\epsilon} = \frac{\mathrm{d}\gamma_{\mathrm{sl}_1}}{\mathrm{d}\epsilon} = \frac{\mathrm{d}\gamma_{\mathrm{sl}_2}}{\mathrm{d}\epsilon}$, where 1 and 2 indicate two different test liquids. Since there is no reason to expect the solid-vapour surface energy to change at the same non-zero rate as the solid-liquid surface energy for an arbitrary choice of liquid, we suggest that $\frac{\mathrm{d}\gamma_\mathrm{sv}}{\mathrm{d}\epsilon} = \frac{\mathrm{d}\gamma_\mathrm{sl}}{\mathrm{d}\epsilon} = 0$ for interfaces involving elastomers - i.e. no Shuttleworth effect. In fact, elastomers are incompressible liquids ($\nu \approx 0.5$) which are constrained by crosslinks on length scales much larger than those relevant to intermolecular interactions. Thus, at the interface, we anticipate that elastomers maintain a constant molecular environment and density at the interface, much like a liquid, resulting in an unchanging surface energy with strain.

The idea for this project was conceived through discussion between Dr. Dalnoki-Veress, Dr. Raphaël and Dr. Salez on how to most directly address the Shuttleworth effect with an experiment. The experimental set-up was designed by Dr. Dalnoki-Veress and myself. In this study, I made the samples, performed the experiments, and analyzed the data. The theoretical work was a collaborative effort between Dr. Trejo and I, with important conceptual input from Dr. Dalnoki-Veress, Dr. Salez, and Dr. Raphaël. I wrote the first draft of the manuscript, which was then edited by all the other contributors.

nature COMMUNICATIONS

ARTICLE

DOI: 10.1038/s41467-018-03346-1 OPEN

Surface energy of strained amorphous solids

Rafael D. Schulman[1], Miguel Trejo[2], Thomas Salez[3,4], Elie Raphaël[2] & Kari Dalnoki-Veress[1,2]

Surface stress and surface energy are fundamental quantities which characterize the interface between two materials. Although these quantities are identical for interfaces involving only fluids, the Shuttleworth effect demonstrates that this is not the case for most interfaces involving solids, since their surface energies change with strain. Crystalline materials are known to have strain-dependent surface energies, but in amorphous materials, such as polymeric glasses and elastomers, the strain dependence is debated due to a dearth of direct measurements. Here, we utilize contact angle measurements on strained glassy and elastomeric solids to address this matter. We show conclusively that interfaces involving polymeric glasses exhibit strain-dependent surface energies, and give strong evidence for the absence of such a dependence for incompressible elastomers. The results provide fundamental insight into our understanding of the interfaces of amorphous solids and their interaction with contacting liquids.

---

[1] Department of Physics and Astronomy, McMaster University, 1280 Main Street West, Hamilton, ON L8S 4M1, Canada. [2] Laboratoire de Physico-Chimie Théorique, UMR CNRS Gulliver 7083, ESPCI Paris, PSL Research University, 75005 Paris, France. [3] Univ. Bordeaux, CNRS, LOMA, UMR 5798, 33405 Talence, France. [4] Global Station for Soft Matter, Global Institution for Collaborative Research and Education, Hokkaido University, Sapporo, Hokkaido 060-0808, Japan. Correspondence and requests for materials should be addressed to K.D-V. (email: dalnoki@mcmaster.ca)

The surface energy γ of an interface between two materials is the energetic cost associated with creating a unit of surface by cleaving and is associated with breaking intermolecular bonds, whereas the surface stress Υ characterizes the force required to generate a unit of area by deforming the materials and is associated with stretching the bonds of the molecules near the interface[1–5]. These separate quantities are related through the Shuttleworth equation[1], for which a simplified form is:

$$\Upsilon_{\mathrm{AB}}(\varepsilon) = \gamma_{\mathrm{AB}}(\varepsilon) + \frac{\mathrm{d}\gamma_{\mathrm{AB}}(\varepsilon)}{\mathrm{d}\varepsilon}, \qquad (1)$$

where ε is the strain parallel to the interface and the subscript refers to the interface between A and B. Although the validity of Eq. 1 is well established (see ref. [2] for a review), it is not obvious how the surface energy is dependent upon strain. For a liquid in contact with a vapour, the surface stress and energy are identical because as the liquid–vapour interface is deformed, molecules from the two fluids may simply rearrange themselves to maintain a constant average molecular environment at the interface. In contrast, as a crystalline solid is deformed, the surface density of atoms is altered, leading to a strain-dependent surface energy. Given Eq. 1, this strain dependence implies that the surface energy and surface stress are in general not equal for this class of materials. There has been some experimental work verifying this principle, but there is difficulty in performing absolute measurements which are precise and model independent[2,3,5–10]. Due to the periodic structure of crystals, rigorous theoretical calculations of surface energy and stress are tractable and have been carried out for a multitude of these materials[2,3,5,6].

On the other hand, there is little evidence to indicate whether the surface energies of interfaces involving amorphous materials, such as glasses and elastomers, are strain dependent. In fact, to the best of our knowledge, there has been no theoretical or experimental work investigating the Shuttleworth effect for glasses. Elastomers have recently received particular attention, because in these soft materials the surface stresses may induce large-scale deformations[11,12]. For instance, sufficiently soft cylindrical structures will undergo a Plateau–Rayleigh instability[13]. However, despite the multitude of recent studies, no consensus has been reached on whether interfaces involving elastomers have surface stresses which are different from surface energies[14–25]. This situation is likely rooted in the fact that interpretations of the experimental measurements to determine Υ have been model dependent.

In this study, by using contact angle measurements, we unambiguously quantify the strain dependence of the difference between the solid–liquid and solid–vapour surface energies of strained interfaces involving polymeric glassy and elastomeric materials. We employ Young–Dupré's law, which dictates that $\gamma_{\mathrm{lv}} \cos\theta_{\mathrm{Y}} = \gamma_{\mathrm{sv}} - \gamma_{\mathrm{sl}}$, where s, l, and v indicate the solid, liquid, and vapour phases and θ_{Y} is the contact angle at equilibrium. Since γ_{lv} is independent of any strain applied to the solid, θ_{Y} is a direct indicator of the strain-dependent difference between γ_{sv} and γ_{sl}. We found that interfaces involving polymeric glassy materials do exhibit strain-dependent surface energies. As seen in Fig. 1a, a droplet placed on a glassy substrate strained by only 6% exhibits a significant change in contact angle. In contrast, we provide strong evidence that interfaces involving an elastomer together with a liquid or a vapour have surface energies which are unchanged by strain. In Fig. 1b, an elastomeric substrate strained by 100% shows no measurable change in θ_{Y}. As we will show, θ_{Y} is independent of strain for all tested combinations of elastomer and liquid.

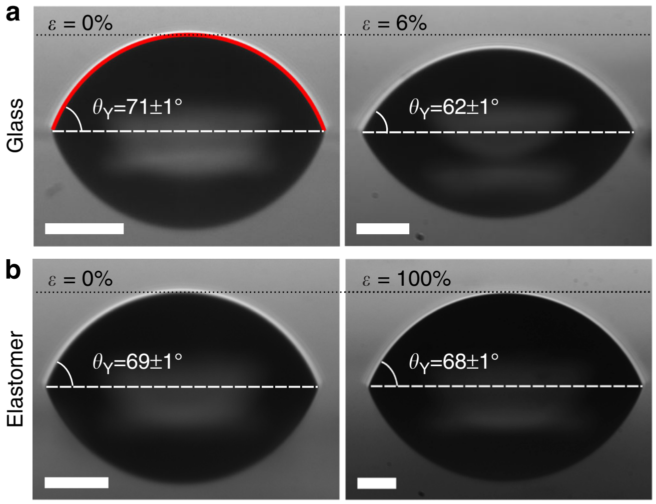

Fig. 1 Contact angle measurements on strained and unstrained polymeric substrates. **a** Contact angle measurements of glycerol on unstrained (left) and 6% strained (right) polycarbonate glass. The left panel shows a typical circular cap fit (red solid line) to the droplet profile. **b** Contact angle measurements of glycerol on unstrained (left) and 100% strained (right) Elastollan elastomer. The images are rescaled so that all contact radii appear equal, while preserving the aspect ratio. Since the profiles are spherical caps, the height of the cap is thus indicative of the contact angle (see the black dotted lines). Anything below the horizontal white dashed line is a reflection off the substrate. All scale bars correspond to 50 μm

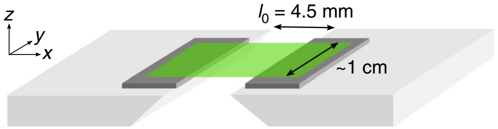

Fig. 2 Schematic of the sample holder used to apply precise strains to the films. The sample holder consists of two aluminium blocks separated by a fixed initial distance l_0. Two pieces of silicon, which have been coated with the same polymeric material as is to be strained, are affixed to the aluminium blocks. The films to be strained are placed such that they bridge the gap between the sample holder blocks. The strong adhesion between the film and the coated silicon pieces keeps the film in place and prevents delamination. The two blocks are then precisely separated by an additional distance Δl along the x-direction, using a motorized translation stage at constant speed, which creates a strain $\varepsilon = \Delta l / l_0$ in the film

Results

Contact angle measurements. In our experiment, polymeric glassy and elastomeric films are strained (Fig. 2) and then transferred onto a silicon wafer. We then place sub-millimetric liquid droplets on those strained films. The droplets are observed to be completely circular when viewed from above. We perform contact angle measurements by viewing the droplets from the side under an optical microscope and fitting their profiles to circular caps, an example of which is shown in the left panel of Fig. 1a. We note that Young–Dupré's law only holds for droplets which are much larger than the elastocapillary length of the system[16]. Therefore, we work exclusively in the regime where the droplet size much exceeds this length scale. All contact angle measurements are performed in air and at room temperature (~20 °C).

Polymeric glasses. In the first part of this study, we perform our measurements on polymeric glasses. Since we want to avoid any plastic deformation of the samples, we choose polysulfone (PSf) and polycarbonate (PC) which have large elongations at yield: up

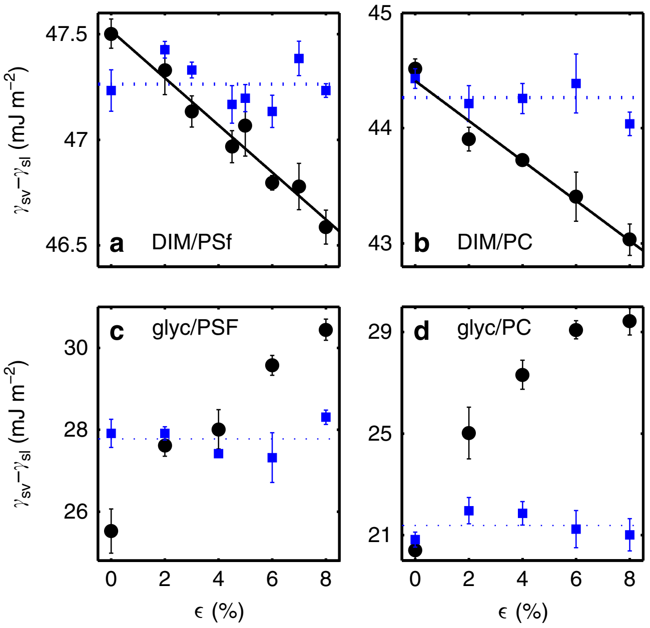

Fig. 3 Surface energy change of strained glasses in contact with two different test liquids. Difference between solid–vapour and solid–liquid surface energies as a function of strain in the solid, shown as circle markers for four liquid–solid combination: **a** diiodomethane/polysulfone, **b** diiodomethane/polycarbonate, **c** glycerol/polysulfone, and **d** glycerol/polycarbonate. The square markers represent room temperature results obtained after annealing the initially strained samples above their glass transition temperature. The average value of these is indicated by the dotted line. The solid lines in **a** and **b** are best fits to Eq. 2, with $k = 2.3 \pm 0.5$ and $\gamma_{\mathrm{sv}}^{(0)} - \gamma_{\mathrm{sl}}^{(0)} = 47.5 \pm 0.1\,\mathrm{mJ\,m^{-2}}$, as well as $k = 1.4 \pm 0.5$ and $\gamma_{\mathrm{sv}}^{(0)} - \gamma_{\mathrm{sl}}^{(0)} = 44.4 \pm 0.3\,\mathrm{mJ\,m^{-2}}$, respectively. Contact angle measurements are repeated several times at each strain, and the vertical error bars represent standard errors in these measurements. Uncertainties in the fitting parameters represent the 95% confidence bounds

to 6 and 8%, respectively, for bulk samples[26]. For the thin film samples and low strain rates employed, we find that both glasses can be strained up to 7–8% without observing crazing. Thus, we vary the strains in the range of 0–8% and discard any sample where crazing is observed. The absolute error in the strain is estimated to be ±1%. Contact angle measurements are performed with two standard test liquids: diiodomethane (DIM), a symmetric, non-polar molecule with $\gamma_{\mathrm{lv}} = 51\,\mathrm{mJ\,m^{-2}}$ (at 20 °C)[27], and glycerol, a highly polar molecule with $\gamma_{\mathrm{lv}} = 63\,\mathrm{mJ\,m^{-2}}$ (at 20 °C)[28].

In Fig. 3a,b, we plot $\gamma_{\mathrm{sv}} - \gamma_{\mathrm{sl}}$, obtained via Young–Dupré's law, as a function of strain for PSf and PC, respectively, with DIM as the test liquid (circles). In both these cases, the contact angle increases with strain, causing $\gamma_{\mathrm{sv}} - \gamma_{\mathrm{sl}}$ to decrease. This result demonstrates, for the first time, the existence of strain-dependent surface energies for interfaces involving a polymeric glass.

Using Eq. 1, the surface stress difference at zero strain $\Upsilon_{\mathrm{sv}}^{(0)} - \Upsilon_{\mathrm{sl}}^{(0)}$, where the (0) superscript will henceforth refer to the unstrained ($\varepsilon = 0$) case, can be determined by fitting a line to each of the data sets (circles) in Fig. 3a, b. In doing so, the surface stress difference at zero strain is found to be, respectively, 11 and 17 mJ m^{-2} smaller than the surface energy difference at zero strain, $\gamma_{\mathrm{sv}}^{(0)} - \gamma_{\mathrm{sl}}^{(0)}$, for PSf and PC, respectively. Similarly, the dependence of $\gamma_{\mathrm{sv}} - \gamma_{\mathrm{sl}}$ upon strain for PSf and PC with glycerol as the test liquid is shown (circles) in Fig. 3c, d. A clear strain dependence is again observed. Surprisingly, $\gamma_{\mathrm{sv}} - \gamma_{\mathrm{sl}}$ increases with strain with this polar liquid, contrary to the results with DIM. Due to curvature in these data, they are not well described by a linear relationship, but fitting a line to the first few data points allows us to determine approximate values for $\Upsilon_{\mathrm{sv}}^{(0)} - \Upsilon_{\mathrm{sl}}^{(0)}$. The magnitude of the effect is much larger with glycerol as the test liquid, as $\Upsilon_{\mathrm{sv}}^{(0)} - \Upsilon_{\mathrm{sl}}^{(0)}$ is found to be roughly 60 and 140 mJ m^{-2} larger than, $\gamma_{\mathrm{sv}}^{(0)} - \gamma_{\mathrm{sl}}^{(0)}$, for PSf and PC, respectively.

After performing the measurements above using the strained glassy films (supported on silicon wafers), we anneal the supported films in the melt state (~30 °C above their glass transition temperature) for 15 min. This procedure relaxes the pre-applied strain in the films. Next, the films are quenched back down to room temperature, and this thermal change induces a contraction. The expansion coefficient of silicon is much smaller than that of the polymer films. Therefore, as the films re-enter the glassy state, their strong adhesion to the silicon wafers restricts them from contracting in the *x*–*y* plane any further than the thermal contraction of the silicon. Therefore, although the pre-applied strain is erased by the annealing, a small biaxial strain $\varepsilon_{\mathrm{t}} \approx 1\%$ is introduced due to thermal contraction[29]. Then, we perform contact angle measurements once more, and the corresponding surface energy differences are plotted as squares in Fig. 3. As can be seen in these plots, the value of $\gamma_{\mathrm{sv}} - \gamma_{\mathrm{sl}}$ is now constant with respect to the pre-applied strain ε. These data intersect the previous measurements (circles) at a small non-zero strain, as expected from the small, $\varepsilon_{\mathrm{t}} \approx 1\%$ biaxial strain present in the film due to thermal contraction.

To further assure that our results are not an artefact due to a plastic deformation of the surface upon straining, we performed two additional tests. First, atomic force microscopy scans (not shown) reveal no noteworthy difference between strained and unstrained films. No signs of crazing or anisotropic topography are seen on the strained sample, and the typical surface roughness is unchanged. Second, one PC film was strained to $\varepsilon = 6\%$—below plastic yield—and subsequently peeled off the holder blocks (Fig. 2). The peeled film could thus relax the elastic deformation it was initially subjected to and was subsequently transferred onto a silicon wafer. The measured contact angle on that sample was found to lie within error of the value measured on an unstrained PC film.

A remaining question concerns the origin of the sign change between the slopes of the data sets for the two test liquids (Fig. 3a–d, circles). The striking difference between the two liquids is that DIM (Fig. 3a, b) is non-polar, whereas glycerol (Fig. 3c, d) is highly polar. To provide further evidence for the important role of polarity, we perform contact angle measurements with water on PSf. For the droplet sizes relevant to our experiments, the evaporation rate of water is too high to perform robust measurements of θ_{Y}. Instead, we perform advancing and receding contact angle measurements. The advancing and receding contact angles of water on PSf decreased by 7 ± 4° and 11 ± 3° over a 7% strain, implying an increase in $\gamma_{\mathrm{sv}} - \gamma_{\mathrm{sl}}$. Thus, both polar liquids, water and glycerol, show the same increasing trend of $\gamma_{\mathrm{sv}} - \gamma_{\mathrm{sl}}$ with strain. Moreover, since surface energies characterize the molecular interactions at the interface, we would anticipate a significant difference whether these interactions are permanent–permanent dipole (Keesom force), permanent-induced dipole (Debye force), or induced–induced dipole (London dispersion force) in origin[30]. Therefore, we suspect that the polarity of the liquid is the source of the difference in slope sign.

Minimal model. The surface energy difference $\gamma_{\mathrm{sv}} - \gamma_{\mathrm{sl}}$ can be re-written as: $\gamma_{\mathrm{sv}} - \gamma_{\mathrm{sl}} = -\gamma_{\mathrm{lv}} + W_{\mathrm{lvs}}$, where $W_{\mathrm{lvs}}(\varepsilon)$ is the work of adhesion between the liquid and solid (with vapour in between) and depends on strain. A simple treatment of the work of adhesion between two non-polar materials requires that the van der Waals interaction energy between two atoms is integrated for all pairs across the interface (Hamaker's calculation)[30]. If we consider such a calculation for two semi-infinite half spaces of liquid and solid, W_{lvs} is proportional to the mass density product $\rho_l\rho_s$. As a simplification, we suppose that physical properties (e.g., polarizability) other than ρ_s do not vary with strain. In this approach, a positive strain ε can induce a reduction in the density ρ_s, which causes a proportional reduction in W_{lvs}, implying a reduction in $\gamma_{\mathrm{sv}} - \gamma_{\mathrm{sl}}$. Indeed, the mass density of our films upon straining is given by $\rho_s = \rho_s^{(0)}[1-(1-2\nu)\varepsilon/k]$ in the limit of small strains, where ν is the Poisson ratio of the film, and where the parameter k depends on details of the straining geometry but is expected to be unity when the strained solid is completely unclamped at its sides in the y-direction and z-direction (Fig. 2) but smaller than unity if the film is fully clamped. The constant k is left as a free parameter in this minimal approach. Therefore, for dispersive interactions, we have a simple prediction for the strain dependence of the surface energy difference:

$$\gamma_{\mathrm{sv}} - \gamma_{\mathrm{sl}} = \gamma_{\mathrm{sv}}^{(0)} - \gamma_{\mathrm{sl}}^{(0)} - \left(\gamma_{\mathrm{sv}}^{(0)} - \gamma_{\mathrm{sl}}^{(0)} + \gamma_{\mathrm{lv}}\right)\frac{(1-2\nu)}{k}\varepsilon. \qquad (2)$$

Given that $\nu = 0.37$ for both PSf and PC[26], we can fit Eq. 2 to our DIM/PSf and DIM/PC data leaving both $\gamma_{\mathrm{sv}}^{(0)} - \gamma_{\mathrm{sl}}^{(0)}$ and k free. The results are shown as solid lines in Fig. 3a, b. These fits describe the data well, and from these we extract values of $\gamma_{\mathrm{sv}}^{(0)} - \gamma_{\mathrm{sl}}^{(0)}$ which are in agreement with those obtained from contact angle measurements on unstrained films (see Fig. 3a, b), and determine k to be 2.3 ± 0.5 and 1.4 ± 0.5 for DIM/PSf and DIM/PC, respectively. Though k is of order unity, as expected, the minimal model is missing some important ingredients. For instance, the polarizability of the molecules in the solid may change with strain, or the surface density may behave differently under strain compared to the bulk. The simple model we have proposed is applicable to the dispersive interactions between a non-polar liquid and a solid, but cannot be simply extended to interactions involving permanent dipoles. Indeed, a polar liquid like glycerol introduces an additional degree of complexity in the interfacial interactions[3].

Elastomers. In the second part of this study, we perform contact angle measurements upon various elastomers using several test liquids. We employ two physically crosslinked elastomers: styrene–isoprene–styrene (SIS) triblock copolymer, and Elastollan which is a thermoplastic polyurethane multiblock copolymer, as well as one chemically crosslinked elastomer: polyvinyl siloxane (PVS). We measure θ_Y for these three elastomers using glycerol and DIM as the test liquids, with the exception of SIS for which we replace DIM by polyethylene glycol (PEG), since SIS is swollen by DIM. The results of the contact angle measurements for all liquid–elastomer combinations are shown in Fig. 4, where we plot $\theta_Y - \langle\theta_Y\rangle_\varepsilon$, that is, the deviation of the equilibrium contact angle from its mean value taken over all measured strains, as a function of strain. As seen in this plot, all contact angles remain constant within ±1° up to 100% strain. These trends together with Young–Dupré's law imply that $\frac{d\gamma_{\mathrm{sv}}}{d\varepsilon} = \frac{d\gamma_{\mathrm{sl_1}}}{d\varepsilon} = \frac{d\gamma_{\mathrm{sl_2}}}{d\varepsilon}$ for all strains, where 1, 2 indicate the two different test liquids. However, there is no physically sound reason to expect the solid–vapour surface energy to change by a non-zero amount under strain in exactly the same way as the solid–liquid surface energy, for an arbitrary choice of test liquid. In fact, one might expect the polarity of the liquid to play an important role. Thus, a reasonable expectation is that $\frac{d\gamma_{\mathrm{sv}}}{d\varepsilon} = \frac{d\gamma_{\mathrm{sl}}}{d\varepsilon} = 0$ for the interfaces involving the elastomers, which would imply through Eq. 1 that $\Upsilon_{\mathrm{sv}} = \Upsilon_{\mathrm{sv}}^{(0)} = \gamma_{\mathrm{sv}} = \gamma_{\mathrm{sv}}^{(0)}$ and $\Upsilon_{\mathrm{sl}} = \Upsilon_{\mathrm{sl}}^{(0)} = \gamma_{\mathrm{sl}} = \gamma_{\mathrm{sl}}^{(0)}$, and thus no Shuttleworth effect. Since we have tested several elastomers (physically and chemically crosslinked) and liquids (with varying polarity), we conjecture that this suggested property is applicable to solid–fluid interfaces involving elastomers in general. If correct, this conjecture may be understood in the following simple way: elastomers are essentially incompressible ($\nu \approx 0.5$) liquids which are constrained by cross-links on length scales much larger than those relevant to intermolecular interactions. Thus—despite the strain—the local molecular environment, density, and consequently stress and energy near the interface remain mostly unchanged.

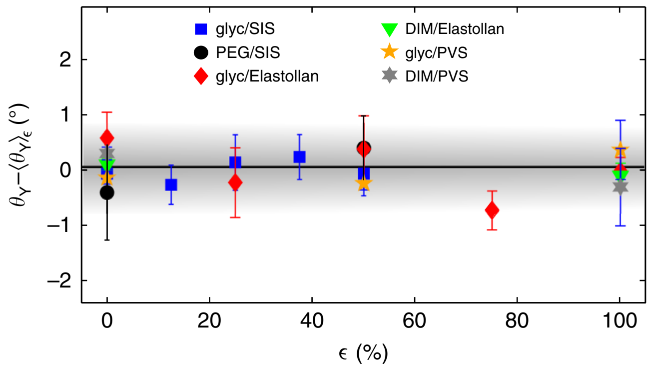

Fig. 4 Contact angles on strained elastomeric substrates. Equilibrium contact angles relative to their average over all strains as a function of strain, for three elastomers using three different test liquids. Equilibrium contact angles are compared to the average value over all strains because this provides better statistics for the normalization compared to plotting with respect to the value at $\varepsilon = 0$, in which case the normalization is determined only by one data point in each set and, as such, is more prone to error. Vertical error bars represent standard errors in the measurement

Discussion

In carrying out contact angle measurements, care must be taken to ensure that contact angle hysteresis does not cause artefacts. Here, the contact angle hysteresis is small (e.g., <5° for glycerol on PSf) on the glassy substrates since the spincoated films are uniform and clean. We find the measured contact angle to be highly reproducible from one droplet to the next. Given the methods of droplet deposition employed in this study, the measured static contact angle is expected to be closer to the advancing contact angle, but is a reliable approximation of the true Youngs angle due to the small hysteresis present. Given all the consistency checks that have been performed, including advancing/receding contact angle measurements with water which exhibit a consistent trend with strain, it is clear that hysteresis cannot be the cause of our main observations.

The fact that droplets in these experiments are completely circular when viewed from above emphasizes an important point. We apply uniaxial strains and hence the surface stresses, which are tensor quantities, are different in the directions normal and tangential to the strain. However, since our droplets are orders of magnitude larger than the elastocapillary length, the macroscopic contact angles measured are determined by Young–Dupré's law and thus functions of the surface energies, which are scalar quantities[16]. For this reason, the macroscopic contact angle is constant around the circumference of the droplet and the droplet's shape is a spherical cap.

Our study is motivated by the on-going debate on whether or not surface stresses in elastomers are identical to surface energies[14–25]. One set of experiments measured the surface stresses of an interface involving PVS by dipping a rod of this elastomer into an ethanol bath and measuring the deformation of the rod both above and beneath the liquid–air interface[14,21]. In the aforementioned experiment, $\frac{d\gamma_{sl}}{d\varepsilon} - \frac{d\gamma_{sv}}{d\varepsilon} = 43 \pm 10$ mN m^{-1}, in contradiction to our data which suggests that $\frac{d\gamma_{sl}}{d\varepsilon} - \frac{d\gamma_{sv}}{d\varepsilon} = 0$ for all solid–fluid interfaces involving elastomers (including PVS). However, the result of Refs. [14,21] relies on a model of the system which has recently been questioned[31]. In addition, the measurements of the local strains are highly sensitive to any minute swelling the submerging liquid may induce, since swelling affects ρ_s.

Other experiments have utilized the shape of the wetting ridge created at the contact line of a liquid droplet on a soft PDMS substrate to determine surface stresses of interfaces involving an elastomer[16,18]. In a recent study, PDMS substrates were strained up to 25% and, thereafter, the wetting ridge was imaged to deduce the strain-dependent surface stresses[23,24]. It was found that Υ_{sv} and Υ_{sl}—approximated to be equal due to a specific choice of liquid—more than doubled over the range of strains tested, despite the equilibrium contact angle remaining unchanged. Although this result is in principle consistent with our elastomer data in Fig. 4, it is inconsistent with our suggestion that $\frac{d\gamma_{sv}}{d\varepsilon} = \frac{d\gamma_{sl}}{d\varepsilon} = 0$ for elastomers. A noteworthy point is that considerations of how the elastic stress due to the strain affects the shape of the wetting ridge are not included in that study. In addition, although PDMS is a ubiquitous material which is important to study, it is also a challenging material as it is known to contain uncrosslinked chains which can migrate to the surface and act as a lubricant[32], among other possible unexpected effects[33]. We acknowledge that the same effects may be present in PVS as well, and stress that PVS was only studied here to facilitate a direct comparison with Ref. [14].

Let us stress that all these studies, whether providing evidence for or against the equality between surface stress and surface energy for solid–fluid interfaces involving elastomers, are highly dependent upon a model to extract Υ from the raw data. In our work, we simply rely on Young–Dupré's law to attain the results we present and, in turn, directly probe the surface stress difference $\Upsilon_{sv} - \Upsilon_{sl}$.

As discussed in the context of our minimal model, the fact that the value of the factor k (see Eq. 2) falls outside the expected range may indicate that the relevant physics is not described solely by the density changes upon strain. In fact, at large extensions, the orientation of chains, and thus the polarizability, will also be modified. Previous work has shown that orientation of chains in semicrystalline materials can induce contact angle changes for large strains (~100%)[34]. This type of effect could even play a role in some elastomers which are rich in double bonds. In such materials, if there is a sufficiently strong strain-induced birefringence, it is possible that a surface energy change will exist upon strain, despite the density remaining constant. We also expect that polarizability effects may be responsible for the different behaviours we observe for polar vs. non-polar liquids.

In this study, we have investigated the strain dependence of the solid–vapour and solid–liquid surface energies of interfaces involving amorphous materials, using contact angle measurements. The glassy materials tested show a significant change in $\gamma_{sv} - \gamma_{sl}$ with strain, which serves as a first demonstration of the Shuttleworth effect for glassy materials. In addition, we show that changing the polarity of the test liquid switches the sign of the strain dependence of $\gamma_{sv} - \gamma_{sl}$. In contrast, we show that $\gamma_{sv} - \gamma_{sl}$ remains constant for strains as large as 100% for several different elastomers, using various test liquids with different polarities. Our data are consistent with the notion that incompressible elastomers do not exhibit a Shuttleworth effect.

Methods

Polymer details and annealing protocols. PSf with number-averaged molecular weight $M_n = 22$ kg mol^{-1} (Sigma-Aldrich) is dissolved in cyclohexanone (Sigma-Aldrich, puriss p.a. >99.5%). Psf films are made with a thickness of $h \approx 400$ nm. These films are annealed at 220 °C for 12 h. The re-annealing after contact angle measurement is done at 220 °C for 15 min. Poly(Bisphenol-A Carbonate) (PC) with $M_n = 22$ kg mol−1 (Polymer Source Inc.) and polydispersity index of 1.9 is dissolved in chloroform (Fisher Scientific, Optima grade). PC films are made with a thickness of $h \approx 1200$ nm. These films are annealed at 170 °C for 12 h. The re-annealing after contact angle measurement is done at 175 °C for 15 min. SIS triblock copolymer (Sigma-Aldrich) with a 14% styrene content is dissolved in toluene (Fisher Scientific, Optima grade). These films are made with a thickness of $h \approx 1300$ nm and annealed at 110 °C for 10 min. Elastollan TPU 1185A (BASF) is dissolved in cyclohexanone (Sigma-Aldrich, puriss p.a. >99.5%). These films are made with a thickness of $h \approx 250$ nm and annealed at 100 °C for 90 min. PVS elastomer is made by mixing base and catalyst (RTV EC00 Translucid) at a 1:1 ratio. These films are made with thicknesses on the order of several hundred microns.

Sample fabrication and straining protocol. With the exception of the PVS samples, all films are prepared by spincoating out of solution. The samples are cast onto freshly cleaved mica substrates (Ted Pella Inc.) to produce uniform films. Subsequently, all samples (except PVS) are annealed to relax the polymer chains and remove any residual solvent that may be present within the sample. The glassy films are scored into ~1 cm squares using a scalpel blade. The elastomeric samples are also divided into squares of ~1 cm but rather using a cotton-tip applicator which is wetted with acetone. The films are then floated onto the surface of an ultrapure water bath (18.2 MΩ-cm, Pall, Cascada, LS) and subsequently picked up using a home-built sample holder (Fig. 2). The PVS samples are made by depositing a drop of the catalyst–base mixture onto a freshly cleaved mica substrate and spreading it into a film using a clean glass pipette and then leaving the elastomer to cure for 1 h. The film is subsequently peeled off the mica and placed onto the sample holder. The initial gap between the two blocks of the sample holder (i.e., the length of the film being strained, see Fig. 2) was fixed at $l_0 = 4.5$ mm. The water–air surface energy ensures that the films are taut (albeit at a strain ≪1% for the glasses and <5% for the elastomers) while floating and during the transfer onto the sample holder. After drying of the residual water from the floating process, one of the blocks of the sample holder is held in place while the other is attached to a translation stage (Newport MFA-CC, SMC100CC). The blocks are then un-fixed and the film is stretched along the x-axis. For the glassy films, the block is moved at a speed of 10 μm s^{-1} equivalent to a strain rate of 2.2×10^{-3} s^{-1}. Performing the straining at 20 μm s^{-1} produces no observable difference in the final results; however, as the speed is increased above 100 μm s^{-1}, we observe an increase in the likelihood of crazing. For the elastomeric films, the block is moved at a speed of 100 μm s^{-1} to reduce the time required to achieve the large strains. We observe no difference in the results when these films are strained at a speed of 10 μm s^{-1}.

Once strained, the sample holder is rotated upside down and carefully translated down until the film bridging the gap between the two blocks makes contact with a silicon wafer which is placed below. Strong adhesive forces between the film and the smooth silicon wafer ensure that the film remains fixed to the wafer and thus unable to relax its strain. At this point, we cut the edges of the film with a scalpel to remove it from the sample holder, completing the sample preparation. The atomic force microscopy scans to ensure there are no apparent topographical changes to the strained surfaces in comparison to unstrained are performed with a Bruker, Multimode 8.

Contact angle measurements. Contact angle measurements are performed under an optical microscope. Measurements are performed immediately following droplet deposition. For DIM (Sigma-Aldrich, Reagent Plus, 99%), the contact radii r of the droplets are in the range of $300 < r < 500$ μm. For glycerol (Caledon Laboratories Ltd.) and PEG (Sigma-Aldrich, $M_n = 0.6$ kg mol^{-1}), the contact radii are in the range of $50 < r < 350$ μm. The sufficiently large size of the droplets and the rapidity of the measurement ensure that evaporation does not significantly affect our measurements. For the PVS experiments, we work only with droplets with $r > 200$ μm to ensure that the droplets are much larger than the elastocapillary length of the system. Droplets are placed as close as possible to the centre of the film where the strain is least affected by the boundary conditions of the experimental straining geometry. However, we observe no systematic difference in the contact angles depending on the location of the droplet on the film. The droplet profiles are fit to circular caps to extract their radius of curvature R, from which the contact angle is attained using the relation $\sin(\theta_Y) = r/R$. For each sample, several different droplets are imaged and the average contact angle is determined.

To rule out potential effects due to swelling, we only employ liquid–solid combinations which are known to be highly immiscible. Since we work with thin films, which undergo colour changes upon minute thickness or refractive index changes, it is easily verified that there is no significant swelling of our films upon exposure to the test liquids used since colour changes are not observed.

It is known that interfacial properties may depend upon the method with which the sample was prepared. For instance, a film which has been spincoated may exhibit different properties on the interface which was in contact with the substrate compared with the free interface. In order to be consistent, all our contact angle measurements are performed on the interface of the film which was in contact with the mica during spincoating.

Data availability. The data that support the findings of this study are available from the corresponding author upon request.

Received: 21 November 2017 Accepted: 6 February 2018
Published online: 07 March 2018

References

1. Shuttleworth, R. The surface tension of solids. *Proc. Phys. Soc. Lond. Sec. A* **63**, 444 (1950).
2. Cammarata, R. C. Surface and interface stress effects in thin films. *Prog. Surf. Sci.* **46**, 1–38 (1994).
3. Ibach, H. The role of surface stress in reconstruction, epitaxial growth and stabilization of mesoscopic structures. *Surf. Sci. Rep.* **29**, 195–263 (1997).
4. Sander, D. Surface stress: implications and measurements. *Curr. Opin. Solid State Mater. Sci.* **7**, 51–57 (2003).
5. Müller, P. & Saúl, A. Elastic effects on surface physics. *Surf. Sci. Rep.* **54**, 157–258 (2004).
6. Nicolson, M. M. Surface tension in ionic crystals. *Proc. R. Soc. Lond. Ser. A* **228**, 490–510 (1955).
7. Berger, R. et al. Surface stress in the self-assembly of alkanethiols on gold. *Science* **276**, 2021–2024 (1997).
8. Mays, C., Vermaak, J. & Kuhlmann-Wilsdorf, D. On surface stress and surface tension: ii. determination of the surface stress of gold. *Surf. Sci.* **12**, 134–140 (1968).
9. Wasserman, H. & Vermaak, J. On the determination of a lattice contraction in very small silver particles. *Surf. Sci.* **22**, 164–172 (1970).
10. Wasserman, H. & Vermaak, J. On the determination of the surface stress of copper and platinum. *Surf. Sci.* **32**, 168–174 (1972).
11. Shanahan, M. The influence of solid micro-deformation on contact angle equilibrium. *J. Phys. D* **20**, 945 (1987).
12. Bostwick, J. B., Shearer, M. & Daniels, K. E. Elastocapillary deformations on partially-wetting substrates: rival contact-line models. *Soft Matter* **10**, 7361–7369 (2014).
13. Mora, S., Phou, T., Fromental, J.-M., Pismen, L. M. & Pomeau, Y. Capillarity driven instability of a soft solid. *Phys. Rev. Lett.* **105**, 214301 (2010).
14. Marchand, A., Das, S., Snoeijer, J. H. & Andreotti, B. Capillary pressure and contact line force on a soft solid. *Phys. Rev. Lett.* **108**, 094301 (2012).
15. Nadermann, N., Hui, C.-Y. & Jagota, A. Solid surface tension measured by a liquid drop under a solid film. *Proc. Natl. Acad. Sci. USA* **110**, 10541–10545 (2013).
16. Style, R. et al. Universal deformation of soft substrates near a contact line and the direct measurement of solid surface stresses. *Phys. Rev. Lett.* **110**, 066103 (2013).
17. Weijs, J. H., Snoeijer, J. H. & Andreotti, B. Capillarity of soft amorphous solids: a microscopic model for surface stress. *Phys. Rev. E* **89**, 042408 (2014). 1310.3941.
18. Park, S. J. et al. Visualization of asymmetric wetting ridges on soft solids with X-ray microscopy. *Nat. Commun.* **5**, 4369 (2014).
19. Mondal, S., Phukan, M. & Ghatak, A. Estimation of solid–liquid interfacial tension using curved surface of a soft solid. *Proc. Natl. Acad. Sci. USA* **112**, 12563–12568 (2015).
20. Andreotti, B. et al. Solid capillarity: when and how does surface tension deform soft solids? *Soft Matter* **12**, 2993–2996 (2016).
21. Andreotti, B. & Snoeijer, J. H. Soft wetting and the Shuttleworth effect, at the crossroads between thermodynamics and mechanics. *Eur. Phys. Lett.* **113**, 66001 (2016).
22. Xu, X., Jagota, A., Paretkar, D. & Hui, C.-Y. Surface tension measurement from the indentation of clamped thin films. *Soft Matter* **12**, 5121–5126 (2016).
23. Xu, Q. et al. Direct measurement of strain-dependent solid surface stress. *Nat. Commun.* **8**, 555 (2017).
24. Xu, Q., Style, R. W. & Dufresne, E. R. Surface elastic constants of a soft solid. Preprint at http://arXiv.org/abs/1711.10300 (2017).
25. Liang, H., Cao, Z., Wang, Z. & Dobrynin, A. V. Surface stress and surface tension in polymeric networks. *ACS Macro Lett.* **7**, 116–121 (2018).
26. Margolis, J. M. *Engineering Thermoplastics: Properties and Applications* (Marcel Dekker, New York, 1985).
27. Good, R. J. & Elbing, E. Generalization of theory for estimation of interfacial energies. *Ind. Eng. Chem. Res.* **62**, 54–78 (1970).
28. Lide, D. R. *CRC Handbook of Chemistry and Physics* (CRC, Boca Raton, 2004).
29. Fortais, A., Schulman, R. D. & Dalnoki-Veress, K. Liquid droplets on a free-standing glassy membrane: deformation through the glass transition. *Eur. Phys. J. E* **40**, 69 (2017).
30. Israelachvili, J. N. *Intermolecular and Surface Forces: Revised*3rd edn (Academic, New York, 2011).
31. Hui, C.-Y. & Jagota, A. Wetting of a partially immersed compliant rod. *J. Appl. Phys.* **120**, 195301 (2016).
32. Hourlier-Fargette, A., Antkowiak, A., Chateauminois, A. & Neukirch, S. Role of uncrosslinked chains in droplets dynamics on silicone elastomers. *Soft Matter* **13**, 3484–3491 (2017).
33. Rivetti, M. et al. Elastocapillary levelling of thin viscous films on soft substrates. *Phys. Rev. Fluids* **2**, 094001 (2017).
34. Good, R. J., Kvikstad, J. A. & Bailey, W. O. Anisotropic forces in the surface of a stretch-oriented polymer. *J. Colloid Interface Sci.* **35**, 314–327 (1971).

Acknowledgements

The financial support by Natural Science and Engineering Research Council of Canada is gratefully acknowledged. We thank the Global Station for Soft Matter, a project of Global Institution for Collaborative Research and Education at the Hokkaido University, as well as the Joliot chair from ESPCI Paris. We also thank Y. Amarouchene, B. Andreotti, A. Antkowiak, L. Bureau, A. Chateauminois, M. Chaudhury, K. Daniels, C. Drummond, E. Dufresne, A. Hourlier-Fargette, H. Perrin, P. Rambach, F. Restagno, J. Snoeijer, R. Style and Q. Xu for valuable suggestions and comments.

Author contributions

All authors contributed to designing the research project, R.D.S. performed all experiments and analysed the data, M.T. lead the development of the theoretical model with input from all authors, R.D.S. wrote the first draft of the manuscript, and all authors edited the manuscript to generate a final version and contributed to the discussion throughout the entire process of the research.

Additional information

Competing interests: The authors declare no competing financial interests.

3.4 Paper IV

Liquid dewetting under a thin elastic film

R. D. Schulman, J. F. Niven, M. A. Hack, C. DiMaria and K. Dalnoki-Veress, Soft Matter, **14**, 3557 (2018).

This work examines the dewetting of a thin liquid film which is capped by an elastic membrane. First, we study the dewetting of a thin polystyrene (PS) film which is situated between a rigid silicon substrate on one side and a thin elastic layer on the opposite side. The elastic films are strained using the apparatus described in Section 2.2.3, and we begin by introducing an isotropic tension into these films. When the sample is heated above the T_g of PS, circular holes nucleate in the PS which grow linearly in time (akin to viscous dewetting on a non-slipping substrate, described in Section. 1.2.3) after a brief initial transient. We find that the dewetting speed decreases with increasing tension in the elastic membrane. An increased tension also leads to a flatter and wider dewetting rim, which is attributed to be the cause of the decreased dewetting speed.

Next, we study the effects of tension anisotropy in the capping elastic film on dewetting. When the elastomer has a biaxial tension, holes acquire a non-circular shape which is elongated along the high tension direction. The rim shape is also non-uniform surrounding the hole, and we find it to be consistent with a shape that maintains a constant pressure throughout the rim. Furthermore, we create a unique free-standing sample geometry wherein the PS film is sandwiched between two biaxially stretched elastic films whose high tension directions are oriented perpendicular to one another. Under these conditions, PS holes nucleate and grow with a square morphology. Thus, we show that exploiting elastic membranes as boundary conditions offers a promising new avenue for controlling liquid patterning in dewetting.

This study began with the undergraduate student C. DiMaria, who was supervised by Dr. Dalnoki-Veress and me. The initial idea was to study the dewetting of a thin liquid on a compliant free-standing elastic membrane. However, we found only a very subtle dependence on the tension in the film. This sample geometry was abandoned as C. DiMaria discovered the method for producing square holes, and the project changed to studying dewetting capped by an elastic membrane. At this juncture, the project was handed off to M. A. Hack, an intern student from University of Twente, who worked under the supervision of Dr. Dalnoki-Veress and myself. M. A. Hack performed preliminary experiments, measurements, and data analysis. After his internship ended, I took the reins of the project. I performed all subsequent experiments (which comprised the bulk of the final data in the paper) and data analysis. J. F. Niven assisted with AFM measurements throughout. I wrote the first draft of the manuscript, which was then revised by all other contributors.

Soft Matter

PAPER

View Article Online
View Journal

Check for updates

Cite this: DOI: 10.1039/c8sm00255j

Liquid dewetting under a thin elastic film†

Rafael D. Schulman,[a] John F. Niven,[a] Michiel A. Hack,[a] Christian DiMaria[a] and Kari Dalnoki-Veress *[ab]

Received 4th February 2018,
Accepted 16th April 2018

DOI: 10.1039/c8sm00255j

rsc.li/soft-matter-journal

We study the dewetting of liquid films capped by a thin elastomeric layer. When the tension in the elastomer is isotropic, circular holes grow at a rate which decreases with increasing tension. The morphology of holes and rim stability can be controlled by changing the boundary conditions and tension in the capping film. When the capping film is prepared with a biaxial tension, holes form with a non-circular shape elongated along the high tension axis. With suitable choice of elastic boundary conditions, samples can even be designed such that square holes appear.

1 Introduction

Dewetting, the study of the spontaneous withdrawal of a liquid off a substrate, has been a topic of intense research over the last several decades.[1–21] In part, this is due to the fact that dewetting serves as a powerful tool to probe physical properties and principles such as: residual stresses in polymer films,[4,5] rheological properties of viscoelastic materials,[6–8] hydrodynamic slip conditions and the dynamics of the contact line,[9–12] as well as determining the effective interface potential and Hamaker constants of a system.[13–15] In addition, dewetting may be utilized to generate pattern formation at microscopic length scales. Novel dewetting morphologies are typically introduced by chemical and topological patterning in the substrate itself.[16–21]

Liquid patterning at small length scales may also be achieved using principles of elastocapillarity, which is the study of the interplay between a solid's elasticity and a liquid's capillarity. In particular, when a solid substrate is sufficiently deformable (either because it is a soft material or because the chosen geometry is highly compliant), the solid will experience large-scale deformation due to capillary forces of a droplet acting upon it.[22–30] Due to this principle, droplets can migrate towards regions of a substrate that are less stiff, which can be used to pattern a soft substrate with liquid droplets.[24] In another study, droplets are shown to map out the stresses in free-standing elastic films by assuming a shape which is elongated along the direction of highest tension.[30] More fundamentally, the replacement of a rigid boundary condition with a compliant one leads to unique wetting properties which show departures from the classic descriptions, such as Young-Dupré's law of partial wetting.[23,25,27,29,30]

Few studies have investigated the intersection of dewetting and elastocapillarity; those that do have focused on a liquid dewetting off a bulk elastic solid and have chiefly been theoretical in nature.[31–35] Some studies have investigated systems where the liquid film is capped by a thin, compliant elastic layer.[36–39] In one set of experiments, the dewetting of thin water films between two sheets of mica, several microns thick, was observed.[36,38] Although the effect of changing the stiffness of the elastic layer was not systematically studied, it was noted that thicker mica sheets (less compliant) resulted in slower dewetting.

In this work, we study the dewetting of a liquid film which is capped by a taut, thin elastic film. Increasing tension in the elastic layer leads to a reduction in the hole growth rate, a flatter and wider dewetting rim, as well as increased stability of the rim. In addition, we show for the first time that elastic capping films can be utilized to generate novel dewetting morphologies. A biaxial tension causes holes to appear with an elongated, non-circular shape. Further, we show that these elastic boundaries can be manipulated to generate holes with a square morphology.

2 Experimental methods

In these experiments, thin polystyrene (PS) films (Scientific Polymer Products, number averaged molecular weight $M_n = 15\,800$ g mol^{-1},

---

[a] Department of Physics and Astronomy, McMaster University, 1280 Main St. W., Hamilton, ON, L8S 4M1, Canada. E-mail: dalnoki@mcmaster.ca

[b] Laboratoire de Physico-Chimie Théorique, UMR CNRS Gulliver 7083, ESPCI Paris, PSL Research University, 75005 Paris, France

† Electronic supplementary information (ESI) available: Detailed overview of the straining apparatus and procedure, equations to estimate tension and film thickness upon straining, late stage evolution of elongated holes, further explanation of the force balance at the rim's contact line, and movies for the growth of circular and square holes. See DOI: 10.1039/c8sm00255j

polydispersity index 1.05) of thickness $h_{PS} \sim 100$ nm, measured using ellipsometry (Accurion, EP3), were prepared through spincoating out of a toluene solution onto 1 cm × 1 cm silicon wafers. The PS was removed near the four sides of the silicon using an acetone-wetted cotton swab. The PS samples were then annealed on a hot stage (Linkam) at 140 °C for 10 min to relax the polymer chains and remove any residual solvent. Elastomeric films were prepared from Elastollan TPU 1185A (BASF). Upon spincoating these solutions, the Elastollan polymers, which contain hard and soft segments, self-assemble to form an elastomer with physical crosslinks. The Elastollan/cyclohexanone solutions were cast onto 3 cm × 3 cm freshly cleaved mica substrates (Ted Pella Inc.) to produce highly uniform ($<5\%$ variation) films with initial thickness in the range $h_0 \sim 50$–320 nm, measured using ellipsometry. These films were subsequently heated atop a hot stage at 150 °C for 10 min to remove any residual solvent from the elastomer. After annealing, these films were scored using a scalpel along each edge of the mica and dipped into an ultrapure water bath (18.2 MΩ cm, Pall, Cascada, LS). In doing so, a thin film of water wedges itself between the Elastollan film and the mica substrate. Subsequently, the films are easily transferred to home-built straining apparatus. The straining apparatus consists of a 250 μm thick elastomeric Elastosil sheet (Wacker Chemie) which is cut into a rounded 'plus' shape, with a circular hole at its center. Each of the four edges of the thick Elastosil sheet is clamped to a post which can translate along an axis. The sheet is held taut by the clamps. The Elastollan film to be strained is suspended over the hole in the thick Elastosil sheet. When the posts are moved outward, the Elastosil sheet stretches, and the hole at its center expands. As a result, the suspended Elastollan film becomes stretched as well. When all four posts are translated outward by the same amount, the Elastosil sheet becomes stretched such that the hole at its center grows in size, but remains circular. Thus, the Elastollan film suspended over this hole, gets stretched radially outward (equally in all directions) and the strain ε is isotropic. If the posts are instead displaced further along one axis compared to the posts along the orthogonal axis, the hole in the Elastosil acquires an elliptical shape. In this way, the suspended elastollan film is stretched biaxially with strains ε_{low} and ε_{high} in the two orthogonal directions. The initial film thickness of the Elastollan is chosen such that the final film thickness after straining, h, is a fixed quantity. In this study, we test $h = 50$ nm and 100 nm. The strained films are then transferred onto the PS sample. Having removed PS from the edges of the silicon wafer, the Elastollan makes good contact with the silicon around the perimeter of the sample, which ensures that the pre-strain in the film cannot relax. Using ellipsometry, h is measured in this portion of the sample with no PS. The sample is then ready for the experiment. Refer to the ESI† for the full details of the straining protocol and sample preparation.

To observe dewetting of the PS, samples are annealed at 140 °C at which PS is a melt and Elastollan remains elastic. Within minutes of heating, small holes form in the PS film (through heterogeneous nucleation) surrounded by rims where the liquid has collected, as depicted schematically in Fig. 1(a). These holes quickly adopt a circular shape and the elastic film acts as a solid capping layer during this process. In the dry region from which the PS has retracted, the elastic film forms adhesive contact with the silicon substrate. The growth of several holes is monitored using an optical microscope (Fig. 1(b)) and the radius of each hole, r, is measured over time (Fig. 1(c)). For the first ~100 min, the hole growth speed is changing with time, which in other dewetting systems has been caused by complex transient dynamics or liquid slip at the contact line being important at early times,[40–42] but could also be a result of elastic effects in the capping film. Thereafter, the speed of dewetting, v, tends towards a constant, analogous to standard dewetting (*i.e.* Newtonian, viscous, non-slipping liquid on a rigid surface).[1,2] The holes are tracked until the rim exhibits significant morphological changes due to undergoing an instability akin to the Plateau–Rayleigh Instability (PRI).[43–45]

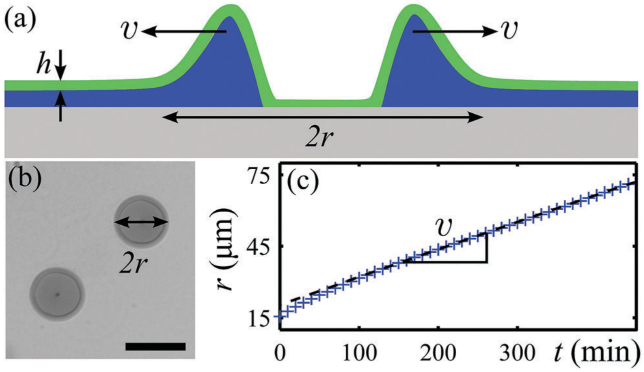

Fig. 1 (a) Schematic of PS film dewetting atop silicon and capped by a thin elastomeric film. The material from the hole collects in a rim which moves outward with speed v. (b) Optical micrograph of two holes capped by an elastomeric film with an isotropic strain ε = 28% after 250 min. Scale bar = 100 μm. (c) Radius of a hole in the experiment depicted in (b) over time. The dashed line is the best fit to the linear growth region, and its slope is the dewetting speed v.

3 Results and discussion

3.1 Hole growth and rim shape under isotropic tension

In the first part of this study, we investigate how the dewetting speed is influenced by changes in the isotropic strain of the capping elastomer. Since we are changing the strain in the films while keeping their final thickness constant, we are primarily changing the tension, T, in the films, while maintaining a nearly constant bending rigidity. In the case of a Hookean material, the tension is simply related to the strain, $T \propto \varepsilon h$ (see ESI†). In the absence of a measured stress–strain relationship of the elastomer at 140 °C, we use εh as an approximate indicator of the tension in the film, although Elastollan is not Hookean over large strains.[46] Thus, in Fig. 2(a), we plot the dewetting speed v as a function of εh for two different values of h. We see that the dewetting speed decreases with increasing strain in the elastomer. In addition, changing the elastomer thickness by a factor of two (*i.e.* an eight-fold change in the bending rigidity) produces no observable change in v. This observation implies that bending of the

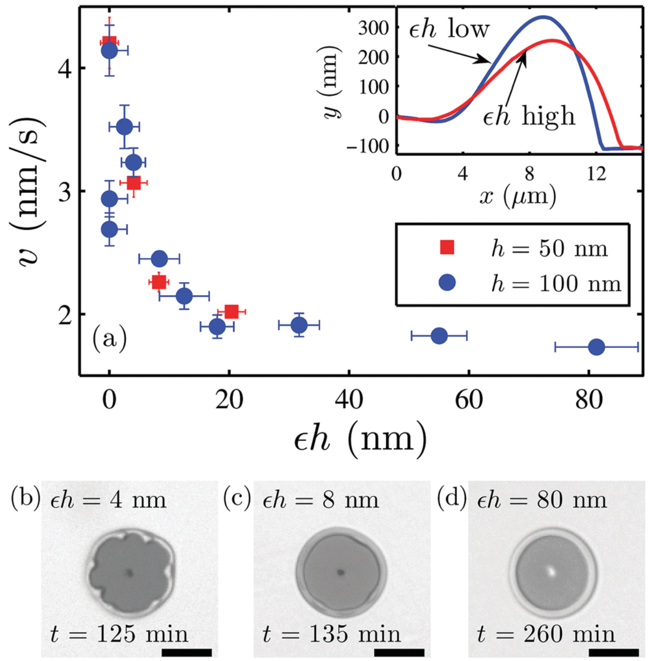

Fig. 2 (a) Dewetting speed as a function of εh, which is proportional to the tension, for two different elastomeric film thicknesses. Inset: AFM profiles of the rim shape for a low (εh = 4 nm) and high (εh = 80 nm) tension sample. (b–d) Optical micrographs of holes of the same size but with different tension in the capping elastomer. Scale bars = 50 μm.

elastomer does not determine the dewetting rate, but rather the tension in the film plays the dominant role. In the inset of Fig. 2(a), we show atomic force microscopy (AFM) profiles of rims for samples with $\varepsilon h \sim 4$ nm and $\varepsilon h \sim 80$ nm. From these scans, it is clear that increased tension results in a flatter, wider rim.

In the simplest model, we assume that the tension is not globally altered by the formation of holes. This simplistic picture is consistent with the observations that the dewetting rate (which depends on T) is constant as holes grow and independent of the number of nucleated holes on a sample. Within this approximation, the energy per unit area of the wet regions of the sample is $E_{\text{wet}} = T + \gamma_{\text{el,v}} + \gamma_{\text{el,l}} + \gamma_{\text{s,l}}$, where γ represents interfacial tensions, "el", "v", "l" and "s" denote the elastomer, vapour, liquid and the solid substrate. The energy per unit area of the dry regions is $E_{\text{dry}} = T + \gamma_{\text{el,v}} + \gamma_{\text{el,s}}$. Therefore, the spreading parameter $S = E_{\text{dry}} - E_{\text{wet}}$ is not dependent on the tension, and thus, the driving force for dewetting remains unchanged when the tension is altered. Thus, the change in tension must alter the dissipation in the system.

A simple balance of mechanical and interfacial tensions at the contact line (see ref. 29, 30 and the ESI†), yields a relation for the equilibrium contact angle $\theta_{\text{E}} \approx \theta_0 \Big/ \sqrt{1 + T/(\gamma_{\text{el,v}} + \gamma_{\text{el,l}})}$ of the capped rim in the limit of small angles, where θ_0 is the equilibrium contact angle for vanishing mechanical tension. This expression is qualitatively consistent with the inset of Fig. 2(a), where an increased tension results in a flatter rim (smaller dynamic contact angle). The dissipation in this system could stem from a combination of several plausible mechanisms. If viscous dissipation at the contact line dominates, then the dewetting speed is proportional to the dynamic contact angle of the capped rim.[1] If hydrodynamic slip is important, then the dissipation may be area-dependent rather than concentrated at the contact line; but for either of these mechanisms, a flatter and wider rim will result in increased dissipation.[2,9,40] There might also be energy lost due to viscoelastic effects in the elastomer; however, we see no clear reason why an increased stress in the elastomer would implicate a larger dissipation.

In Fig. 2(a), we see that the dewetting speed decreases slowly with εh when $\varepsilon h \gtrsim 20$. There are two potential reasons why this might be the case. If the rim shape determines the dewetting speed, we would expect v to decrease asymptotically towards zero in the limit of infinite tensions and a completely flat rim, which appears to be the case in Fig. 2(a). Moreover, although we have approximated the elastomer to be Hookean for simplicity, if the full stress–strain relationship of the elastomer is neo-Hookean, the tension would increase more slowly with strain at large values. Since the tension determines the dewetting speed, this could, in part, explain why v decreases more slowly at large εh.

Changing tension also affects the stability of the liquid rim, as seen in Fig. 2(b–d). Despite the holes being equal in size, the low tension sample shows rims which have reached late stages of the rim instability as fingers are in the process of forming, the intermediate sample shows bulges in the rims, while the high tension sample exhibits rims which appear unaffected by the instability. It is known that liquids dewetting off more wettable substrates (*i.e.* lower dynamic contact angle, wider rims) are less susceptible to developing the rim instability.[43,44] Analogously, here the higher tension samples are characterized by rims which are flatter and wider, and this leads to increased rim stability (consistent with the PRI: a lower curvature increases stability).

3.2 Elongated holes under biaxial tension

There is great interest in utilizing dewetting for microscopic pattern formation.[16–21] Although a theoretical study has shown that spinodal dewetting patterns become anisotropic atop biaxially strained bulk elastic substrates,[35] there has been no subsequent work studying the possibility of exploiting elasticity to generate novel morphologies. Thus, we perform the first investigation of how hole morphology may be altered using a capping elastomeric layer. In these experiments, we anneal the uncapped PS samples long enough that circular holes form. An elastic film is strained only along one direction and held fixed in the perpendicular direction ($\varepsilon_{\text{high}}h \sim 100$ nm, $\varepsilon_{\text{low}}h \sim 0$) and then transferred onto the sample, and the experiment proceeds as usual. As seen in Fig. 3(a), an AFM scan reveals that the initial hole shape is completely circular, as we have prepared it. However, after a short time, the hole adopts a shape which is elongated along the high tension direction (Fig. 3(b)). Holes that form after capping are also elongated in the same way, but we purposefully choose to start with a small circular hole, to ensure a more robust initial condition. At first, the elongated hole is surprising because Fig. 2(a) implies that holes grow

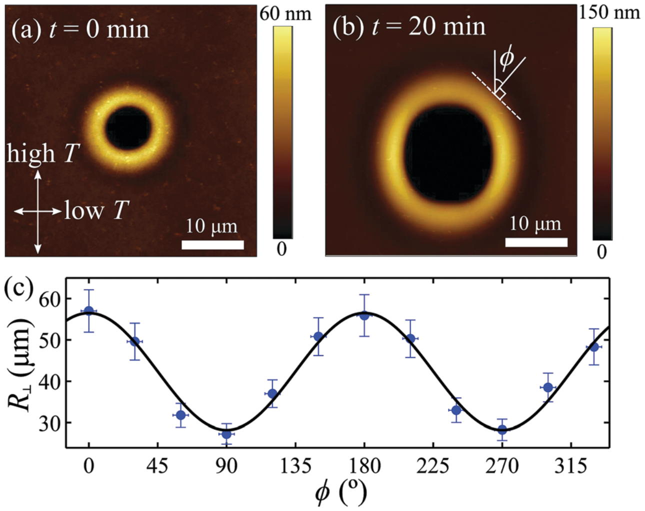

Fig. 3 (a) AFM scan of the initially round hole which has been capped by an elastomeric film with $\varepsilon_{\text{high}} \sim 100\%$, $\varepsilon_{\text{low}} \sim 0\%$ and $h \sim 100$ nm. (b) AFM scan of the same hole after annealing. (c) For the hole at the time of (b), $R_\perp$ as a function of the orientation of the rim (defined in (b)). The solid curve represents the best fit of the expression for $R_\perp(\phi)$ discussed in the text (R_0 = 28 μm). In the AFM scans, colours indicate relative heights on the sample, and the bottom of the hole is outside of the colour bar range. The high and low tension axes are oriented as shown in (a).

slower with high tension, and naïvely, we would thereby expect holes to be elongated along the low tension direction. However, since we are investigating the initial shape of the hole here, it necessarily implies that the energetic cost of forming the rim determines the morphology, and the physics pertaining to the later stages of dewetting, where the growth rate of the round holes was constant in time, is not applicable. In fact, we observe that the elongated holes' rims become unstable before even reaching a constant dewetting speed (see ESI† for further discussion). Therefore, it is not possible to formulate a quantitative comparison between the dewetting speed of the round holes and the dynamics of the elongated holes. To first create the rim, extra interface is created, and work is done against mechanical and interfacial tensions. It is then favourable to deform the film less across the high tension direction and more across the low tension direction – this balance leads to an elongated shape shown in Fig. 3(b). This argument is analogous to deforming a trampoline with an anisotropic tension – an asymmetric deformation would result.

Consistent with the case of isotropic tension, the elongated hole (Fig. 3(b)) has a flatter rim along the high tension direction. We quantify the rim's shape by the radius of curvature of the top of the rim for a slice normal to the hole, $R_\perp$ (*i.e.* the radius of curvature at the peak of the rim profiles akin to those shown in the inset of Fig. 2(a)). The radius of curvature of the rim for a slice in the tangential direction is much larger and need not be considered. For the hole shown in Fig. 3(b), we measure $R_\perp$ for different values of ϕ, defined as the angle the normal of the rim subtends to the high tension direction, indicated in Fig. 3(b). These data are plotted in Fig. 3(c), where it is clear that the radius of curvature of the rim is much larger along the high tension direction. At these early times, wherein the rim energetics dictate the hole's shape, we expect that the liquid within the entire rim has a constant Laplace pressure. If bending is ignored, as validated above, the pressure in the rim is $P \approx T_{\text{tot}}/R_\perp$, where T_{tot} is the total mechanical and interfacial tensions between the elastomer–air interface and elastomer–liquid interface. However, at these large strains, the mechanical tension is dominant over interfacial tensions, since the Young's modulus of Elastollan is $\sim 10^7$ Pa (see ESI†).[46] Thus, we can simply write $R_\perp \approx PT$. Since the film is prepared with a biaxial strain, $T = T_{\text{high}}\cos^2\phi + T_{\text{low}}\sin^2\phi$. For a Hookean material with a Poisson's ratio of 0.5 (typical of elastomers), it is the case that $T_{\text{high}} = 2T_{\text{low}}$ when $\varepsilon_{\text{low}} = 0$. We can use this fact to generate an approximate expression for $R_\perp$, and find that $R_\perp \approx R_0(2\cos^2\phi + \sin^2\phi)$, where R_0 is a constant. In Fig. 3(c), the solid curve represents the best fit of the expression for $R_\perp(\phi)$, with R_0 as the only free-parameter. Despite the approximations made, $R_\perp(\phi)$ captures the curvature of the rim well.

3.3 Holes with square morphology

In the experiments described thus far, the PS film is sandwiched between an elastic film and a rigid silicon substrate. However, the rigid substrate may also be substituted for an elastic film. To further manipulate the boundary conditions for dewetting, we make the sample depicted in Fig. 4(a). Here, a biaxially strained elastomeric film ($\varepsilon_{\text{high}}h \sim 140$ nm) is transferred onto a steel washer with a circular hole. The PS film is placed atop this elastomer. Finally,

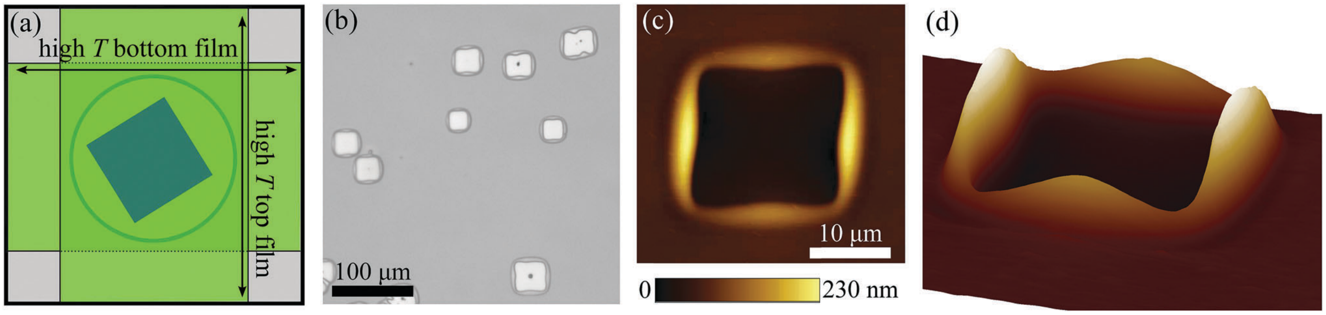

Fig. 4 (a) Top view schematic of the sandwiched sample. The trilayer sample is free-standing over the hole in the washer, and the PS is sandwiched between two biaxially stretched elastic films. (b) Optical micrograph of the square holes nucleating in the PS. (c and d) AFM scan of a square hole. Colours indicate relative heights on the sample.

a second elastomeric film (strained biaxially in the same way) is placed on top, but with its high tension direction oriented perpendicular to that of the bottom elastomeric film. As such, the sample is a free-standing trilayer: elastomer–liquid–elastomer. When this sample is annealed, the holes evolve with a square morphology with the sides oriented along the principal strain directions. This configuration is maintained as the holes continue to grow (Fig. 4(b) (see Video in ESI†)). As shown in Fig. 4(c and d), an AFM scan of one of these holes performed from the top side of this sample reveals that the rims parallel to the high tension direction of the top film are much taller than the ones parallel to the low tension direction. On the underside of the sample where the high tension direction in the film is perpendicular to that of the top film, we would expect the 3D-morphology in Fig. 4(c and d) to be rotated by 90°. This morphology is completely consistent with the notion that the rim energetics dictate the initial shape of the hole. Precisely as in the elongated hole in Fig. 3(b), it is favourable to minimize the deformation of the elastic film across the high tension direction and maximize it across the low tension direction.

4 Conclusions

In this study, we have investigated the dewetting of a thin liquid film capped by a taut elastomeric layer with both isotropic and biaxial tension. For the case of isotropic tension, holes are round and dewet at a constant speed at long times. A higher tension in the elastomer leads to a flattened rim and decreases the dewetting speed. When the capping elastic film is prepared with a biaxial tension, holes assume a shape which is elongated along the high tension direction, a process driven by the energetics of the rim. By choosing the magnitude and anisotropy of the tension in the elastic film, holes can be designed to have wider and more stable rims or to form with non-circular shapes. In addition, when a liquid film is sandwiched between two elastomeric layers with biaxial tension, holes acquire a square morphology. We have shown that by using thin elastic films to cap the dewetting liquid, a new avenue for patterning emerges.

Conflicts of interest

There are no conflicts to declare.

Acknowledgements

The authors thank Joshua D. McGraw, Elie Raphaël, and Thomas Salez for valuable discussions. The financial support by the Natural Science and Engineering Research Council of Canada is gratefully acknowledged.

References

1 P. de Gennes, F. Brochard-Wyart and D. Quere, *Capillarity and Wetting Phenomena*, Springer, 2008.
2 C. Redon, F. Brochard-Wyart and F. Rondelez, *Phys. Rev. Lett.*, 1991, **66**, 715.
3 G. Reiter, *Phys. Rev. Lett.*, 1992, **68**, 75.
4 G. Reiter, M. Hamieh, P. Damman, S. Sclavons, G. Sylvain, T. Vilmin and E. Raphaël, *Nat. Mater.*, 2005, **4**, 754.
5 P. Damman, S. Gabriele, S. Coppée, S. Desprez, D. Villers, T. Vilmin, E. Raphaël, M. Hamieh, S. A. Akhrass and G. Reiter, *Phys. Rev. Lett.*, 2007, **99**, 036101.
6 K. Dalnoki-Veress, B. Nickel, C. Roth and J. Dutcher, *Phys. Rev. E: Stat. Phys., Plasmas, Fluids, Relat. Interdiscip. Top.*, 1999, **59**, 2153.
7 S. Herminghaus, R. Seemann and K. Jacobs, *Phys. Rev. Lett.*, 2002, **89**, 056101.
8 S. Gabriele, S. Sclavons, G. Reiter and P. Damman, *Phys. Rev. Lett.*, 2006, **96**, 156105.
9 C. Redon, J. Brzoska and F. Brochard-Wyart, *Macromolecules*, 1994, **27**, 468–471.
10 R. Fetzer, K. Jacobs, A. Münch, B. Wagner and T. Witelski, *Phys. Rev. Lett.*, 2005, **95**, 127801.
11 O. Bäumchen, M. Lessel, R. Fetzer, R. Seemann and K. Jacobs, *J. Phys.: Conf. Ser.*, 2010, **216**, 012002.
12 J. D. McGraw, T. S. Chan, S. Maurer, T. Salez, M. Benzaquen, E. Raphaël, M. Brinkmann and K. Jacobs, *Proc. Natl. Acad. Sci. U. S. A.*, 2016, **113**, 1168–1173.
13 R. Seemann, S. Herminghaus and K. Jacobs, *Phys. Rev. Lett.*, 2001, **86**, 5534.
14 R. Seemann, S. Herminghaus and K. Jacobs, *J. Phys.: Condens. Matter*, 2001, **13**, 4925.
15 J. De Silva, M. Geoghegan, A. Higgins, G. Krausch, M.-O. David and G. Reiter, *Phys. Rev. Lett.*, 2007, **98**, 267802.
16 L. Rockford, Y. Liu, P. Mansky, T. Russell, M. Yoon and S. Mochrie, *Phys. Rev. Lett.*, 1999, **82**, 2602.
17 A. M. Higgins and R. A. Jones, *Nature*, 2000, **404**, 476.
18 R. Konnur, K. Kargupta and A. Sharma, *Phys. Rev. Lett.*, 2000, **84**, 931.
19 K. Kargupta and A. Sharma, *Langmuir*, 2002, **18**, 1893–1903.
20 K. Y. Suh and H. H. Lee, *Adv. Funct. Mater.*, 2002, **12**, 405–413.
21 A. Sehgal, V. Ferreiro, J. F. Douglas, E. J. Amis and A. Karim, *Langmuir*, 2002, **18**, 7041–7048.
22 M. Shanahan, *J. Phys. D: Appl. Phys.*, 1987, **20**, 945.
23 A. Marchand, S. Das, J. H. Snoeijer and B. Andreotti, *Phys. Rev. Lett.*, 2012, **109**, 236101.
24 R. W. Style, Y. Che, S. J. Park, B. M. Weon, J. H. Je, C. Hyland, G. K. German, M. P. Power, L. A. Wilen, J. S. Wettlaufer and E. Dufresne, *Proc. Natl. Acad. Sci. U. S. A.*, 2013, **110**, 12541–12544.
25 R. Style, R. Boltyanskiy, Y. Che, J. Wettlaufer, L. A. Wilen and E. Dufresne, *Phys. Rev. Lett.*, 2013, **110**, 066103.
26 N. Nadermann, C.-Y. Hui and A. Jagota, *Proc. Natl. Acad. Sci. U. S. A.*, 2013, **110**, 10541–10545.
27 S. J. Park, B. M. Weon, J. S. Lee, J. Lee, J. Kim and J. H. Je, *Nat. Commun.*, 2014, **5**, 4369.
28 J. B. Bostwick, M. Shearer and K. E. Daniels, *Soft Matter*, 2014, **10**, 7361–7369.
29 R. D. Schulman and K. Dalnoki-Veress, *Phys. Rev. Lett.*, 2015, **115**, 206101.
30 R. D. Schulman, R. Ledesma-Alonso, T. Salez, E. Raphaël and K. Dalnoki-Veress, *Phys. Rev. Lett.*, 2017, **118**, 198002.

31 P. Martin and F. Brochard-Wyart, *Phys. Rev. Lett.*, 1998, **80**, 3296.

32 A. Martin, O. Rossier, A. Buguin, P. Auroy and F. Brochard-Wyart, *Eur. Phys. J. E: Soft Matter Biol. Phys.*, 2000, **3**, 337–341.

33 A. Martin, A. Buguin and F. Brochard-Wyart, *Langmuir*, 2001, **17**, 6553–6559.

34 H. Gérardin, E. Verneuil, A. Constant, S. Dubois, J. Clain, X. Noblin, A. Buguin and F. Brochard-Wyart, *Europhys. Lett.*, 2005, **71**, 418.

35 L. Qiao and L. He, *Eur. Phys. J. E: Soft Matter Biol. Phys.*, 2008, **26**, 387–393.

36 T. Becker and F. Mugele, *J. Phys.: Condens. Matter*, 2002, **15**, S321.

37 S. Kumar and O. K. Matar, *J. Colloid Interface Sci.*, 2004, **273**, 581–588.

38 S. de Beer, D. ‘t Mannetje, S. Zantema and F. Mugele, *Langmuir*, 2009, **26**, 3280–3285.

39 A. Carlson, S. Mandre and L. Mahadevan, *arXiv*, 2015.

40 K. Jacobs, R. Seemann, G. Schatz and S. Herminghaus, *Langmuir*, 1998, **14**, 4961–4963.

41 A. Ghatak, R. Khanna and A. Sharma, *J. Colloid Interface Sci.*, 1999, **212**, 483–494.

42 A. Münch, *J. Phys.: Condens. Matter*, 2005, **17**, S309.

43 A. Sharma and G. Reiter, *J. Colloid Interface Sci.*, 1996, **178**, 383–399.

44 S.-H. Choi and B.-m. Zhang Newby, *J. Chem. Phys.*, 2006, **124**, 054702.

45 O. Bäumchen, L. Marquant, R. Blossey, A. Münch, B. Wagner and K. Jacobs, *Phys. Rev. Lett.*, 2014, **113**, 014501.

46 H.-Y. Mi, X. Jing, M. R. Salick, W. C. Crone, X.-F. Peng and L.-S. Turng, *Adv. Polym. Technol.*, 2014, **33**, 1.

Supplemental Information for "Liquid dewetting under a thin elastic film"

Rafael D. Schulman,[a] John F. Niven,[a] Michiel A. Hack,[a] Christian DiMaria,[a] and Kari Dalnoki-Veress*[ab]

S1 Straining of elastic films

The home made straining apparatus is depicted in Fig. S1(a). The apparatus consists of a 250 μm thick Elastosil sheet which has been cut into a rounded plus sign shape, but contains a circular hole at its center. The Elastosil film is clamped at its four sides and supported by four posts which are able to translate in the directions indicated by arrows in Fig. S1(a). The Elastollan sample is placed atop of the hole in the Elastosil, which immediately causes the the Elastollan film to form strong contact with the Elastosil, allowing the mica to be peeled off and removed. Thus, a thin Elastollan film is left free-standing over the hole in the Elastosil.

Upon transfer, the Elastollan films have a small ($< 5\%$) pre-strain due to being stretched by the surface tension of the water during the sample preparation. In order for the initial condition to be an unstrained film, we must relieve this pre-strain. This is done by slowly bringing all four supports inwards to shrink the size of the Elastosil hole. At the point that the pre-strain is relieved, wrinkles just begin to appear in the Elastollan film. This point serves as the initial condition for the Elastollan film. To then strain the Elastollan film, the four posts supporting the Elastosil are moved outwards to stretch the Elastosil film, and hence, expand the hole at its center. To generate isotropic tension, each support is moved an equal distance such that the Elastosil hole remains circular in shape (Fig. S1(b)). For the biaxial samples, one set of supports is held fixed, while the other set of supports is displaced in the orthogonal direction. This generates a hole in the Elastosil with an elliptical shape (Fig. S1(c)). For the case of isotropic tension, the strain is found by $\varepsilon = (d_\mathrm{f} - d_\mathrm{i})/d_\mathrm{i}$, where d_i and d_f are the initial (i.e. the state after the pre-strain has been relieved) and final diameters of the free-standing Elastollan film. In the case of biaxial tension, the strain along the high-tension direction is evaluated as $\varepsilon_\mathrm{high} = (d_\mathrm{high,f} - d_\mathrm{i})/d_\mathrm{i}$, where $d_\mathrm{high,f}$ is the final diameter of the free-standing Elastollan film along the high-tension axis.

Next, the PS sample is brought into contact with the strained Elastollan film. The Elastollan adheres strongly to the PS and also to the bare silicon frame where the PS has been removed. Using a scalpel, the excess Elastollan is cut to free the sample from the straining set up. At this point, the sample looks as depicted in Fig. S2.

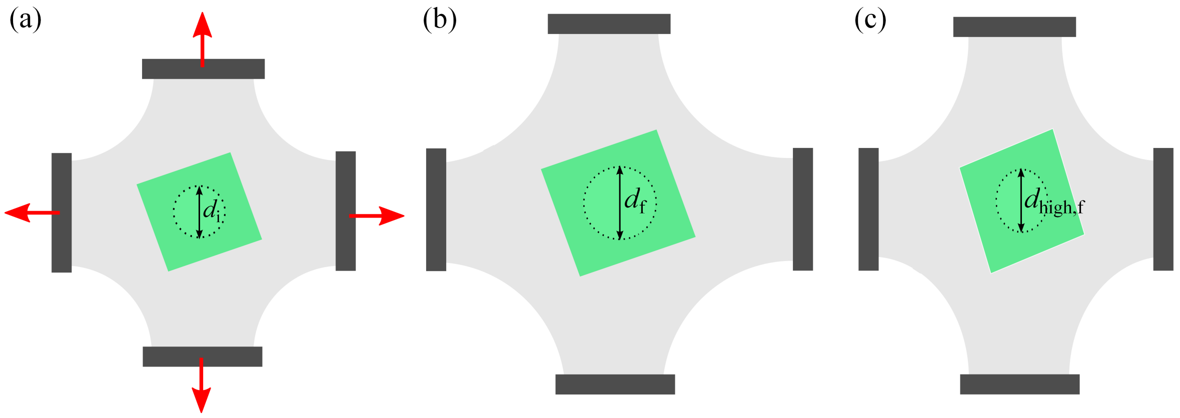

Fig. S1 (a) Top view schematic of the straining apparatus. The Elastollan film is free-standing over the hole in the Elastosil with diameter d_i. The clamped sides of the Elastosil can be translated along the axes indicated by the arrows. (b) An Elastollan film which has been strained equally in both directions (isotropic tension) to a final diameter of d_f. (c) An Elastollan film which has been strained biaxially to a final diameter $d_\mathrm{high,f}$ in one direction, while being held fixed in the orthogonal direction.

---

[a] *Department of Physics and Astronomy, McMaster University, 1280 Main St. W., Hamilton, ON, L8S 4M1, Canada. E-mail: dalnoki@mcmaster.ca*
[b] *Laboratoire de Physico-Chimie Théorique, UMR CNRS Gulliver 7083, ESPCI Paris, PSL Research University, 75005 Paris, France.*

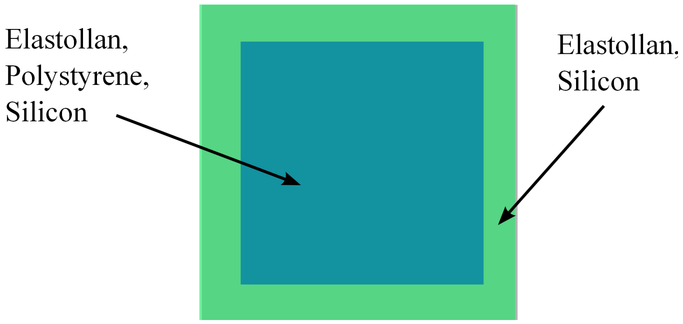

Fig. S2 Top view schematic of the final sample. The labels indicate the different material layers of the sample, listed in order from the top surface to the bottom surface. The ellipsometry measurements are performed in the region of Elastollan on silicon.

S2 Mechanical relationships for straining

Using Hooke's law[1], we can predict simple stress-strain relationships for our films under the assumption of Hookean elasticity. We assume that there is no stress acting in the direction orthogonal to the film (z-direction), i.e. $\sigma_z = 0$. We also know that the mechnical tension is related to stress through film thickness $T = h\sigma$. As such, we may derive a simple expression for isotropic tension generated upon straining:

$$T = \frac{Eh\varepsilon}{1-\nu}, \tag{S1}$$

where ν is the Poisson ratio of the elastomer, which can be assumed to be 0.5, and E is the Young's modulus. Thus, εh is an appropriate indicator for the tension in our films. For the case of biaxial tension where the film is held fixed along one direction ($\varepsilon_{\mathrm{low}} = 0$), we arrive at:

$$T_{\mathrm{low}} = \frac{Eh\nu\varepsilon_{\mathrm{high}}}{1-\nu^2}, \tag{S2}$$

$$T_{\mathrm{high}} = \frac{Eh\varepsilon_{\mathrm{high}}}{1-\nu^2}, \tag{S3}$$

where "high" and "low" indicate the high and low tension directions. Here, we see that under the assumption of Hookean elasticity, $T_{\mathrm{high}} = 2T_{\mathrm{low}}$, since $\nu = 0.5$. In the biaxial tension experiments, $\varepsilon_{\mathrm{high}} \sim 100\%$, $h \sim 100$ nm, and $E \sim 10^7$ Pa[2], which leads to $T_{\mathrm{high}} \sim 1.3$ N/m. Thus, it is clear that mechanical tension will dominate over interfacial tensions in determining the Laplace pressure in the rim.

Since volume is conserved in a material with $\nu = 0.5$, it is possible to predict the final thickness upon an isotropic strain:

$$h = \frac{h_0}{(1+\varepsilon)^2}, \tag{S4}$$

as well as for a biaxial strain with $\varepsilon_{\mathrm{low}} = 0$:

$$h = \frac{h_0}{(1+\varepsilon_{\mathrm{high}})}. \tag{S5}$$

Using the equations above, the initial film thickness h_0 was chosen to produce the desired h (50 nm or 100 nm) once strained.

S3 Equilibrium contact angle

To calculate the equilibrium contact angle that the rim would subtend with the substrate, we appeal to a balance of the interfacial and mechanical tensions depicted in Fig. S3. In this picture, we employ the simplifying assumption that the formation of holes does not alter the mechanical tension in the film. Carrying out the force balance in the horizontal direction yields:

$$T + \gamma_{\mathrm{el,v}} + \gamma_{\mathrm{el,s}} = \left(T + \gamma_{\mathrm{el,v}} + \gamma_{\mathrm{el,l}}\right)\cos\theta_{\mathrm{E}} + \gamma_{\mathrm{s,l}}. \tag{S6}$$

From the equation above, using the small angle approximation in which $\cos\theta \approx 1 - \theta^2/2$, it is straightforward to show that:

$$\theta_{\mathrm{E}} = \frac{\theta_0}{\sqrt{1+\frac{T}{\gamma_{\mathrm{el,v}}+\gamma_{\mathrm{el,l}}}}}. \tag{S7}$$

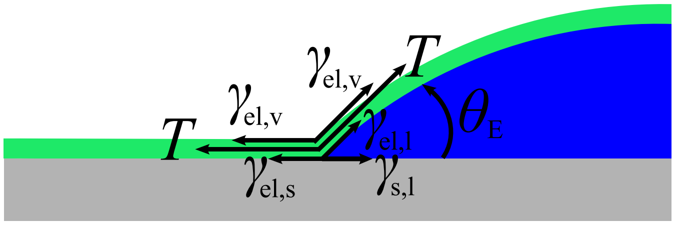

Fig. S3 Balance of interfacial and mechanical tensions to calculate the equilibrium contact angle that the rim subtends with the substrate.

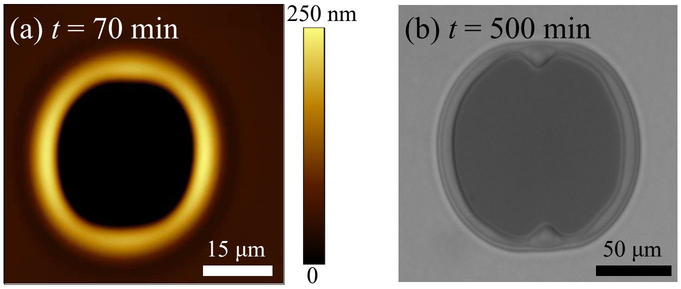

Fig. S4 (a) AFM scan of the hole from Fig. 3(b) once evidence of the rim instability sets in on the high tension sides of the hole. (b) Optical micrograph of the hole after the rim instability has started forming fingers at the high tension ends.

S4 Elongated holes at late times

As the elongated holes continue to grow beyond the early stages described in the main manuscript, we observe that the rim instability rapidly begins to set in on the high tension side of the rim. The early stages of this instability can be seen in an AFM scan of the hole in Fig. 3(b) at $t = 70$ min shown in Fig. S4(a) where there is a bulge forming in the high tension side of the rim. The later stage of this instability is showcased by the optical image in Fig. S4(b), where there are fingers forming at the high tension ends of the hole, yet the low tension side of the rim appears completely stable. In fact, the rim instability sets in at the high tension ends long before the stage of constant dewetting velocity has been reached. For this reason, the physics contained in Fig. 2(a), wherein holes exhibit a smaller v when the tension is larger, cannot be applied to these anisotropic experiments. We suspect that the root of this effect is that depending on a liquid cylinder's orientation, the Plateau-Rayleigh instability can become enhanced or suppressed when a tension anisotropy is introduced in the elastomeric film capping the liquid – this is beyond the scope of this study and will be investigated in future work.

S5 Supplemental movies

Movie S1 - Hole growth when the capping elastomer has an isotropic tension ($\varepsilon h = 8$ nm). The movie is 750 min long.
Movie S2 - Growth of square holes.

References

1 S. Timoshenko and J. Goodier, *Theory of Elasticity, 2nd edition*, McGraw-Hill Book Company, Inc., New York, 1951.
2 H.-Y. Mi, X. Jing, M. R. Salick, W. C. Crone, X.-F. Peng and L.-S. Turng, *Adv. Polym. Tech.*, 2014, **33**, year.

3.5 Paper V

Droplets capped with an elastic film can be round, elliptical, or nearly square

R. D. Schulman and K. Dalnoki-Veress, submitted to Nat. Phys. in April 2018. Manuscript ID: NPHYS-2018-04-00950.

In this final paper, we explore partial wetting of a liquid which is capped by an elastic membrane. In these experiments, the sample substrate consists of a silicon wafer which has been coated with an elastomeric film. Droplets are deposited on the substrate and subsequently capped by an additional elastic film (composed of the same material with which the silicon is coated) which has been strained using the apparatus described in Section 2.2.3. Droplets capped by films with isotropic tension assume the shape of spherical caps with contact angles which decrease with increasing tension. To describe the data, we invoke a horizontal force balance at the contact line, completely analogous to Young-Dupré's law, which includes both mechanical and interfacial tensions. We find an excellent agreement between the experimental data and this simple model, which contains one free parameter. From the free parameter, we determine the interfacial energy between the elastomer and liquid- a quantity which is traditionally difficult to measure. We extract this value for four combinations of two elastomers and two test liquids. In addition, using Young-Dupré's law, we determine γ_{sv} for each of the elastomers twice. The values we obtain for γ_{sv} are reasonable in magnitude and self-consistent within the error of the measurements.

If the droplet is instead capped by a film with biaxial tension, it acquires an elliptical shape when viewed from above. By a simple extension of the contact angle prediction, our model predicts the aspect ratio of the droplets to be given by the relation $\sqrt{T_{\mathrm{high}}/T_{\mathrm{low}}}$. We find this relation to be in close agreement with experimental data. Finally, we design a free-standing sample where droplets are sandwiched between two biaxially stretched elastic films whose high tension directions are oriented perpendicular to one another. In doing so, we observe that droplets acquire a square morphology - in complete analogy with the square holes in the dewetting study. In this free-standing geometry, capped droplets may act as lenses to focus light. Since the droplets' radius of curvature and shape can be changed through the tension in the film, these lenses would be highly tunable. As a demonstration, we shine a laser through a square droplet and show that the resultant focal spot acquires a cross shape. Therefore, this study demonstrates again that elastic boundaries can be useful for liquid patterning and presents a potential application for creating tunable lenses.

This research project was a natural extension for me after having completed the dewetting project. With that, I designed the experimental protocol, made the samples, performed the experiments, and analyzed the data. I developed the simple theoretical model. As before, I wrote the first draft of the manuscript, which was subsequently edited by Dr. Dalnoki-Veress

Droplets capped with an elastic film can be round, elliptical, or nearly square

Rafael D. Schulman[1] and Kari Dalnoki-Veress[1, 2, *]

[1]*Department of Physics and Astronomy, McMaster University,*
1280 Main St. W, Hamilton, ON, L8S 4M1, Canada.
[2]*Laboratoire de Physico-Chimie Théorique, UMR CNRS Gulliver 7083,*
ESPCI Paris, PSL Research University, 75005 Paris, France.
(Dated: April 6, 2018)

When a droplet partially wets a rigid substrate, it assumes the shape of a spherical cap with contact angle set by Young-Dupré's law. However, modifying the boundary conditions for wetting can significantly alter its characteristics, take for example water droplets on a superhydrophobic lotus leaf. In addition, it is known that soft elastic substrates lead to departures from Young-Dupré's law. Here, we present experiments which show that the wetting of droplets capped by taut elastic films is highly tunable. Adjusting the tension allows the contact angle and droplet morphology to be controlled. By exploiting these elastic boundaries, droplets can be made elliptical, with an adjustable aspect ratio, and can even be transformed into a nearly square shape. Our results imply that this system can be used to create tunable liquid lenses, and moreover, presents a unique approach to liquid patterning.

Wetting has been the subject of intense research for well over a century. The activity has been motivated largely by industrial applications, ranging from designing tires to treating textiles and choosing coatings for surfaces, but also by the academic interest in a field which is undeniably rich [1]. A common theme in wetting phenomena is that boundary conditions and substrate play a pivotal role. For instance, when the substrate is replaced by a soft solid, elastocapillary interactions lead to deviations from the classical prediction of Young-Dupré's law due to the formation of a wetting ridge at the contact line [2–9]. The substrate can also be replaced by a thin free-standing elastic film, serving as a compliant boundary for the droplet [11–18]. Work employing such a geometry has shown that the contact angles are set by a Neumann construction in which mechanical and interfacial tensions are balanced at the contact line [12, 13, 15, 17, 18].

Compliant elastic surfaces have also been shown to cause novel wetting behaviours and morphologies. For instance, droplets have been observed to migrate towards regions of increased compliance [19–21], and to interact with other droplets due to deformations induced in the elastic films [16, 22]. Anisotropic tension in a supporting free-standing film causes sessile droplets to elongate along the high tension direction, and thus, droplets map out the stress field in the elastomer [18]. Droplets pressed between a rigid surface and a soft solid acquire the shape of a flattened ellipsoid [10]. In yet another example, dewetting liquid films which are capped by a thin elastic layer exhibit slower dynamics with increased tension in the elastomer, and by introducing anisotropy in the elastic boundaries, dewetting morphologies can be controlled [23].

Although partial wetting on soft or compliant solids has received significant attention in the past, here, we examine partial wetting in a novel geometry wherein droplets are capped by a thin elastic film under tension. This system could serve as a model for blisters or droplets trapped beneath drying paint [24]. We show that the contact angle of these droplets decreases with increased tension, and that this is well described by a horizontal balance of interfacial and mechanical tensions at the contact line. The model contains a free parameter from which the elastomer-liquid interfacial tension may be determined. We extract reasonable values for this quantity for four different liquid-solid combinations. Finally, we show that introducing biaxial stresses in the capping elastic boundary can produce elliptical droplets with tuneable aspect ratio, and even droplets with nearly-square morphology using a suitable choice of sample geometry.

Thin elastomeric films of Elastollan (elast) TPU 1185A (BASF) and styrene-isoprene-styrene (SIS) triblock copolymer (14% styrene content, Sigma-Aldrich) are prepared by spincoating out of cyclohexanone and toluene solutions respectively. Films are spun onto silicon wafers to create substrates and also onto freshly cleaved mica. The films are annealed at 150°C (elast) or 100°C (SIS) for 10 min to remove solvent and relax the polymer chains. The substrate films are of thickness 200 nm (elast) and 400 nm (SIS), as measured using ellipsometry (Accurion, EP3). One edge of each substrate is brushed with an acetone-wetted cotton swab to remove the elastomer from this edge. Small droplets of glycerol (Caledon Laboratories Ltd.) or polyethylene glycol (PEG) with $M_n = 0.6$ kg/mol (Sigma-Aldrich) are deposited onto the substrates. These sessile droplets are capped with a thin film of the same elastomer as the substrate film (to simplify the boundary conditions for wetting), using the following procedure: the capping films are prepared on mica and then transferred onto a home-built straining set-up following the protocol described in Ref. [23]. Using this apparatus, films are loaded isotropically with

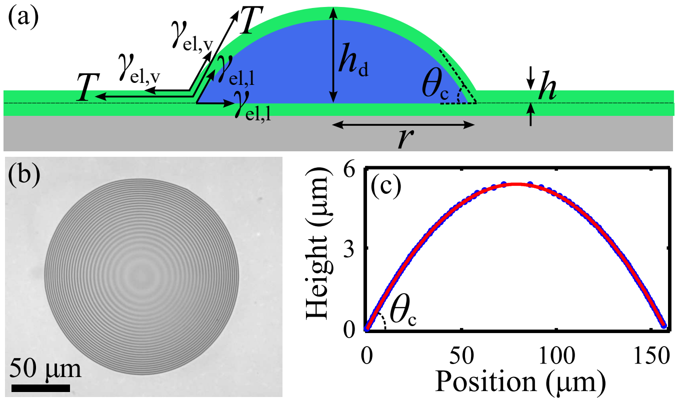

FIG. 1. (a) Schematic of a liquid droplet capped by a taut elastic film and supported by a film of the same elastomer on a silicon substrate. The tension balance to determine the contact angle is shown. (b) Optical micrograph under a red filter of the top view of a glycerol droplet capped by an Elastollan film with $\epsilon = 0.15$ and $h = 570$ nm. (c) Height profile of the capped droplet in (b) as a function of horizontal position. The solid curve is a circular cap fit from which we determine $\theta_{\mathrm{c}} = 7.8 \pm 0.2^{\circ}$.

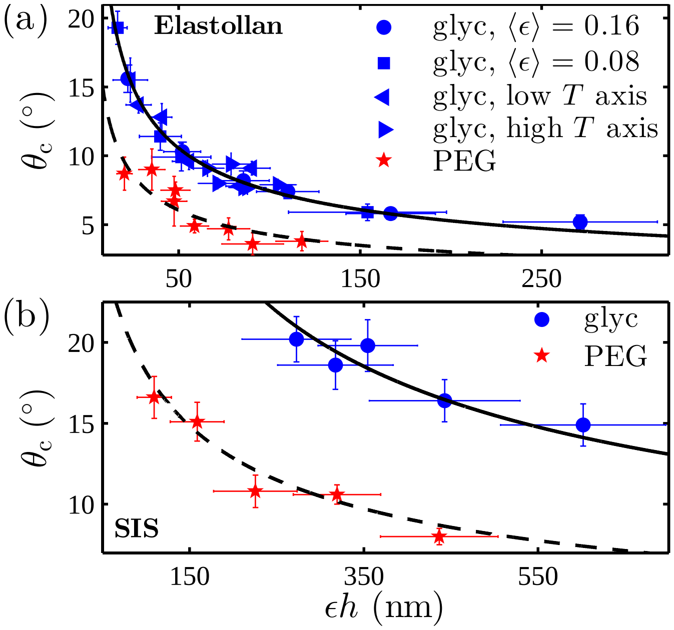

FIG. 2. Contact angle as a function of ϵh, which is proportional to tension, for two elastomers: (a) Elastollan and (b) SIS, and with two test liquids: glycerol (glyc) and PEG. The Elastollan/glycerol data includes sets where the strain is held constant, $\langle\epsilon\rangle = 0.16 \pm 0.03$ (●) and $\langle\epsilon\rangle = 0.08 \pm 0.02$ (■), and only film thickness is changed. Plotted on the same graph are also data attained from biaxial strain experiments along the low (◀) and high (▶) tension axes. Solid (glyc) and dashed (PEG) curves correspond to fits of Eq. 1, with $\gamma_{\mathrm{el,l}}/E$ as the only free parameter. Vertical error bars represent the standard deviation in contact angles measured for a sample, and horizontal error bars stem from uncertainties in thickness and strain.

strain ϵ or biaxially with principal strains ϵ_{low} and ϵ_{high}. The substrate with sessile droplets is then brought into contact with the strained capping film such that strong adhesive contact is formed between the two elastic films, thus completing the sample depicted in Fig. 1(a). We study four different pairings of liquid and elastomer. In the region where the substrate film was removed from the silicon using the cotton swab, we use ellipsometry to determine the thickness h of the capping film. We employ films with h between 150-1700 nm (Elastollan) and 550-3000 nm (SIS).

After being capped, the droplets are circular with a contact radius r when viewed from above. Only droplets which are not visibly pinned are measured. We work with droplets in the range 30 μm $< r <$ 300 μm. Droplets are large enough that evaporation can be ignored, and much larger than the bulk elastocapillary length such that elastic substate films are not significantly deformed by the capillarity of the droplets and can be thought of as uncompliant substrates [5]. In addition, we employ droplet sizes such that bending of the capping film is only relevant locally at the contact line and tension dominates the global picture [25]. Due to the high tension in the capping film, the droplets are sufficiently flattened (to a height h_{d}) to exhibit interference fringes when viewed under an optical microscope with a red ($\lambda = 632.8$ nm) filter (Newport, 10LF10-633), as seen in Fig. 1(b). From this interference pattern, the height profile of the droplet is determined. A height profile from a horizontal slice through the droplet in Fig. 1(b) is shown by the data points in Fig. 1(c). We find that this profile is in excellent agreement with a circular cap fit, shown by the solid curve, from which the radius of curvature R of the capped droplet is measured. If the droplets are large enough, it is also possible to directly image the droplet's profile by acquiring images from a side view, and fit this profile to a circle to extract R. We find good agreement between both techniques. The contact angle of the capped droplet θ_{c} is finally evaluated using the geometric relation $\sin\theta_{\mathrm{c}} = r/R$. Several droplets are measured and the average θ_{c} is determined. The contact angles are highly reproducible from one droplet to the next and independent of the size of the droplet over the range studied.

Although elastomers are not Hookean over large strains, we work exclusively with small strains ($\lesssim 0.2$), such that we can approximate a linear relationship between stress and strain [26]. As such, the mechanical tension in an isotropically strained film is $T = \frac{E\epsilon h}{1-\nu} \approx 2E\epsilon h$, where E is the Young's modulus of the elastomer and $\nu \approx 0.5$ is the Poisson ratio. Thus, the mechanical tension in a capping film can be varied by tuning film thickness or strain. In Fig. 2(a), we plot the contact angle as a function of the product ϵh for Elastollan with glycerol (glyc) droplets. Two data sets are shown wherein

h is varied while the isotropic strain is held constant: $\langle\epsilon\rangle = 0.16 \pm 0.03$ (●) and $\langle\epsilon\rangle = 0.08 \pm 0.02$ (■). The data sets collapse on the same curve and show that contact angle decreases with ϵh. This observation is consistent with previous work which found dewetting rims of a liquid capped with an elastic film to be increasingly more flattened with higher T [23]. Our experiment is repeated with PEG droplets with strains in the range of 0.1-0.2 and variable film thicknesses, and the data is plotted in Fig. 2 (★). Once again, the same trend is seen, but the two liquids, PEG and glycerol, do not collapse onto the same curve. In Fig. 2(b), the two liquids are paired with SIS elastomer instead (again with strains in the range 0.1-0.2 and variable film thicknesses), and the same qualitative trends as in Fig. 2(a) are seen.

To understand these trends, we construct a balance of mechanical and interfacial tensions at the contact line akin to previous work [12, 13, 15, 17, 18]. In the simplest model, we make the assumption that the tension in the capping film is not significantly altered by the deformation induced by the droplet (elastic membrane limit) and remains uniform throughout [27]. This important assumption is discussed later in more detail. The tension balance is shown in Fig. 1(a), where γ represents interfacial tensions between elastomer ("el"), liquid ("l"), and vapour ("v"), and is carried out in the horizontal direction, in analogy with Young-Dupré's law of partial wetting on a rigid solid. Since the substrate is intentionally chosen to be the same material as the capping film, there is no interfacial tension between these. Motivated by previous work on these elastomers, we further assume that the interfacial tensions remain constant with strain (i.e. no Shuttleworth effect) [28]. The horizontal tension balance gives $\cos\theta_c = (T + \gamma_{el,v} - \gamma_{el,l})/(T + \gamma_{el,v} + \gamma_{el,l})$. Note that, just as for Young-Dupré's law, the same result is obtained by a free-energy minimization. Given measured modulus values $E_{elast} = 13 \pm 2$ MPa and $E_{SIS} = 1.1 \pm 0.2$ MPa [26], we calculate that $300 < T < 7000$ mN/m for all our samples. Thus, we make the approximation that T is much greater than any interfacial tension in the system, as interfacial tensions involving polymeric materials are typically < 50 mN/m. Finally, we employ the small angle approximation (since all our contact angles are less than 20°), and uncover a simple prediction for the contact angle:

$$\theta_c = 2\sqrt{\frac{\gamma_{el,l}}{T}} \approx \sqrt{2\frac{\gamma_{el,l}}{E\epsilon h}}. \qquad (1)$$

TABLE I. Interfacial tensions extracted from fitting to contact angle data.

Solid/Liquid	$\gamma_{el,l}/E$ (nm)	$\gamma_{el,l}$ (mN/m)	θ_Y (°)	$\gamma_{el,v}$ (mN/m)
Elast/glyc	0.85 ± 0.04	11 ± 2	67.8 ± 0.8	35 ± 2
Elast/PEG	0.28 ± 0.08	4 ± 1	42.4 ± 0.7	38 ± 1
SIS/glyc	18 ± 3	20 ± 5	82.3 ± 1.3	29 ± 5
SIS/PEG	4.0 ± 0.8	5 ± 1	54 ± 1.2	32 ± 2

Thus, the contact angle is fully determined by the mechanical tension and elastomer-liquid interfacial tension. To test the model, we fit Eq. 1 to each data set in Fig. 2, leaving $\gamma_{el,l}/E$ as a free parameter in each case. The fits are plotted in Fig. 2 as solid (glyc) and dashed (PEG) curves for each of the elastomers, and are in excellent agreement with the data. The best fit values of $\gamma_{el,l}/E$ are shown in Table I. Using our measured values of E, we compute $\gamma_{el,l}$. In addition, we have measured the Young's contact angle (θ_Y) of each solid/liquid combination tested, and the values are listed in Table I. Using the Young-Dupré equation, we can calculate the elastomer-vapour interfacial tension as $\gamma_{el,v} = \gamma_{l,v}\cos\theta_Y + \gamma_{el,l}$, where $\gamma_{l,v}$ is found in the literature to be 63 mN/m [29] and 46 mN/m [30] for glycerol and PEG. Therefore, by measuring contact angles of droplets capped with thin taut elastic films, one can determine the system's solid-liquid and solid-vapour interfacial energies. These interfacial energies are of typical magnitudes for interfacial tensions involving polymeric solids. In fact, $\gamma_{el,v}$ is within error of that quoted in Ref. [31]. Furthermore, as seen in Table I, the values of $\gamma_{el,v}$ are determined twice (using the two liquids) for each solid, and are within error of each other, which further validates the simple model.

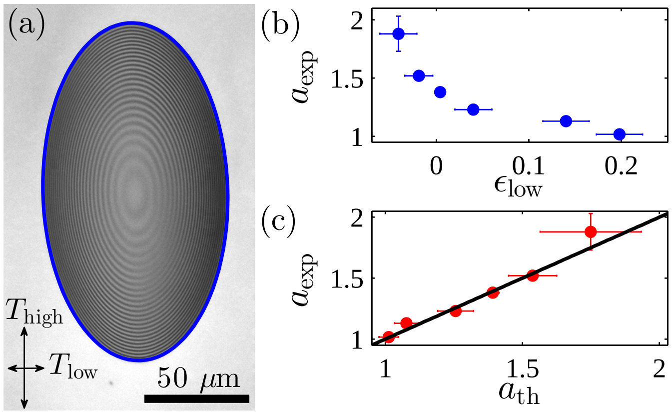

FIG. 3. (a) Optical micrograph under red filter of an elliptical droplet aligned with the high tension direction in the capping film ($\epsilon_{high} = 0.2$, $\epsilon_{low} = -0.04$, $h = 586$ nm). (b) Measured aspect ratio as a function of strain along the low tension axis. ϵ_{high} is held constant at ~ 0.2. (c) Measured aspect ratio plotted against the theoretically expected aspect ratio (Eq. 2) given ϵ_{high} and ϵ_{low}. The solid line represents the relationship $a_{exp} = a_{th}$. Horizontal error bars are due to uncertainties in the two strains. Vertical error bars are standard deviations in measured a_{exp}.

Thus far, all films have been prepared with an isotropic tension. However, previous work has shown that wetting morphologies can be controlled by loading elastic boundaries with anisotropic strains [18, 23]. Thus, we perform additional experiments with Elastollan and glycerol, wherein the droplets are capped by films with a biaxial tension with principal strains $\epsilon_{\rm high}$ and $\epsilon_{\rm low}$. In doing so, droplets assume an elongated shape (Fig. 3(a)) which is well described by an ellipse whose major axis aligns with the high tension direction (plotted as a curve around the perimeter). To understand how the elliptical droplet's measured aspect ratio, $a_{\rm exp}$, varies with strain, we perform experiments where $\epsilon_{\rm high} \sim 0.2$ and $-0.05 < \epsilon_{\rm low} < 0.2$. As seen in Fig. 3(b), the aspect ratio decreases as $\epsilon_{\rm low}$ increases, and approaches unity in the limit of isotropic strain ($\epsilon_{\rm low} = \epsilon_{\rm high}$).

We find that height profiles of the droplet along the high- and low-tension axes are well described by spherical cap fits once again, and from these, we determine the contact angles along both axes ($\theta_{\rm c,high}$ and $\theta_{\rm c,low}$). Along each of the principal axes (high tension or low tension), the tension balance at the contact line, and the final prediction of Eq. 1, is identical to the isotropic case, but with T replaced by $T_{\rm high}$ or $T_{\rm low}$ respectively. Applying Hooke's law, one can calculate the tension along the principal strain direction i to be $T_i \approx \frac{1}{1-\nu^2} E(\epsilon_i + \nu\epsilon_j)h$ where j is the orthogonal principal strain direction and for elastomers we can set $\nu \approx 0.5$. At this point, an effective strain can be defined for this direction $\epsilon_{{\rm eff},i} = \frac{1-\nu}{1-\nu^2}(\epsilon_i + \nu\epsilon_j)$, such that the isotropic expression is recovered for the biaxial case as well: $T_i = \frac{1}{1-\nu} E\epsilon_{{\rm eff},i}h \approx 2E\epsilon_{{\rm eff},i}h$. In this way, the elliptical droplet data for $\theta_{\rm c,high}$ (▶) and $\theta_{\rm c,low}$ (◀) is plotted against $\epsilon_{{\rm eff},i}h$ in Fig. 2(a). As expected, the biaxial strain data collapses onto the same curve as the isotropic strain data.

Since the droplet profiles along both principal directions are well fit to circular caps, the droplet height can be evaluated using the circular cap identity $h_{{\rm d},i} = r_i \tan(\theta_{{\rm c},i}/2) \approx r_i\theta_{{\rm c},i}/2$, where subscript i once again denotes a principal direction (either high or low tension axis) and the small angle approximation was employed. Of course, the droplet height must be the same for profiles taken along either principal direction ($h_{\rm d,high} = h_{\rm d,low}$). Therefore, the theoretical aspect ratio can be calculated as $r_{\rm high}/r_{\rm low}$ to be

$$a_{\rm th} = \frac{\theta_{\rm c,low}}{\theta_{\rm c,high}} = \sqrt{\frac{T_{\rm high}}{T_{\rm low}}} = \sqrt{\frac{\epsilon_{\rm high} + \nu\epsilon_{\rm low}}{\epsilon_{\rm low} + \nu\epsilon_{\rm high}}}, \qquad (2)$$

where we have made use of Eq. 1 and the Hookean relationships described above. For a quantitative test of this result, we refer to Fig. 3(c), where all measurements of the aspect ratio $a_{\rm exp}$ are plotted against their predicted values $a_{\rm th}$, computed using Eq. 2 and the applied strains. Plotted in this way, we find consistency with a line representing $a_{\rm exp} = a_{\rm th}$, indicating good agreement between theory and experiment.

The theory outlined in this study relies on the simple assumption that the tension of the film is not significantly changed by the deformation induced by the droplet. To construct a comprehensive theoretical treatment to calculate the additional stresses created by this deformation, one may follow the methodology presented in articles by Davidovitch, Vella, and co-workers, where the Föppl-von Kármán equations are solved in the limit of vanishing bending contributions [32–34]. However, results we have presented suggest that our assumption is appropriate. Droplets under isotropic tension are well described as spherical caps, which is consistent with the notion of a uniform tension in the elastic film acting against a constant pressure within the capped liquid. The contact angles depend on the prepared tension, i.e. the product ϵh. If the tension was significantly modified during capping, one would expect the additional tension to depend individually on h as well (through the stretching modulus Eh), and would disrupt the collapse of the data seen in Fig. 2(a). However, the strongest evidence in favour of the assumption stems from the success and self-consistency of the model presented herein (success of predictions made by Eq. 1 and Eq. 2, sensible values of $\gamma_{\rm el,l}$ and $\gamma_{\rm el,v}$, and the collapse of biaxial and isotropic strain data in Fig. 2(a)).

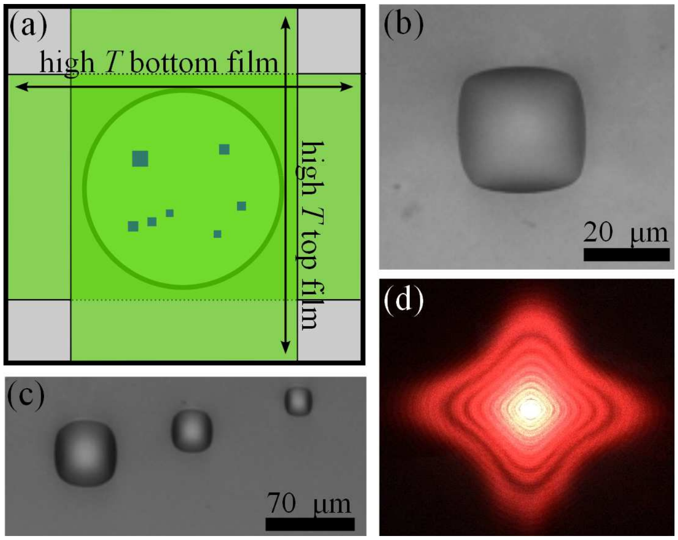

FIG. 4. (a) Top view schematic of the sample with droplets capped by biaxially stretched films on either side, all freestanding over the hole in the washer. (b)-(c) Optical images of droplets with square morphology. (d) Focal spot (with diffraction pattern) of a laser shone through a square droplet.

In previous work, we have seen that using suitable elastic boundary conditions, dewetting liquid films will nucleate holes which are square [23]. Drawing inspiration from that result, we recreate such elastic boundary conditions, but for sessile droplets instead, in the sample depicted in Fig. 4(a). An Elastollan film with biaxial tension ($\epsilon_{\rm high} \sim 2$, $\epsilon_{\rm high} \sim -0.4$) is placed atop a steel washer with a circular hole. Glycerol droplets are deposited on the free-standing portion of this film. Finally, a second Elastollan film subjected to the same biaxial strains is placed on top, but with its high tension axis oriented perpendicular to the bottom film. Thus, the droplets are capped by an elastomer on either side, and the whole system is free-standing. As seen in Figs. 4(b)-(c), droplets in such a sample assume a remarkable square morphology with the sides oriented along the principal strain directions. In this free-standing sample geometry (Fig.4(a)), droplets act as lenses whose focal length and shape can be tuned using the elastic boundary conditions. As a proof of principle, we shine a laser through a pinhole (150 μm in diameter) onto a square droplet. The resultant focal spot (with the diffraction pattern) is shown in Fig. 4(d). As an elliptical droplet resembles a cylindrical lens producing a focal spot in the shape of a line, a square droplet creates a focal spot resembling a cross.

In this study, we have investigated the partial wetting of liquid droplets capped by thin elastic films. When the tension in the elastic film is isotropic, droplets assume the shape of spherical caps which flatten with increasing tension. A horizontal balance of interfacial and mechanical tensions at the contact line well describes the change in contact angle with tension with only one free parameter. From this free parameter, the elastomer-liquid interfacial tension - a notoriously difficult quantity to measure- can be determined. Finally, we show that elastic films as boundary conditions for partial wetting can produce droplets with novel morphologies. Droplets can be designed to have elliptical shapes with aspect ratios that depend on the strains in the elastic film, and it is even possible to generate droplets with square morphology using suitable choices of the elastic boundary conditions. Thus, elastic membranes can be used to create highly tunable liquid morphologies.

The financial support by the Natural Science and Engineering Research Council of Canada the Joliot chair from ESPCI Paris is gratefully acknowledged. We thank A. Fortais for performing modulus measurements.

---

* dalnoki@mcmaster.ca

[1] P. de Gennes, F. Brochard-Wyart, and D. Quere, *Capillarity and Wetting Phenomena* (Springer, 2008).

[2] R. Pericet-Cámara, A. Best, H. J. Butt, and E. Bonaccurso, Langmuir **24**, 10565 (2008).

[3] E. R. Jerison, Y. Xu, L. a. Wilen, and E. R. Dufresne, Phys. Rev. Lett. **106**, 186103 (2011).

[4] R. W. Style and E. R. Dufresne, Soft Matter **8**, 7177 (2012).

[5] R. Style, R. Boltyanskiy, Y. Che, J. Wettlaufer, L. A. Wilen, and E. Dufresne, Phys. Rev. Lett. **110**, 066103 (2013).

[6] A. Marchand, S. Das, J. H. Snoeijer, and B. Andreotti, Phys. Rev. Lett. **109**, 236101 (2012).

[7] S. J. Park, B. M. Weon, J. S. Lee, J. Lee, J. Kim, and J. H. Je, Nat. Comm. **5**, 4369 (2014).

[8] C.-Y. Hui and A. Jagota, Pro. R. Soc. A **470** (2014).

[9] J. B. Bostwick, M. Shearer, and K. E. Daniels, Soft Matter **10**, 7361 (2014).

[10] P. Martin, P. Silberzan, and F. Brochard-Wyart, Langmuir **13**, 4910 (1997).

[11] M. E. Shanahan, The Journal of Adhesion **18**, 247 (1985).

[12] N. Nadermann, C.-Y. Hui, and A. Jagota, Proc. Natl. Acad. Sci. U.S.A. **110**, 10541 (2013).

[13] C.-Y. Hui, A. Jagota, N. Nadermann, and X. Xu, Procedia IUTAM **12**, 116 (2015).

[14] C.-Y. Hui and A. Jagota, Soft Matter **11**, 8960 (2015).

[15] R. D. Schulman and K. Dalnoki-Veress, Phys. Rev. Lett. **115**, 206101 (2015).

[16] T. Liu, X. Xu, N. Nadermann, Z. He, A. Jagota, and C.-Y. Hui, Langmuir **33**, 75 (2016).

[17] A. Fortais, R. D. Schulman, and K. Dalnoki-Veress, Eur. Phys. J. E **40**, 69 (2017).

[18] R. D. Schulman, R. Ledesma-Alonso, T. Salez, E. Raphaël, and K. Dalnoki-Veress, Phys. Rev. Lett. **118**, 198002 (2017).

[19] R. W. Style, Y. Che, S. J. Park, B. M. Weon, J. H. Je, C. Hyland, G. K. German, M. P. Power, L. A. Wilen, J. S. Wettlaufer, and E. R. Dufresne, Proc. Natl. Acad. Sci. U.S.A. **110**, 12541 (2013).

[20] J. B. Alvarez, Y. Bazilevs, R. Juanes, and H. Gomez, Soft Matter (2018).

[21] T. Liu, N. Nadermann, Z. He, S. H. Strogatz, C.-Y. Hui, and A. Jagota, Langmuir **33**, 4942 (2017).

[22] S. Karpitschka, A. Pandey, L. A. Lubbers, J. H. Weijs, L. Botto, S. Das, B. Andreotti, and J. H. Snoeijer, Proc. Natl. Acad. Sci. U.S.A. **113**, 7403 (2016).

[23] R. D. Schulman, J. F. Niven, M. A. Hack, C. DiMaria, and K. Dalnoki-Veress, arXiv preprint arXiv:1711.09318 (2017).

[24] J. Farinha, M. Winnik, and K. Hahn, Langmuir **16**, 3391 (2000).

[25] B. Andreotti and J. H. Snoeijer, Europhys. Lett. **113**, 66001 (2016).

[26] We measure the modulus using tensile stress-strain measurements on fibers consisting of Elastollan and SIS with diameters between 5 and 40 microns. The stress-strain curves are linear within experimental error for strains up to 0.2.

[27] L. Landau and E. Lifshitz, *Theory of Elasticity, 3rd* (Butterworth-Heinemann, New York, 1986).

[28] R. D. Schulman, M. Trejo, T. Salez, E. Raphaël, and K. Dalnoki-Veress, Nat. Commun. **9**, 982 (2018).

[29] D. R. Lide, *CRC Handbook of Chemistry and Physics* (CRC Press, 2004) pp. 6–154.

[30] G. Korosi and E. Kovats, J. Chem. Eng. Data **26**, 323 (1981).

[31] B. Zuo, F. F. Zheng, Y. R. Zhao, T. Chen, Z. H. Yan, H. Ni, and X. Wang, Langmuir **28**, 4283 (2012).

[32] B. Davidovitch, R. D. Schroll, D. Vella, M. Adda-Bedia, and E. A. Cerda, Proc. Natl. Acad. Sci. U.S.A. **108**, 18227 (2011).

[33] H. King, R. D. Schroll, B. Davidovitch, and N. Menon, Proc. Natl. Acad. Sci. U.S.A. **109**, 9716 (2012).

[34] R. Schroll, M. Adda-Bedia, E. Cerda, J. Huang, N. Menon, T. Russell, K. Toga, D. Vella, and B. Davidovitch, Phys. Rev. Lett. **111**, 014301 (2013).

Chapter 4

Conclusions and future outlook

In the work comprising this thesis, we use contact angle measurements to study elastocapillary interactions between liquids and taut solid films. Primarily, we show that wetting phenomena (partial wetting and dewetting) are altered when a free boundary or a rigid boundary is replaced by a compliant membrane. We emphasize the principle that there exists a strong parallel between interfacial tensions and the mechanical tension of an elastic membrane. In Papers I and II, we show that the contact line geometry of a partially wetting droplet on a compliant membrane is found through a Neumann construction incorporating both mechanical and interfacial tensions. This result is completely analogous to the partial wetting of a droplet on a liquid substrate. Further evidence of the parallel is that partial wetting on a rigid substrate wherein the droplet is capped by a membrane is described by a modification to Young-Dupré's law which includes mechanical tension and interfacial tensions (Paper V). Although interfacial tensions are more or less pre-determined by the nature of the materials, the tension in a membrane can be readily modified. Thus, these compliant boundary conditions render wetting phenoma much more tunable. As we have seen, by altering the tension in the solid film, contact angles in partial wetting can be adjusted and dewetting rates can be changed.

However, there is a crucial difference between elastic membranes and interfacial tensions which make these compliant boundary conditions so interesting. Namely, elastic membranes can be prepared with an anisotropic tension, whereas interfacial tensions of amorphous materials are isotropic in nature. Consequently, membranes can be exploited to control liquid patterning. We have shown in Papers II and V that droplets elongate along the high tension direction when sessile on, or capped by, a biaxially stretched elastic film. In this way, droplets on free-standing membranes map out elastic stresses and act as compass needles for the principal directions. Furthermore, compliant boundary conditions can even be designed to produce square-shaped droplets and dewetting holes. We have found that droplets which are capped on either side by compliant elastic membranes can be used as lenses to focus light. Since the magnitude and anisotropy of the tension can be adjusted to change the morphology of the droplets, the focal length and focal spot shape is highly tunable. Moreover, dewetting is generally considered a promising candidate for creating liquid pattern formation on a microscopic scale. However, past studies have used chemical or topographical pre-patterning of the substrate itself to guide dewetting into forming desired morphologies. In Paper IV, we show that compliant boundaries offer a novel avenue for controlling dewetting morphologies.

In Paper III, we address the hotly debated Shuttleworth effect in amorphous materials. We provide the first evidence for the presence of strain-dependent surface energies of interfaces involving glassy polymers. This implies that surface stress (force per unit length) and surface energy (energy per unit area) are not equivalent quantities for these interfaces. On the other hand, we provide strong evidence for the absence of the Shuttleworth effect in elastomeric materials. Although the latter is not a conclusive proof, we believe that the evidence we have brought forth will contribute to the current discussion and reduce confusion within the literature.

There are several extensions and new research ideas which follow naturally from the studies contained within this dissertation. In the following text, I will outline some of these. As we have seen, droplets on compliant substrates induce a deformation below themselves which depends on the tension in the film. Since the wetting configuration is altered by tension, the total free energy of the wetting must also be a function of tension. Therefore, if the elastic film is prepared with a *spatial gradient* in the tension, there must necessarily be a gradient in the free energy as a function of droplet position. Hence, the droplet will be driven to migrate towards a position which minimizes its free energy. We have made modest experimental attempts to observe this spontaneous motion, but have not yet had any sucess. Our current hypothesis is that the driving force in those experiments was not sufficiently large to overcome contact angle hysteresis. Therefore, future work must focus on overcoming this barrier to motion, possibly by designing a tension gradient which maximizes the driving force.

Another promising idea is to use the system studied in Paper V to further address the Shuttleworth effect. In Paper III, we show that $\frac{\mathrm{d}\gamma_{\mathrm{sv}}}{\mathrm{d}\epsilon} = \frac{\mathrm{d}\gamma_{\mathrm{sl}}}{\mathrm{d}\epsilon}$ for interfaces involving elastomers up to strains of 100%. Although this is strong evidence for the absence of a Shuttleworth effect, conclusive proof would require showing that $\frac{\mathrm{d}\gamma_{\mathrm{sl}}}{\mathrm{d}\epsilon} = 0$ or $\frac{\mathrm{d}\gamma_{\mathrm{sv}}}{\mathrm{d}\epsilon} = 0$. In Paper V, we find that fitting the contact angles of partially wetting droplets capped by elastic membranes to a modified Young-Dupré model allows for a robust determination of γ_{sl}. Thus, this system could be used to test whether γ_{sl} remains constant for strains up to 100%. The only complication is that the stress-strain relationship for this range of strains will need to be completely determined in advance, as the elastomer will not be Hookean at such large extensions.

Compliant membranes could also be used to modify other wetting phenomena, such as the Plateau-Rayleigh Instability. If a liquid cylinder is coated with an elastic membrane containing isotropic tension, we would expect to see a change in the growth rate of the instability. Even more intriguing is the notion of capping the liquid with a biaxially stretched elastic film. In this case, the orientation of the high tension direction relative to the axis of the cylinder could potentially also alter the wavelength and stability conditions of the Plateau-Rayleigh Instability.

As seen from this dissertation as well as other work in the field of elastocapillarity, there is no lack of rich physics or unexpected manifestations of self-assembly that can emerge from the interplay between capillarity and elasticity - even for seemingly simple solid structures. Although there are a multitude of future directions to be explored, the work contained in this thesis uncovers some of the important principles at play when liquids interact with taut solid films. Stated quite generally, elastocapillary interactions between liquids and taut elastic films introduce modifications to classical descriptions of wetting, present avenues for generating liquid patterning, and provide fundamental insight into the physics of interfaces.

Appendix A

Papers not included in this thesis

The following papers comprise additional studies that I have been involved in, but have not been included as the core papers for my dissertation. In Paper AI, we study the swimming dynamics of the nematode *C. elegans* in fluids of varying viscosity. By measuring forces during swimming, we determine the drag coefficients of the worm and compare to predictions from classical theories. I was not the main contributor of this study, but co-supervised A. Kasper alongside Dr. Backholm and Dr. Dalnoki-Veress. I helped wth the experiments, data analysis, and editing the manuscript. In Paper AII, we study the elastocapillary deformations induced by a liquid droplet on a thin fiber. We find that the capillary forces of the droplet cause the fiber to bend. For a critical droplet size, proportional to L_{BC} (Eq. 1.54), the fiber spontaneously winds itself around the droplet. Although I am the main contributor in this study (performed the experiments and data analysis, contributed to the theoretical model, and wrote the first draft of the manuscript), the subject is tangential to the theme of this thesis. For Paper AIII, I am not the main contributor, but the subject is relevant to this thesis. Here, we examine the elastocapillary deformation of droplets on glassy membranes. The deformation is observed as the film is heated through the glass transition. The results are replicated using a similar model as Paper I, but with the additional ingredient that the mechanical tension varies with temperature until the film enters the melt state where the mechanical tension vanishes. In this project, I was involved in developing the theoretical model and provided mentorship to A. Fortais who performed the experiments.

Paper AI

The effects of viscosity on the undulatory swimming dynamics of C. elegans

M. Backholm, A. K. S. Kasper, R. D. Schulman, W. S. Ryu and K. Dalnoki-Veress, Phys. Fluids, **27**, 091901 (2015)

Paper AII

Elastocapillary bending of microfibers around liquid droplets

R. D. Schulman, A. Porat, K. Charlesworth, A. Fortais, T. Salez, E. Raphaël and K. Dalnoki-Veress, Soft Matter, **13**, 720 (2017).

Paper AIII

Liquid droplets on a free-standing glassy membrane: Deformation through the glass transition

A. Fortais, R. D. Schulman, and K. Dalnoki-Veress, Eur. Phys. J. E, **40**, 69 (2017).

Bibliography

[1] B. Roman and J. Bico. Elasto-capillarity: deforming an elastic structure with a liquid droplet. *J. Phys. Condens. Matter*, 22(49):493101, 2010.

[2] J. W. Van Honschoten, M. Escalante, N. R. Tas, H. V. Jansen, and M. Elwenspoek. Elastocapillary filling of deformable nanochannels. *J. Appl. Phys.*, 101(9):094310, 2007.

[3] J.-G. Fan, D. Dyer, G. Zhang, and Y.-P Zhao. Nanocarpet effect: Pattern formation during the wetting of vertically aligned nanorod arrays. *Nano Lett.*, 4(11):2133–2138, 2004.

[4] A. Dev and S. Chaudhuri. Uniform large-scale growth of micropatterned arrays of ZnO nanowires synthesized by a surfactant assisted approach. *Nanotechnology*, 18(17):175607, 2007.

[5] R. A. L. Jones. *Soft condensed matter.* Oxford University Press, 2002.

[6] P.-G. de Gennes, F. Brochard-Wyart, and D. Quere. *Capillarity and Wetting Phenomena.* Springer, 2008.

[7] M. V. Berry. The molecular mechanism of surface tension. *Phys. Educ.*, 6(2):79, 1971.

[8] M. J. P. Nijmeijer, C. Bruin, A. F. Bakker, and J. M. J. van Leeuwen. Wetting and drying of an inert wall by a fluid in a molecular-dynamics simulation. *Phys. Rev. A*, 42:6052–6059, 1990.

[9] A. Marchand, J. H. Weijs, J. H. Snoeijer, and B. Andreotti. Why is surface tension a force parallel to the interface? *Am. J. Phys*, 79(10):999–1008, 2011.

[10] J. H. Weijs, A. Marchand, B. Andreotti, D. Lohse, and J. H. Snoeijer. Origin of line tension for a Lennard-Jones nanodroplet. *Phys. Fluids*, 23(2):022001, 2011.

[11] C. Isenberg. *The science of soap films and soap bubbles.* Courier Corporation, 1978.

[12] P.-G. De Gennes. Wetting: statics and dynamics. *Rev. Mod. Phys.*, 57(3):827, 1985.

[13] J. Pellicer, J. Manzanares, and S. Mafé. The physical description of elementary surface phenomena: thermodynamics versus mechanics. *Am. J. Phys*, 63(6):542–547, 1995.

[14] T Young. Analysis of interfacial forces, london. *Philos. Trans. R. Soc., A*, 95:65, 1805.

[15] J. B. Bostwick, M. Shearer, and K. E. Daniels. Elastocapillary deformations on partially-wetting substrates: rival contact-line models. *Soft Matter*, 10(37):7361–7369, 2014.

[16] I. Langmuir. Oil lenses on water and the nature of monomolecular expanded films. *J. Chem. Phys.*, 1(11):756–776, 1933.

[17] O. K. C. Tsui and T. P. Russell. *Polymer thin films.* World Scientific, 2008.

[18] M. B Williams and S. H. Davis. Nonlinear theory of film rupture. *J. Colloid Interface Sci.*, 90(1):220–228, 1982.

[19] F. B. Wyart and J. Daillant. Drying of solids wetted by thin liquid films. *Can. J. Phys*, 68(9):1084–1088, 1990.

[20] G. Reiter. Dewetting of thin polymer films. *Phys. Rev. Lett.*, 68(1):75, 1992.

[21] G. Reiter. Unstable thin polymer films: rupture and dewetting processes. *Langmuir*, 9(5):1344–1351, 1993.

[22] J. F. Padday. Cohesive properties of thin films of liquids adhering to a solid surface. *Spec. Disc. Faraday Soc.*, 1:64–74, 1970.

[23] A. Sharma and E. Ruckenstein. Dewetting of solids by the formation of holes in macroscopic liquid films. *J. Colloid Interface Sci.*, 133(2):358–368, 1989.

[24] C. Redon, F. Brochard-Wyart, and F. Rondelez. Dynamics of dewetting. *Phys. Rev. Lett.*, 66(6):715, 1991.

[25] K. Jacobs, S. Herminghaus, and K. R. Mecke. Thin liquid polymer films rupture via defects. *Langmuir*, 14(4):965–969, 1998.

[26] R. Seemann, S. Herminghaus, and K. Jacobs. Dewetting patterns and molecular forces: A reconciliation. *Phys. Rev. Lett.*, 86(24):5534, 2001.

[27] A. Buguin, L. Vovelle, and F. Brochard-Wyart. Shocks in inertial dewetting. *Phys. Rev. Lett.*, 83(6):1183, 1999.

[28] D. J. Acheson. *Elementary fluid dynamics*. Oxford University Press, 1990.

[29] M. Rubinstein and R. Colby. *Polymer physics*. Oxford university press New York, 2003.

[30] G. Reiter, M. Hamieh, P. Damman, S. Sclavons, G. Sylvain, T. Vilmin, and E. Raphaël. Residual stresses in thin polymer films cause rupture and dominate early stages of dewetting. *Nat. Mater.*, 4(10):754, 2005.

[31] R. Fetzer, K. Jacobs, A. Münch, B. Wagner, and T. P. Witelski. New slip regimes and the shape of dewetting thin liquid films. *Phys. Rev. Lett.*, 95(12):127801, 2005.

[32] S. Gabriele, S. Sclavons, G. Reiter, and P. Damman. Disentanglement time of polymers determines the onset of rim instabilities in dewetting. *Phys. Rev. Lett.*, 96(15):156105, 2006.

[33] P. Damman, S. Gabriele, S. Coppée, S. Desprez, D. Villers, T. Vilmin, E. Raphaël, M. Hamieh, S. A. Akhrass, and G. Reiter. Relaxation of residual stress and reentanglement of polymers in spin-coated films. *Phys. Rev. Lett.*, 99:036101, 2007.

[34] O. Bäumchen, M. Lessel, R. Fetzer, R. Seemann, and K. Jacobs. Sliding fluids: dewetting experiments reveal the solid/liquid boundary condition. *J. Phys. Conf. Ser.*, 216(1):012002, 2010.

[35] J. D. McGraw, T. S. Chan, S. Maurer, T. Salez, M. Benzaquen, E. Raphaël, M. Brinkmann, and K. Jacobs. Slip-mediated dewetting of polymer microdroplets. *Proc. Natl. Acad. Sci. U.S.A.*, 113(5):1168–1173, 2016.

[36] S. Herminghaus, R. Seemann, and K. Jacobs. Generic morphologies of viscoelastic dewetting fronts. *Phys. Rev. Lett.*, 89:056101, 2002.

[37] R. Seemann, S. Herminghaus, and K. Jacobs. Gaining control of pattern formation of dewetting liquid films. *J. Phys. Cond. Mat.*, 13(21):4925, 2001.

[38] J. P. De Silva, M. Geoghegan, A. M. Higgins, G. Krausch, M.-O. David, and G. Reiter. Switching layer stability in a polymer bilayer by thickness variation. *Phys. Rev. Lett.*, 98(26):267802, 2007.

[39] C. Redon, J. B. Brzoska, and F. Brochard-Wyart. Dewetting and slippage of microscopic polymer films. *Macromolecules*, 27(2):468–471, 1994.

[40] A. Münch. Dewetting rates of thin liquid films. *J. Phys. Cond. Mat.*, 17(9):S309, 2005.

[41] L. Rockford, Y. Liu, P. Mansky, T. P. Russell, M. Yoon, and S. G. J. Mochrie. Polymers on nanoperiodic, heterogeneous surfaces. *Phys. Rev. Lett.*, 82(12):2602, 1999.

[42] A. M. Higgins and R. A. L. Jones. Anisotropic spinodal dewetting as a route to self-assembly of patterned surfaces. *Nature*, 404(6777):476, 2000.

[43] R. Konnur, K. Kargupta, and A. Sharma. Instability and morphology of thin liquid films on chemically heterogeneous substrates. *Phys. Rev. Lett.*, 84(5):931, 2000.

[44] N. Rehse, C. Wang, M. Hund, M. Geoghegan, R. Magerle, and G. Krausch. Stability of thin polymer films on a corrugated substrate. *Eur. Phys. J. E*, 4(1):69–76, 2001.

[45] K. Y. Suh and H. H. Lee. Capillary force lithography: large-area patterning, self-organization, and anisotropic dewetting. *Adv. Funct. Mater.*, 12(6-7):405–413, 2002.

[46] K. Kargupta and A. Sharma. Dewetting of thin films on periodic physically and chemically patterned surfaces. *Langmuir*, 18(5):1893–1903, 2002.

[47] A. Sehgal, V. Ferreiro, J. F. Douglas, E. J. Amis, and A. Karim. Pattern-directed dewetting of ultrathin polymer films. *Langmuir*, 18(18):7041–7048, 2002.

[48] S. Timoshenko and J. N. Goodier. *Theory of Elasticity, 2nd.* McGraw-Hill Book Company, Inc., New York, 1951.

[49] L. D. Landau and E. M. Lifshitz. *Theory of Elasticity, 3rd.* Butterworth-Heinemann, New York, 1986.

[50] S. P. Timoshenko and S. Woinowsky-Krieger. *Theory of plates and shells.* McGraw-hill, 1959.

[51] H. L. Langhaar. *Energy methods in applied mechanics.* Courier Dover Publications, 2016.

[52] W. D. Means. *Stress and strain: basic concepts of continuum mechanics for geologists.* Springer Science & Business Media, 2012.

[53] J. E. Mark. *Physical properties of polymers handbook*, volume 1076. Springer, 2007.

[54] J. G. Drobny. *Handbook of thermoplastic elastomers.* Elsevier, 2014.

[55] R. C. Cammarata. Surface and interface stress effects in thin films. *Prog. Surf. Sci.*, 46(1):1–38, 1994.

[56] H. Ibach. The role of surface stress in reconstruction, epitaxial growth and stabilization of mesoscopic structures. *Surf. Sci. Rep.*, 29(5-6):195–263, 1997.

[57] P. Müller and A. Saúl. Elastic effects on surface physics. *Surf. Sci. Rep.*, 54(5):157–258, 2004.

[58] P. Müller, A. Saùl, and F. Leroy. Simple views on surface stress and surface energy concepts. *Adv. Nat. Sci.: Nanosci. Nanotechnol.*, 5(1):013002, 2013.

[59] R. Shuttleworth. The surface tension of solids. *Proc. Phys. Soc. London, Sec. A*, 63(5):444, 1950.

[60] M. M. Nicolson. Surface tension in ionic crystals. *Proc. R. Soc. London, Ser. A*, 228(1175):490–510, 1955.

[61] R. E. Martinez, W. M. Augustyniak, and J. A. Golovchenko. Direct measurement of crystal surface stress. *Phys. Rev. Lett.*, 64(9):1035, 1990.

[62] A. J. Schell-Sorokin and R. M. Tromp. Mechanical stresses in (sub) monolayer epitaxial films. *Phys. Rev. Lett.*, 64(9):1039, 1990.

[63] R. Berger, E. Delamarche, H. P. Lang, C. Gerber, J. K. Gimzewski, E. Meyer, and H.-J. Güntherodt. Surface stress in the self-assembly of alkanethiols on gold. *Science*, 276(5321):2021–2024, 1997.

[64] C. W. Mays, J. S. Vermaak, and D. Kuhlmann-Wilsdorf. On surface stress and surface tension: ii. determination of the surface stress of gold. *Surf. Sci.*, 12(2):134–140, 1968.

[65] H. J. Wasserman and J. S. Vermaak. On the determination of a lattice contraction in very small silver particles. *Surf. Sci.*, 22(1):164–172, 1970.

[66] H. J. Wasserman and J. S. Vermaak. On the determination of the surface stress of copper and platinum. *Surf. Sci.*, 32(1):168–174, 1972.

[67] P. M. Diehm, P. Ágoston, and K. Albe. Size-dependent lattice expansion in nanoparticles: reality or anomaly? *ChemPhysChem*, 13(10):2443–2454, 2012.

[68] R. G. Linford. Surface energy of solids. *Chem. Soc. Rev.*, 1:445–464, 1972.

[69] J. J. Bikerman. Surface energy of solids. In *Inorganic and Physical Chemistry*, pages 1–66. Springer, 1978.

[70] B. J. Keene. Review of data for the surface tension of pure metals. *Int. Mater. Rev.*, 38(4):157–192, 1993.

[71] R.-J. Roe. Surface tension of polymer liquids. *J. Phys. Chem.*, 72(6):2013–2017, 1968.

[72] S. Wu. Surface and interfacial tensions of polymer melts: i. polyethylene, polyisobutylene, and polyvinyl acetate. *J. Colloid Interface Sci.*, 31(2):153–161, 1969.

[73] S. Wu. Surface and interfacial tensions of polymer melts: ii. poly (methyl methacrylate), poly (n-butyl methacrylate), and polystyrene. *J. Phys. Chem.*, 74(3):632–638, 1970.

[74] K. L. Johnson, K. Kendall, and A. D. Roberts. Surface energy and the contact of elastic solids. In *Proc. R. Soc. Lond. A*, volume 324, pages 301–313. The Royal Society, 1971.

[75] M. K. Chaudhury and G. M. Whitesides. Direct measurement of interfacial interactions between semispherical lenses and flat sheets of poly (dimethylsiloxane) and their chemical derivatives. *Langmuir*, 7(5):1013–1025, 1991.

[76] A. Marchand, S. Das, J. H. Snoeijer, and B. Andreotti. Capillary pressure and contact line force on a soft solid. *Phys. Rev. Lett.*, 108(9):094301, 2012.

[77] N. Nadermann, C.-Y. Hui, and A. Jagota. Solid surface tension measured by a liquid drop under a solid film. *Proc. Natl. Acad. Sci. U.S.A.*, 110(26):10541–5, 2013.

[78] R. Style, R. Boltyanskiy, Y. Che, J. Wettlaufer, L. A. Wilen, and E. Dufresne. Universal Deformation of Soft Substrates Near a Contact Line and the Direct Measurement of Solid Surface Stresses. *Phys. Rev. Lett.*, 110(6):066103, 2013.

[79] M. Zhai and G. B. McKenna. Elastic modulus and surface tension of a polyurethane rubber in nanometer thick films. *Polymer*, 55(11):2725–2733, 2014.

[80] S. J. Park, B. M. Weon, J. S. Lee, J. Lee, J. Kim, and J. H. Je. Visualization of asymmetric wetting ridges on soft solids with X-ray microscopy. *Nat. Commun.*, 5:4369, 2014.

[81] S. Mondal, M. Phukan, and A. Ghatak. Estimation of solid–liquid interfacial tension using curved surface of a soft solid. *Proc. Natl. Acad. Sci. U.S.A.*, 112(41):12563–12568, 2015.

[82] B. Andreotti, O. Baumchen, F. Boulogne, K. E. Daniels, E. R. Dufresne, H. Perrin, T. Salez, J. H. Snoeijer, and R. W. Style. Solid capillarity: when and how does surface tension deform soft solids? *Soft Matter*, 12:2993–2996, 2016.

[83] B. Andreotti and J. H. Snoeijer. Soft wetting and the Shuttleworth effect, at the crossroads between thermodynamics and mechanics. *Eur. Phys. Lett.*, 113(6):66001, 2016.

[84] X. Xu, A. Jagota, D. Paretkar, and C.-Y. Hui. Surface tension measurement from the indentation of clamped thin films. *Soft Matter*, 12(23):5121–5126, 2016.

[85] Q. Xu, K. E. Jensen, R. Boltyanskiy, R. W. Sarfati, R.and Style, and E. R. Dufresne. Direct measurement of strain-dependent solid surface stress. *Nat. Commun.*, 8(555), 2017.

[86] Q. Xu, R. W. Style, and E. R. Dufresne. Surface elastic constants of a soft solid. *Soft matter*, 14(6):916–920, 2018.

[87] H. Liang, Z. Cao, Z. Wang, and A. V. Dobrynin. Surface stress and surface tension in polymeric networks. *ACS Macro Lett.*, 7:116–121, 2018.

[88] J. H. Weijs, J. H. Snoeijer, and B. Andreotti. Capillarity of soft amorphous solids: A microscopic model for surface stress. *Phys. Rev. E*, 89(4):042408, 2014.

[89] J. A. F. Plateau. *Statique expérimentale et théorique des liquides soumis aux seules forces moléculaires*. Gauthier-Villars, 1873.

[90] S. Mora, T. Phou, J.-M. Fromental, L. M. Pismen, and Y. Pomeau. Capillarity driven instability of a soft solid. *Phys. Rev. Lett.*, 105(21):214301, 2010.

[91] C. Y. Hui, A. Jagota, Y. Y. Lin, and E. J. Kramer. Constraints on microcontact printing imposed by stamp deformation. *Langmuir*, 18(4):1394–1407, 2002.

[92] A. Jagota, D. Paretkar, and A. Ghatak. Surface-tension-induced flattening of a nearly plane elastic solid. *Phys. Rev. E*, 85(5):051602, 2012.

[93] S. Mora, C. Maurini, T. Phou, J.-M. Fromental, B. Audoly, and Y. Pomeau. Solid drops: large capillary deformations of immersed elastic rods. *Phys. Rev. Lett.*, 111(11):114301, 2013.

[94] C. Py, P. Reverdy, L. Doppler, J. Bico, B. Roman, and C. N. Baroud. Capillary origami: spontaneous wrapping of a droplet with an elastic sheet. *Phys. Rev. Lett.*, 98(15):156103, 2007.

[95] N. Patra, B. Wang, and P. Král. Nanodroplet activated and guided folding of graphene nanostructures. *Nano Lett.*, 9(11):3766–3771, 2009.

[96] J. Bae, T. Ouchi, and R. C. Hayward. Measuring the elastic modulus of thin polymer sheets by elastocapillary bending. *ACS Appl. Mater. Inter.*, 7(27):14734–14742, 2015.

[97] J. D. Paulsen, V. Démery, C. D. Santangelo, T. P. Russell, B. Davidovitch, and N. Menon. Optimal wrapping of liquid droplets with ultrathin sheets. *Nat. Mater.*, 14(12):1206, 2015.

[98] D. Kumar, J. D. Paulsen, T. P. Russell, and N. Menon. Wrapping with a splash: high-speed encapsulation with ultrathin sheets. *Science*, 359(6377):775–778, 2018.

[99] J. W. van Honschoten, J. W. Berenschot, T. Ondarcuhu, R. G. P. Sanders, J. Sundaram, M. Elwenspoek, and N. R. Tas. Elastocapillary fabrication of three-dimensional microstructures. *Appl. Phys. Lett.*, 97(1):014103, 2010.

[100] N. Chakrapani, B. Wei, A. Carrillo, P. M. Ajayan, and R. S. Kane. Capillarity-driven assembly of two-dimensional cellular carbon nanotube foams. *Proc. Natl. Acad. Sci. U.S.A.*, 101(12):4009–4012, 2004.

[101] K. K. S. Lau, J. Bico, K. B. K. Teo, M. Chhowalla, G. A. J. Amaratunga, W. I. Milne, G. H. McKinley, and K. K. Gleason. Superhydrophobic carbon nanotube forests. *Nano Lett.*, 3(12):1701–1705, 2003.

[102] B. Pokroy, S. H. Kang, L. Mahadevan, and J. Aizenberg. Self-organization of a mesoscale bristle into ordered, hierarchical helical assemblies. *Science*, 323(5911):237–240, 2009.

[103] C. Py, R. Bastien, J. Bico, B. Roman, and A. Boudaoud. 3d aggregation of wet fibers. *Europhys. Lett.*, 77(4):44005, 2007.

[104] J. Bico, B. Roman, L. Moulin, and A. Boudaoud. Adhesion: elastocapillary coalescence in wet hair. *Nature*, 432(7018):690–690, 2004.

[105] F. Vollrath and D. T. Edmonds. Modulation of the mechanical properties of spider silk by coating with water. *Nature*, 304:305, 1989.

[106] H. Elettro, F. Vollrath, A. Antkowiak, and S. Neukirch. Coiling of an elastic beam inside a disk: a model for spider-capture silk. *Int. J. Non-linear Mech.*, 75:59–66, 2015.

[107] H. Elettro, S. Neukirch, F. Vollrath, and A. Antkowiak. In-drop capillary spooling of spider capture thread inspires hybrid fibers with mixed solidliquid mechanical properties. *Proc. Natl. Acad. Sci. U.S.A.*, 113(22):6143–6147, 2016.

[108] G. R. Lester. Contact angles of liquids at deformable solid surfaces. *J. Colloid Sci.*, 16(4):315–326, 1961.

[109] M. E. R. Shanahan. The influence of solid micro-deformation on contact angle equilibrium. *J. Phys. D*, 20(7):945, 1987.

[110] R. Pericet-Cámara, A. Best, H.-J. Butt, and E. Bonaccurso. Effect of capillary pressure and surface tension on the deformation of elastic surfaces by sessile liquid microdrops: an experimental investigation. *Langmuir*, 24(19):10565–10568, 2008.

[111] E. R. Jerison, Y. Xu, L. A. Wilen, and E. R. Dufresne. Deformation of an elastic substrate by a three-phase contact line. *Phys. Rev. Lett.*, 106(18):186103, 2011.

[112] R. W. Style and E. R. Dufresne. Static wetting on deformable substrates, from liquids to soft solids. *Soft Matter*, 8(27):7177, 2012.

[113] A. Marchand, S. Das, J. H. Snoeijer, and B. Andreotti. Contact angles on a soft solid: from Young's law to Neumann's law. *Phys. Rev. Lett.*, 109(23):236101, 2012.

[114] C.-Y. Hui and A. Jagota. Deformation near a liquid contact line on an elastic substrate. *Proc. R. Soc. A*, 470, 2014.

[115] Z. Cao and A. V. Dobrynin. Polymeric droplets on soft surfaces: from Neumann's triangle to Young's law. *Macromolecules*, 48(2):443–451, 2015.

[116] R. W. Style, A. Jagota, C.-Y. Hui, and E. R. Dufresne. Elastocapillarity: surface tension and the mechanics of soft solids. *Annu. Rev. Condens. Matter Phys.*, 8:99–118, 2017.

[117] R. W. Style, Y. Che, S. J. Park, B. M. Weon, J. H. Je, C. Hyland, G. K. German, M. P. Power, L. A. Wilen, J. S. Wettlaufer, and E. R. Dufresne. Patterning droplets with durotaxis. *Proc. Natl. Acad. Sci. U.S.A.*, 110(31):12541–12544, 2013.

[118] J. B. Alvarez, Y. Bazilevs, R. Juanes, and H. Gomez. Wettability control of droplet durotaxis. *Soft Matter*, 2018.

[119] S. Karpitschka, A. Pandey, L. A. Lubbers, J. H. Weijs, L. Botto, S. Das, B. Andreotti, and J. H. Snoeijer. Liquid drops attract or repel by the inverted cheerios effect. *Proc. Natl. Acad. Sci. U.S.A.*, 113(27):7403–7407, 2016.

[120] J. Huang, M. Juszkiewicz, W. H. de Jeu, E. Cerda, T. Emrick, N. Menon, and T. P. Russell. Capillary wrinkling of floating thin polymer films. *Science*, 317(5838):650–3, 2007.

[121] D. Vella, M. Adda-Bedia, and E. Cerda. Capillary wrinkling of elastic membranes. *Soft Matter*, 6(22):5778–5782, 2010.

[122] R. D. Schroll, M. Adda-Bedia, E. Cerda, J. Huang, N. Menon, T. P. Russell, K. B. Toga, D. Vella, and B. Davidovitch. Capillary deformations of bendable films. *Phys. Rev. Lett.*, 111(1):014301, 2013.

[123] M. E. R. Shanahan. Contact angle equilibrium on thin elastic solids. *J. Adhes.*, 18(4):247–267, 1985.

[124] C.-Y. Hui, A. Jagota, N. Nadermann, and X. Xu. Deformation of a solid film with surface tension by a liquid drop. *Procedia IUTAM*, 12:116–123, 2015.

[125] C.-Y. Hui and A. Jagota. Planar equilibrium shapes of a liquid drop on a membrane. *Soft Matter*, 11(46):8960–8967, 2015.

[126] P. Martin and F. Brochard-Wyart. Dewetting at soft interfaces. *Phys. Rev. Lett.*, 80(15):3296, 1998.

[127] F. Brochard-Wyart and P.-G. De Gennes. Dewetting of a water film between a solid and a rubber. *J. Phys. Condens. Matter*, 6(23A):A9, 1994.

[128] A. Carré and M. E. R. Shanahan. Influence of the “wetting ridge” in dry patch formation. *Langmuir*, 11(9):3572–3575, 1995.

[129] S. Kumar and O. K. Matar. Dewetting of thin liquid films near soft elastomeric layers. *J. Colloid Interface Sci.*, 273(2):581–588, 2004.

[130] O. K. Matar, V. Gkanis, and S. Kumar. Nonlinear evolution of thin liquid films dewetting near soft elastomeric layers. *J. Colloid Interface Sci.*, 286(1):319–332, 2005.

[131] L. Qiao and L. H. He. Anisotropic dewetting on stretched elastomeric substrates. *Eur. Phys. J. E*, 26(4):387–393, 2008.

[132] T. Becker and F. Mugele. Collapse of molecularly thin lubricant layers between elastic substrates. *J. Phys. Condens. Matter*, 15(1):S321, 2002.

[133] S. de Beer, D. ‘t. Mannetje, S. Zantema, and F. Mugele. Instability of confined water films between elastic surfaces. *Langmuir*, 26(5):3280–3285, 2009.

[134] A. Carlson and L. Mahadevan. Similarity and singularity in adhesive elastohydrodynamic touchdown. *Phys. Fluids*, 28(1):011702, 2016.

[135] J. M. Margolis. *Engineering Thermoplastics: Properties and Applications.* Marcel Dekker, Inc., 1985.